








































GRANDMA and HXMT Observations of GRB 221009A - the Standard-Luminosity Afterglow of a Hyper-Luminous Gamma-Ray Burst - In Gedenken an David Alexander Kann

D. A. KANN ^{1,*}, S. AGAYEVA ², V. AIVAZYAN,^{3,4} S. ALISHOV,² C. M. ANDRADE ⁵, S. ANTIER ⁶, A. BARANSKY ⁷, P. BENDJOYA,⁸ Z. BENKHALDOUN ⁹, S. BERADZE ^{3,4}, D. BEREZIN,¹⁰ M. BOËR ⁶, E. BROENS ¹¹, S. BRUNIER,⁸ M. BULLA ^{12,13,14}, O. BURKHONOV ¹⁵, E. BURNS ¹⁶, Y. CHEN,¹⁷ Y. P. CHEN,¹⁷ M. CONTI,¹⁸ M. W. COUGHLIN ⁵, W. W. CUI,¹⁷ F. DAIGNE,¹⁹ B. DELAVEAU,²⁰ H. A. R. DEVILLEPOIX,²¹ T. DIETRICH ^{22,23}, D. DORNIC ²⁴, F. DUBOIS,^{25,26} J.-G. DUCOIN,¹⁹ E. DURAND,²⁰ P.-A. DUVERNE,²⁷ H.-B. EGGENSTEIN ²⁸, S. EHGAMBERDIEV ^{15,29}, A. FOUAD,³⁰ M. FREEBERG ³¹, D. FROEBRICH ³², M. Y. GE,¹⁷ S. GERVASONI,⁶ V. GODUNOVA ¹⁰, P. GOKULDASS,³³ E. GURBANOV,² D. W. HAN,¹⁷ E. HASANOV,² P. HELLO,³⁴ T. HUSSENOT-DESENONGES,³⁴ R. INASARIDZE ^{3,4}, A. ISKANDAR,³⁵ N. ISMAILOV ³⁶, A. JANATI,⁹ T. JEGOU DU LAZ,³⁴ S. M. JIA,¹⁷ S. KARPOV ³⁷, A. KAEOUACH,³⁸ R. W. KIENDREBEOGO ^{6,39,5}, A. KLOTZ ^{40,41}, R. KNEIP,⁴² N. KOCHIASHVILI ³, N. KUNERT,²² A. LEKIC,²⁰ S. LEONINI,¹⁸ C. K. LI,¹⁷ W. LI,¹⁷ X. B. LI,¹⁷ J. Y. LIAO,¹⁷ L. LOGIE,^{25,26} F. J. LU,¹⁷ J. MAO,^{43,44,45} D. MARCHAIS,⁴⁶ R. MÉNARD,⁴⁷ D. MORRIS,⁴⁸ R. NATSVLISHVILI,³ V. NEDORA,²³ K. NOONAN,⁴⁸ K. NOYSNA ⁴⁹, N. B. ORANGE,⁵⁰ P. T. H. PANG,^{51,52} H. W. PENG,⁵³ C. PELLLOIN ¹⁹, J. PELOTON ³⁴, T. PRADIER ⁵⁴, O. PYSHNA,⁷ Y. RAJABOV ¹⁵, S. RAU,^{25,26} C. RINNER,⁹ J.-P. RIVET,⁸ F. D. ROMANOV ⁵⁵, P. ROSI,¹⁸ V. A. RUPCHANDANI,^{56,57} M. SERRAU,⁵⁸ A. SHOKRY,³⁰ A. SIMON,^{59,60} K. SMITH,⁴⁸ O. SOKOLIUK,^{7,10} M. SOLIMAN,⁶¹ L. M. SONG,¹⁷ A. TAKEY ³⁰, Y. TILLAYEV ^{15,29}, L. M. TINJACA RAMIREZ,¹⁸ I. TOSTA E MELO,⁶² D. TURPIN ⁶³, A. DE UGARTE POSTIGO ⁶, S. VANAVERBEKE ^{25,26}, V. VASYLENKO,^{59,60} D. VERNET,⁶⁴ Z. VIDADI ³⁶, C. WANG,⁶⁵ J. WANG,¹⁷ L. T. WANG,³⁵ X. F. WANG ^{53,66}, S. L. XIONG,^{17,†} Y. P. XU,¹⁷ W. C. XUE,¹⁷ X. ZENG,⁶⁷ S. N. ZHANG,¹⁷ H. S. ZHAO,¹⁷ AND X. F. ZHAO¹⁷

¹Hessian Research Cluster ELEMENTS, Giersch Science Center, Max-von-Laue-Straße 12, Goethe University Frankfurt, Campus Riedberg, 60438 Frankfurt am Main, Germany

²N. Tusi Shamakhy Astrophysical Observatory, Azerbaijan National Academy of Sciences, settl. Y. Mammadaliyev, AZ 5626, Shamakhy, Azerbaijan

³E. Kharadze Georgian National Astrophysical Observatory, Mt. Kanobili, Abastumani, 0301, Adigeni, Georgia

⁴Samtskhe-Javakheti State University, Rustaveli Str. 113, Akhaltsikhe, 0080, Georgia

⁵School of Physics and Astronomy, University of Minnesota, Minneapolis, Minnesota 55455, USA

⁶Artemis, Observatoire de la Côte d'Azur, Université Côte d'Azur, Boulevard de l'Observatoire, 06304 Nice, France

⁷Astronomical Observatory of Taras Shevchenko National University of Kyiv, Observatorna Str. 3, Kyiv, 04053, Ukraine

⁸Laboratoire J.-L. Lagrange, Université de Nice Sophia-Antipolis, CNRS, Observatoire de la Côte d'Azur, 06304 Nice, France

⁹Oukaimeden Observatory, High Energy Physics and Astrophysics Laboratory, FSSM, Cadi Ayyad University, Av. Prince My Abdellah, BP 2390 Marrakesh, Morocco

¹⁰Main Astronomical Observatory of National Academy of Sciences of Ukraine, 27 Acad. Zabolotnoho Str., Kyiv, 03143, Ukraine

¹¹Vereniging Voor Sterrenkunde, Balen-Neetlaan 18A, 2400, Mol, Belgium

¹²Department of Physics and Earth Science, University of Ferrara, via Saragat 1, I-44122 Ferrara, Italy

¹³INFN, Sezione di Ferrara, via Saragat 1, I-44122 Ferrara, Italy

¹⁴INAF, Osservatorio Astronomico d'Abruzzo, via Mentore Maggini snc, I-64100 Teramo, Italy

¹⁵Ulugh Beg Astronomical Institute, Uzbekistan Academy of Sciences, Astronomy Str. 33, Tashkent 100052, Uzbekistan

¹⁶Department of Physics & Astronomy, Louisiana State University, Baton Rouge, LA 70803, USA

¹⁷Key Laboratory of Particle Astrophysics, Institute of High Energy Physics, Chinese Academy of Sciences, Beijing 100049, People's Republic of China

¹⁸Montarrenti Observatory, S. S. 73 Ponente, I-53018 Sovicille, Siena, Italy

¹⁹Sorbonne Université, CNRS, UMR 7095, Institut d'Astrophysique de Paris, 98 bis bd Arago, 75014 Paris, France

²⁰Institut Polytechnique des Sciences Avancées IPSA, 63 bis Boulevard de Brandebourg, 94200 Ivry-sur-Seine, France

²¹Space Science & Technology Centre, School of Earth and Planetary Sciences, Curtin University, GPO Box U1987, Perth, Western Australia 6845, Australia

²²Institute for Physics and Astronomy, University of Potsdam, Haus 28, Karl-Liebknecht-Str. 24/25, 14476 Potsdam, Germany

²³Max Planck Institute for Gravitational Physics (Albert Einstein Institute), Am Mühlenberg 1, 14476 Potsdam, Germany

²⁴CPPM, Aix Marseille Univ, CNRS/IN2P3, CPPM, Marseille, France

²⁵AstroLAB IRIS, Provinciale Domein "De Palingbeek", Verbrandemolenstraat 5, 8902 Zillebeke, Ieper, Belgium

²⁶Vereniging Voor Sterrenkunde (VVS), Oostmeers 122 C, 8000 Brugge, Belgium

arXiv:2302.06225v2 [astro-ph.HE] 27 Mar 2023

- ²⁷ *Université Paris Cité, CNRS, Astroparticule et Cosmologie, F-75013 Paris, France*
- ²⁸ *Volkssternwarte Paderborn, Im Schlosspark 13, 33104 Paderborn, Germany*
- ²⁹ *National University of Uzbekistan, 4 University Str., Tashkent 100174, Uzbekistan*
- ³⁰ *National Research Institute of Astronomy and Geophysics (NRIAG), 1 El-marsad St., 11421 Helwan, Cairo, Egypt*
- ³¹ *KNC, AAVSO, Hidden Valley Observatory (HVO), Colfax, WI, USA; iTelescope, New Mexico Skies Observatory, Mayhill, NM, USA*
- ³² *School of Physics and Astronomy, University of Kent, Canterbury CT2 7NH, UK*
- ³³ *Department of Aerospace, Physics, and Space Sciences, Florida Institute of Technology, Melbourne, Florida 32901, USA*
- ³⁴ *IJCLab, Univ Paris-Saclay, CNRS/IN2P3, Orsay, France*
- ³⁵ *Xinjiang Astronomical Observatory (XAO), Chinese Academy of Sciences, Urumqi, 830011, People's Republic of China*
- ³⁶ *N. Tusi Shamakhy Astrophysical Observatory Azerbaijan National Academy of Sciences, settl. Y. Mammadaliyev, AZ 5626, Shamakhy, Azerbaijan*
- ³⁷ *CEICO, Institute of Physics of the Czech Academy of Sciences, Na Slovance 1999/2, CZ-182 21, Praha, Czech Republic*
- ³⁸ *Oukaimeden Observatory, Cadi Ayyad University, High Atlas Observatory, Morocco*
- ³⁹ *Laboratoire de Physique et de Chimie de l'Environnement, Université Joseph KI-ZERBO, Ouagadougou, Burkina Faso*
- ⁴⁰ *IRAP, Université de Toulouse, CNRS, UPS, 14 Avenue Edouard Belin, F-31400 Toulouse, France*
- ⁴¹ *Université Paul Sabatier Toulouse III, Université de Toulouse, 118 Route de Narbonne, 31400 Toulouse, France*
- ⁴² *K26 / Contern Observatory (private obs.), 1, beim Schmilberbour, 5316 Contern, Luxembourg*
- ⁴³ *Yunnan Observatories, Chinese Academy of Sciences, 650011 Kunming, Yunnan Province, People's Republic of China*
- ⁴⁴ *Center for Astronomical Mega-Science, Chinese Academy of Sciences, 20A Datun Road, Chaoyang District, 100012 Beijing, People's Republic of China*
- ⁴⁵ *Key Laboratory for the Structure and Evolution of Celestial Objects, Chinese Academy of Sciences, 650011 Kunming, People's Republic of China*
- ⁴⁶ *Observatoire du 'Crous des Gats', 31550 Cintegabelle, France*
- ⁴⁷ *Club d'astronomie Mont-Tremblant, 545 Chemin Saint-Bernard, Mont-Tremblant, Québec, Canada J8E 1S8*
- ⁴⁸ *University of the Virgin Islands, United States Virgin Islands 00802, USA*
- ⁴⁹ *National Astronomical Research Institute of Thailand (Public Organization), 260, Moo 4, T. Donkaew, A. Mae Rim, Chiang Mai, 50180, Thailand*
- ⁵⁰ *OrangeWave Innovative Science, LLC, Moncks Corner, SC 29461, USA*
- ⁵¹ *Nikhef, Science Park 105, 1098 XG Amsterdam, The Netherlands*
- ⁵² *Institute for Gravitational and Subatomic Physics (GRASP), Utrecht University, Princetonplein 1, 3584 CC Utrecht, The Netherlands*
- ⁵³ *Physics Department, Tsinghua University, Beijing, 100084, People's Republic of China*
- ⁵⁴ *Université de Strasbourg, CNRS, IPHC UMR 7178, 67000 Strasbourg, France*
- ⁵⁵ *AAVSO observer; Pobedy street, house 7, flat 60, Yuzhno-Morskoy, Nakhodka, Primorsky Krai 692954, Russia*
- ⁵⁶ *Brown University, Providence, RI 02912, Rhode Island, USA*
- ⁵⁷ *American University of Sharjah, Sharjah, UAE*
- ⁵⁸ *Société Astronomique de France, Observatoire de Dauban, FR 04150 Banon, France*
- ⁵⁹ *Astronomy and Space Physics Department, Taras Shevchenko National University of Kyiv, Glushkova Ave., 4, Kyiv, 03022, Ukraine*
- ⁶⁰ *National Center Junior Academy of Sciences of Ukraine, Dehtiarivska St. 38-44, Kyiv, 04119, Ukraine*
- ⁶¹ *Department of Astronomy and Meteorology, Faculty of Science, Al-Azhar University, 11884 Nasr City, Cairo, Egypt*
- ⁶² *INFN, Laboratori Nazionali del Sud, I-95125 Catania, Italy*
- ⁶³ *Université Paris-Saclay, Université Paris Cité, CEA, CNRS, AIM, 91191, Gif-sur-Yvette, France*
- ⁶⁴ *Observatoire de la Côte d'Azur, CNRS, UMS Galilée, France*
- ⁶⁵ *National Astronomical Observatories, Chinese Academy of Sciences, Beijing 100012, People's Republic of China*
- ⁶⁶ *Beijing Planetarium, Beijing Academy of Science and Technology, Beijing, 100044, People's Republic of China*
- ⁶⁷ *Center for Astronomy and Space Sciences, China Three Gorges University, Yichang 443000, People's Republic of China*

ABSTRACT

GRB 221009A is the brightest Gamma-Ray Burst (GRB) detected in more than 50 years of study. In this paper, we present observations in the X-ray and optical domains ranging from the prompt emission (optical coverage by all-sky cameras) up to 20 days after the GRB obtained by the GRANDMA Collaboration (which includes observations from more than 30 professional and amateur telescopes) and the *Insight-HXMT* Collaboration operating the X-ray telescope *HXMT*-LE. We study the optical afterglow with empirical fitting using the GRANDMA+*HXMT*-LE data sets, augmented with data from the literature up to 60 days. We then model numerically, using a Bayesian approach, the GRANDMA and *HXMT*-LE afterglow observations, that we augment with *Swift*-XRT and additional optical/NIR

observations reported in the literature. We find that the GRB afterglow, extinguished by a large dust column, is most likely behind a combination of a large Milky-Way dust column combined with moderate low-metallicity dust in the host galaxy. Using the GRANDMA+*HXMT*-LE+XRT dataset, we find that the simplest model, where the observed afterglow is produced by synchrotron radiation at the forward external shock during the deceleration of a top-hat relativistic jet by a uniform medium, fits the multi-wavelength observations only moderately well, with a tension between the observed temporal and spectral evolution. This tension is confirmed when using the extended dataset. We find that the consideration of a jet structure (Gaussian or power-law), the inclusion of synchrotron self-Compton emission, or the presence of an underlying supernova do not improve the predictions, showing that the modelling of GRB22109A will require going beyond the most standard GRB afterglow model. Placed in the global context of GRB optical afterglows, we find the afterglow of GRB 22109A is luminous but not extraordinarily so, highlighting that some aspects of this GRB do not deviate from the global known sample despite its extreme energetics and the peculiar afterglow evolution.

Keywords: Gamma-ray bursts: Individual: GRB 22109A — Optical astronomy (1776) — Optical telescopes (1744) — Interstellar dust extinction (837)

1. INTRODUCTION

Gamma-ray bursts (GRBs) are among the most energetic phenomena detected in the Universe. They release extreme amounts of energy in soft γ -rays, up to $1M_{\odot}$ assuming isotropic emission (Kulkarni et al. 1999; Atteia et al. 2017), and can also be exceedingly luminous in the optical domain (Akerlof et al. 1999; Boër et al. 2006; Kann et al. 2007; Racusin et al. 2008; Bloom et al. 2009; Jin et al. 2023).

GRBs exhibit durations¹ from ms up to several hours (e.g., Thöne et al. 2011; Gendre et al. 2013; Levan et al. 2014a). They have been historically divided (Mazets et al. 1981; Kouveliotou et al. 1993) into two classes based on their duration and spectral hardness.

So-called “short/hard GRBs” have durations of a few seconds or less and a harder spectrum with respect to their isotropic energy release (e.g., Minaev & Pozanenko 2020; Agüí Fernández et al. 2023). They have been linked to gravitational waves (Abbott et al. 2017a,b,c; Goldstein et al. 2017), and their progenitors are supposed to be mainly coalescing compact objects such as binary neutron stars or neutron-star black-hole binary systems (for reviews, see Nakar 2007; Berger 2014). The general “short/hard” paradigm has been called into question especially with the long-duration event GRB 211211A (Rastinejad et al. 2022; Troja et al. 2022; Yang et al. 2022), which has been claimed to be associated

with kilonova emission, a hallmark of compact binary mergers.

Conversely, so-called “long/soft GRBs” generally have durations greater than a few seconds, a softer spectrum, and their origin is most likely related to the core-collapse of rapidly rotating massive stars (Woosley 1993; Mösta et al. 2015). Similar to the case of short GRBs, the “long/soft” paradigm has been called into question by GRB 200826A, a sub-second GRB clearly associated with supernova (SN) emission (Ahumada et al. 2021; Zhang et al. 2021; Rossi et al. 2022). For reviews of long GRBs and their connection to stripped-envelope supernova explosions, see Gehrels et al. (2009); Hjorth & Bloom (2012); Cano et al. (2017).

The luminosity of GRB afterglows (in the X-ray to optical/Near-InfraRed [NIR] energy range) is moderately correlated with the isotropic prompt-emission (mostly γ -ray) energy release E_{iso} (Gehrels et al. 2008; Nysewander et al. 2009; Kann et al. 2010, 2011), so very luminous GRBs usually have more luminous afterglows, and of course a low distance also implies a brighter afterglow that can be more easily followed-up. A combination of these two features therefore usually yields the richest data sets for any electromagnetic study. Two examples of such well-studied, nearby bright GRBs are GRBs 030329 and 130427A. GRB 030329 occurred at $z = 0.16867 \pm 0.00001$ (Thöne et al. 2007), and is to this day the GRB afterglow with the most optical/NIR observations. It yielded data for a wide range of studies on the prompt emission, afterglow evolution and polarization, and the associated SN 2003dh (Vanderspek et al. 2004; Lipkin et al. 2004; Greiner et al. 2003; Hjorth et al. 2003; Stanek et al. 2003; Matheson et al. 2003). The second being GRB 130427A, the first known nearby

* Corresponding author: grandma-l@in2p3.fr

† Corresponding author: xiongsli@ihep.ac.cn

¹ Usually measured as T_{90} , denoting the time span during which 90% of the emission, from 5% to 95%, are accumulated. T_{90} durations are detector-dependent and can include γ -ray tail emission in bright bursts.

GRB ($z = 0.3399 \pm 0.0002$, Selsing et al. 2019) that exhibited an E_{iso} in the range of “cosmological” GRBs at $z \gtrsim 1$. There is also a rich observational data set for this event, stretching from trigger time to nearly 100 Ms (e.g. Maselli et al. 2014; Vestrand et al. 2014; Ackermann et al. 2014; Perley et al. 2014; Melandri et al. 2014; Levan et al. 2014b; van der Horst et al. 2014; De Pasquale et al. 2016).

In this paper, we report observations by the GRANDMA collaboration and its partners of the paragon of nearby, bright GRBs, GRB 221009A, by far the brightest GRB observed to date.

On 9 October 2022, at 14:10:17 UT, the Burst Alert Telescope (BAT, Barthelmy et al. 2005) onboard the *Neil Gehrels Swift Observatory* satellite (Gehrels et al. 2004, *Swift* hereafter) triggered and located a new, X-ray bright transient denoted as *Swift* J1913.1+1946 (triggers 1126853 and 1126854, Dichiaro et al. 2022a,b). *Swift* slewed immediately to the position and its narrow-field instruments, the X-ray telescope (XRT, Burrows et al. 2005) and the Ultra-Violet/Optical Telescope (UVOT, Roming et al. 2005) discovered a transient, which was very bright in X-rays (> 800 ct/s) and moderately bright in the optical (unfiltered finding chart, *white* = 16.63 ± 0.14 mag). The optical detection was somewhat remarkable as the transient lies in the Galactic plane and extinction along the line-of-sight is very high, $E_{(B-V)} = 1.32$ mag/ $A_V = 4.1$ mag (Schlafly & Finkbeiner 2011, henceforth SF11). It was furthermore reported that the source was also detected over ten minutes earlier by the Gas-Slit Camera (GSC) of the *MAXI* X-ray detector onboard the International Space Station (ISS, Negoro et al. 2022; Kobayashi et al. 2022; Williams et al. 2023). Overall, this is in agreement with a new Galactic transient.

About 6.5 hours after the *Swift* trigger, it was reported by Kennea et al. (2022a) that this source may be a GRB, GRB 221009A, as both the Gamma-Ray Burst Monitor (GBM, Meegan et al. 2009) and the Large Area Telescope (LAT, Atwood et al. 2009) of the *Fermi* observatory (GLAST Facility Science Team et al. 1999) triggered on a GRB² localized to the same sky position at 13:16:59.99 UT, which we henceforth use as trigger time T_0 . This event turned out to be extraordinarily bright (Veres et al. 2022), not just the brightest event ever detected by GBM, but the brightest *ever* detected.

² The initial GBM trigger notice was distributed, but a problem with automated data processing prevented any additional real-time classification/localization messages from being sent to the ground.

The event begins with a moderately bright precursor, followed by ≈ 180 s of quiescence before the main phase starts. The first peak, ≈ 20 s long, would already place GRB 221009A among the brightest GRBs ever detected, exceeding all but a handful of GBM/Konus detections. This peak is followed by two ultra-bright peaks, and finally a fourth, less bright but longer peak which fades into a high-energy afterglow at ≈ 600 s. The extreme fluence led to a saturation of all sensitive γ -ray detectors, such as *Fermi* GBM (Lesage et al. 2022), *Fermi* LAT (Bissaldi et al. 2022; Pillera et al. 2022; Omodei et al. 2022a,b), Konus-*Wind* (Frederiks et al. 2022, 2023), *Insight*-HXMT/HE (Tan et al. 2022; Ge et al. 2022), *AGILE*/MCAL+AC (Ursi et al. 2022), and *INTEGRAL* SPI/ACS (Gotz et al. 2022).

This saturation leads to preliminary analyses reporting only lower limits on the true fluence. *INTEGRAL* SPI/ACS (Gotz et al. 2022) analysis finds 1.3×10^{-2} erg/cm², *Fermi* GBM finds $(2.912 \pm 0.001) \times 10^{-2}$ erg/cm² and peak flux 2385 ± 3 ph s⁻¹ cm⁻² (Lesage et al. 2022), Konus-*Wind* report 5.2×10^{-2} erg/cm² (Frederiks et al. 2022), and Kann & Agui Fernandez (2022) estimate $\approx 9 \times 10^{-2}$ erg/cm². Even these preliminary estimates show GRB 221009A exceeded GRB 130427A in fluence by a factor of at least 10. Recently, Frederiks et al. (2023) presented the full Konus-*Wind* analysis, which yields a fluence more than twice as high as that derived by Kann & Agui Fernandez (2022), leading to an isotropic energy release $E_{\text{iso}} > 10^{55}$ erg, twice as high as the previous record holder.

Several smaller orbital detectors were not saturated, stemming from size, environment, or off-axis detection, such as detectors on *Insight* (the Low-Energy (LE) telescope and the Particle Monitors, Ge et al. 2022), *SATech-01/GECAM-C* HEBS (Liu et al. 2022), *GRBAlpha* (Ripa et al. 2022, 2023), *STPSat-6/SIRI-2* (Mitchell et al. 2022), and *SRG/ART-XC* (Lapshov et al. 2022; Frederiks et al. 2023).

Optical spectroscopy of the transient showed it to indeed be a GRB afterglow, with a redshift $z = 0.151$ measured both in absorption and emission (de Ugarte Postigo et al. 2022; Castro-Tirado et al. 2022; Izzo et al. 2022; Malesani et al. 2023), making it even closer than GRB 030329. Such an event is ultra-rare, e.g., Atteia (2022) estimate it to occur only once every half-millennium. Williams et al. (2023), O’Connor et al. (2023) and Malesani et al. (2023) also discuss the rate of events, finding estimates of the same order. Using the significantly higher fluence from Frederiks et al. (2023), Burns et al. (2023) derive an even more extreme value, finding a repetition rate of 1 every $\approx 10,000$ years, a once-in-all-human-civilization event.

The GRB showed very strong VHE emission, with a ≈ 400 GeV photon detected by *Fermi* LAT (Xia et al. 2022a,b), a highly significant detection by *AGILE*/GRID (Piano et al. 2022), photons of ≈ 10 GeV seen more than two weeks after the GRB by DAMPE (Duan et al. 2022), the spectacular detection by LHAASO of thousands of VHE photons up to 18 TeV (Huang et al. 2022), and potentially even a 250 TeV photon detected by Carpet-2 (Dzhappuev et al. 2022).

The burst caused a Sudden Ionospheric Disturbance (Schnoor et al. 2022; Guha & Nicholson 2022; Hayes & Gallagher 2022; Pal et al. 2023). There were no detected neutrinos associated with GRB 221009A, however (Ice-Cube Collaboration 2022; KM3NeT Collaboration 2022; Ai & Gao 2022). The gravitational-wave detectors were off or not sensitive enough to achieve any detection (Panarale 2022).

GRANDMA (Global Rapid Advanced Network for Multi-messenger Addicts) (Antier et al. 2020a,b; Aivazyan et al. 2022) is a collaboration of ground-based facilities dedicated to time-domain astronomy, and focused on electromagnetic follow-up of gravitational-wave candidates and other transients such as GRBs. Its network contains 36 telescopes from 30 observatories, 42 institutions, and groups from 18 countries³. The network has access to wide field-of-view telescopes ([FoV] $> 1\text{deg}^2$) located on three continents, and remote and robotic telescopes with narrower fields-of-view.

Here we present the analysis of the afterglow emission of GRB 221009A with different model approaches. All results are obtained using the *Fermi* GBM trigger time of 9 October 13:16:59.99 UT. In §2, we present the observational data we use in the article, the photometric methods we use and a discussion of the extinction selection. In §3, we present our methods to analyze the afterglow light curves using empirical light-curve fitting and two Bayesian inference analyses. We then present our results to investigate which astrophysical scenarios and processes best describe the data. In §4, we present our conclusions.

2. OBSERVATIONAL DATA

2.1. *Swift* XRT and *HXMT/LE* afterglow data

The *Swift* XRT started to observe the field of GRB 221009A right after BAT triggered on the afterglow, about 56 min after the *Fermi*/GBM trigger time. The X-ray light curve (0.3 – 10 keV) of GRB 221009A was collected from the UK *Swift* Science Data Centre⁴ at the

University of Leicester (Evans et al. 2007, 2009). We directly made use of the Burst Analyser light curve given in Jansky units at the 10 keV central frequencies (Evans et al. 2010). Due to the large number of data points in the *Swift* XRT light curve, we could not use it directly for the MCMC analysis without overweighting the X-ray data. We, therefore, constructed a synthetic light curve of the *Swift* XRT data (both at 1 keV and 10 keV). Assuming a power law spectrum within the *Swift* XRT passband (as found by the *Swift* spectral analysis⁵), the 1 keV band is constructed using an extrapolation of the 10 keV flux density curve at the times where the photon index could be derived from the *Swift* burst analyzer hardness ratio analysis. We separated the observations in both bands into 29 time windows, fitting a Gaussian to the flux distribution of the observations in each time window. Its median value and standard deviation are used as the measure and error of the synthetic curve. The obtained synthetic light curve is presented in Fig. 1.

The *Insight*-HXMT/LE X-ray telescope (Zhang et al. 2020) detected the afterglow emission of GRB 221009A at late times from about 9.8 h to 3 d after the *Fermi*/GBM trigger time, including two scanning observations (P050124003601 & P050124003701) and 20 pointing observations ranging from P051435500101 to P051435500401 with a total good-time-interval of 24 ks. The first two points are obtained by the spectral fitting of two scanning observations. The spectrum is obtained from the data when the target appears in the FoV. Unlike the pointing observations, the background is not obtained by the background model but from a region with no bright source in the FoV. Moreover, the instrumental response is calculated with the target track in the FoV and the Point Spread Function (PSF) of the *Insight*-HXMT/LE collimator. For the pointing observations, we use the *Insight*-HXMT Data Analysis software HXMTDAS v2.05⁶ to extract the light curves, spectra and background following the recommended procedure of the *Insight*-HXMT Data Reduction for HXMT-LE analysis. For both the scanning and pointing observations, the spectra of *Insight*-HXMT/LE in the 1.5 – 10 keV range are fitted by an absorbed power-law, i.e., $\text{tbabs}^*\text{power}$ in XSPEC. The *HXMT/LE* X-ray afterglow is shown in comparison to the *Swift*/XRT measurements in Fig. 1.

The *HXMT/LE* flux measurements are not corrected for the dust echo scattering (see for example, Negro

³ <https://grandma.ijclab.in2p3.fr>

⁴ <https://www.swift.ac.uk/>

⁵ https://www.swift.ac.uk/xrt_spectra/01126853/

⁶ <http://hxmtweb.ihep.ac.cn/>

et al. 2023; Williams et al. 2023; Tiengo et al. 2023) since Insight-HXMT is a collimated telescope with a large field of view, e.g., $1^\circ \times 4^\circ$. It is thus not possible to easily remove the dust echo scattering flux contribution. However, to evaluate the apparent flux increase caused by the dust scattering echoes we employed a similar procedure than the one adopted on the NICER data (Williams et al. 2023). As the dust scattering only dominates at energies below 4 keV, we first restricted the energy range to 4-8 keV. As a mild change of the spectral shape is observed during our *Insight*-HXMT observations (Williams et al. 2023), we used the spectral model of *Swift*/XRT with a fixed Galactic/intrinsic N_{H} and photon index ($\Gamma=1.8$) to fit the spectra. For the first several pointing data, the derived unabsorbed fluxes above in the 1.5-10 keV energy range are then consistent with the interpolated fluxes of *Swift*/XRT at the same times, which are about 10% lower than the uncorrected/dust-echo-included fluxes. However, for the last several pointing data, the combination of the low counts rate of the source and the high background level prevents us from correcting the fluxes caused by dust scattering echoes. To keep all *HXMT* fluxes produced in the same way, only the uncorrected dust echos scattering fluxes are given for all the data of LE. Therefore, these fluxes are systematically brighter (about 10%) than that derived from *Swift*/XRT at early (<0.5 d) times. We also notice that the flux difference between *Insight*-*HXMT*/LE and *Swift*/XRT narrows as time goes, which could be due to the fading of the dust scattering echoes.

2.2. Optical observations during the GRB prompt emission

We used the images taken from two sites managed by the Desert Fireball Network (Towner et al. 2020) at Mundrabilla (lon = 127.8486° E, lat = 31.8356° S, altitude = 84 m) and at Raw War Road (lon = 125.7503° E, lat = 29.7422° S, altitude = 215 m), Western Australia. The acquisition devices are constituted of a Nikon D810 (color CFA matrix) set at 3200 ISO with Samyang 8mm F/3.5 optics. This provides images covering the full sky. Images have 27 s exposure time taken every 30 seconds for the entire night. At the prompt time the GRB is located at elevations of 15° and 17° above the local horizons of Mundrabilla and Raw War Road, respectively. The sky at Mundrabilla was partially covered by thin clouds and there was bright moonlight. Weather and elevation conditions were better at Raw War Road. We analyzed the archive images taken between $t_{\text{GRB}} - 30$ s and $t_{\text{GRB}} + 500$ s. There is no detection at the position of the GRB to a limiting magnitude of 3.8 mag in the Green filter (which is roughly compat-

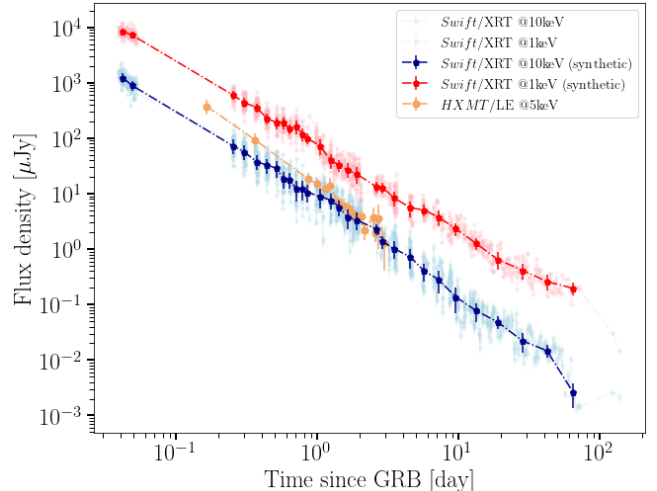


Figure 1. The unabsorbed X-ray light curve of GRB 221009A detected by the *Swift*/XRT (given at 10 keV in blue and 1 keV in red) and the *HXMT*/LE (orange) instruments. The light curves were corrected for Galactic and intrinsic N_{H} I column density absorption estimated from the late-time *Swift*/XRT spectrum analysis (https://www.swift.ac.uk/xrt_spectra/01126853/). In dark blue and red colors, we show our synthetic *Swift*/XRT light curve that we finally used in our afterglow modeling analysis, see the sections 3.4.2 and 3.4.1.

ible with Johnson *V*) at Raw War Road. The limits are shallower at Mundrabilla. Time and magnitudes in the AB system are reported in Table 5 corrected for extinction and in the Appendix, Table 6 uncorrected for extinction. No other contemporaneous observations have been reported, so to our knowledge, these are unique.

2.3. Optical post-GRB observations

Our first observation of the GRB within GRANDMA was obtained with the TAROT-Réunion telescope (TRE) at 2022-10-09T15:34:41 UTC (2:20 hr after T_0) thanks to its automated program following GRBs. Although GRANDMA was not conducting an observational campaign at the time of event, by the request of A. de Ugarte Postigo, the GRANDMA network was activated to observe about 1 day post-trigger time; at this point, we provided the network the *Swift* UVOT coordinates (Dichiara et al. 2022b). The first ToO image requested by GRANDMA was taken by the 60 cm telescope from Maidanak ~ 90 min after the notification at 2022-10-10T14:56:43 UTC (1.08 d after the GBM trigger) with the R_C filter. Our last observations were made by the Canada-France-Hawaii Telescope (CFHT) equipped with Megacam at 2022-10-29T06:32 (19 d, 17 hr post T_0). In total, we collected about 80 images (usually consisting of stacks of short exposures) from 15 GRANDMA partner telescopes. In successive order,

we provide here the mid-time of the first observation relative to T_0 for each telescope and the filters used during the whole campaign: D810 (before and during the prompt emission in V band) at Mundrabilla and Raw War Road observatories, TAROT-Réunion (0.0972 d, without filter) near Les Makes Observatory, UBAI-ST60 (1.0813 d in R_C) at Maidanak Observatory, KAO (1.1368 d in $g'r'i'z'$) at Kottamia Observatory, ShAO-T60 (1.1465 d in VR_C) at Shamakhy Observatory, AZT-8 (1.2274 d in $R_C I_C$) at Lisnyky observatory, HAO (1.2563 d without filter) at Oukaimenden observatory, MOSS (1.2722 d without filter) at Oukaimenden Observatory, C2PU-Omicron (1.3077 d in r') at Calern observatory, SNOVA (2.1535 d without filter) at Nanshan Observatory, T70 (2.2424 d in I_C) at Abastumani Observatory, UBAI-AZT22 (11.1313 d in R_C) at Maidanak Observatory, VIRT (12.4567 d in $R_C I_C$) at Etelman Observatory, and CFHT-Megacam (19.6945 d in $g'r'i'z'$) at Mauna Kea Observatory. Our preliminary analysis of the GRANDMA observations has been reported by [Rajabov et al. \(2022\)](#) where we reported observations from UBAI-ST60, KAO, Lisnyky-AZT-8, MOSS, C2PU-Omicron and SNOVA. In general, the sensitivity of the observations at the earliest epochs was reduced by the full moon.

In addition to the professional network, GRANDMA activated its [Kilonova-Catcher](#) (KNC) citizen science program for further observations. Our web portal was used to provide coordinates of the *Swift* UVOT source. Some amateur astronomers participating in the program observed the source by their own volition and distributed their own reports to the astronomical community ([Broens 2022](#); [Romanov 2022a,b,c](#); [Aguerre et al. 2022](#)). They also transferred their images to our web portal to allow us to perform our own image reduction and analysis. In total more than 250 images were uploaded to our web portal. Here we provide the list of the names of the telescopes (see [Tables 5 and 6](#) for the images selected for photometric analysis): a Celestron C11-Edge telescope, iT11 and iT21 iTelescopes, the IRIS 0.68m telescope, the Celestron EdgeHD14, the 12" MEADE telescope at the RIT Observatory, the C11 Dauban MSXD Telescope, the 0.53-m Ritchey-Chretien telescope of Montarrenti Observatory, the OMEGON200F5Newton telescope, a Newton SW 200/1000 telescope, a Newton 250 f/4 telescope, a Celestron 11 ATLAS telescope, the T-CAT telescope at the Crous des Gats Observatory, the iT24 iTelescope of the Sierra Remote Observatory and the 0.61-m Dall-Kirkham telescope of Burke-Gaffney Observatory, the 0.28m Mol SCT, the LCO 0.4m telescope at the McDonald Observatory, a Celestron C11 Millery telescope;

the Planewave CDK-14 telescope at the Contern Observatory. The observations started 0.25 to ~ 6 days after the trigger time, predominantly in Johnson-Cousins and Sloan filter sets, but also with other filters, such as *Lumen* or Bayer sensors.

The GRANDMA observations are listed in [Tables 5 and 6](#). The former reports the mid-time (in ISO format with post-trigger delay) and extinction-corrected brightness (in AB magnitudes) of the observations, while the latter includes the uncorrected magnitudes and references to selected online GCN reports (see [public observational reports](#), individual GCNs are all cited in the table). The mid-time is calculated as the weighted average of the observation start time and the number of exposures. The number of exposures is also provided. Our method for calculating magnitudes is described in the following section, and images that did not meet our criteria are labeled as “VETO”. In [Table 6](#), the reference catalogs and stars used by external teams for comparison are also included, unless not specified in the GCN reports. When the information is not provided by the online GCN report, we mark it as “-”.

2.4. Photometric methods

We required all GRANDMA images to be pre-processed by the telescope teams with bias or dark subtraction and flat-fielding. We reject a few images from amateur astronomers where these corrections were not performed. Some teams uploaded their images with their own astrometric calibration, but for most images the astrometric calibration is obtained directly from the Astrometry.net website. Then, two methods are used to measure the magnitude on the template-subtracted images (see below): STDpipe and MUPHOTEN. For both of these methods, we use techniques to blindly search for new detections within the *Swift* UVOT error localization ([Dichiara et al. 2022b](#)), but we can also force photometry at the GRB 221009A afterglow coordinates we fixed to RA = 288.2646558, Dec. = 19.7733650 ([Atri et al. 2022](#)).

STDpipe – The Simple Transient Detection Pipeline STDPIPE ([Karpov 2021](#)), is a set of python libraries aimed at performing astrometry, photometry and transient detection tasks on optical images. To do so, it uses several external algorithms such as SEXTRACTOR ([Bertin & Arnouts 1996](#)) for the source extraction, catalog cross-matching tools using the CDS Xmatch service developed at the Strasbourg Astronomical Observatory ([Boch et al. 2012](#); [Pineau et al. 2020](#)), the HOTPANTS code ([Becker 2015](#)) for image subtraction tasks

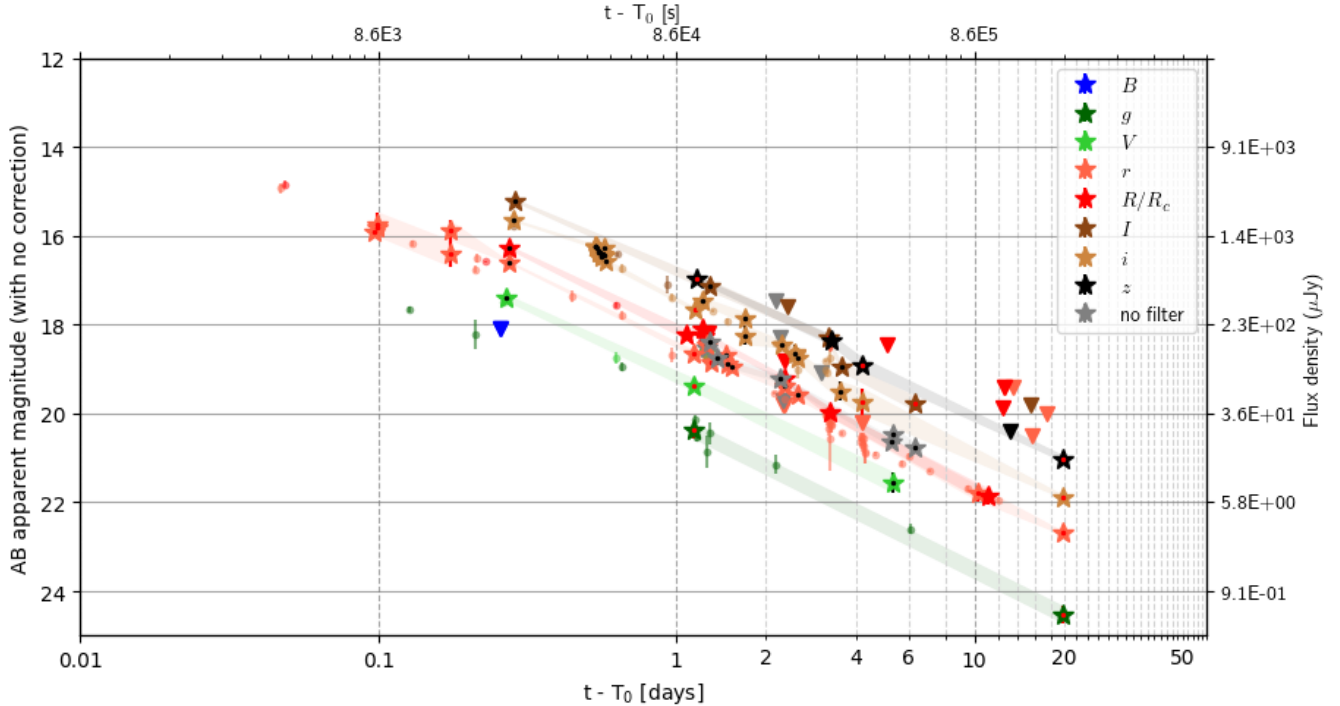


Figure 2. The optical afterglow of GRB 221009A was observed using $g'Vr'R_Ci'ICz'$ filters and without filter, with data points shown in the observer frame. The selected optical GCN data we use are represented by dots and the GRANDMA data measurements and upper limits are indicated by larger stars and downward-pointing triangles (see Table 6). The red points within the stars indicate measurements made by professional observers, while black points represent observations made by KNC observers. Only magnitude measurements with at least a 3σ detection significance are included (the upper limits being given at 5σ significance), with uncertainty regions shown as shading. The measurements are not corrected for any extinction.

and the PHOTUTILS⁷ Astropy package (Bradley et al. 2021) to perform photometric calibration and measurements. More details about the STDPIPE software architecture can be found in the git documentation⁸. In order to increase the signal-to-noise ratio of some KNC images where the GRB afterglow was barely visible, we resampled and coadded individual frames using the SWARP software (Bertin 2010). Our final set of science images were subtracted with Pan-STARRS DR1 catalog (PS1, Chambers et al. 2016) images downloaded from the CDS HiPS2FITS service (Boch et al. 2020) and rescaled to each image pixel scale. Forced aperture photometry was then applied at the GRB afterglow position in the residual images in order to limit the flux contribution from the very nearby stars. Due to the heterogeneity of the KNC instruments, we had a wide pixel scale distribution in our images. Therefore, the aperture radius was fixed per image to the average FWHM of stars detected at $S/N > 5$ by SEXTRACTOR in the image field. Depending on the photometric system used by KNC astronomers, the photometric calibration was done with the stars in

the image field either using the native photometric bands ($g'r'i'z'$) of the PS1 catalog or by converting them into the Johnson-Cousins BVR_CIC system using the transformation described by Pancino et al. (2022). The photometric model for the calibrated magnitudes, mag_{cal} , is defined following method described in Karpov (2021):

$$\text{mag}_{\text{cal}} = -2.5 \log_{10}(\text{ADU}) + \text{ZP}(x, y) + C \times (B - V) \quad (1)$$

where ADU is the star flux measured by the detector, ZP is the spatially varying Zero Point function and C is a color correction term to take into account the color distribution of the PS1 calibration stars. The ZP distribution is estimated by performing an iterative weighted linear least square fit to match the photometric model given in Equation 1 to the catalogued magnitudes. 3σ outliers to our photometric model were iteratively rejected (sigma clipping). The statistical errors on the ZP distribution were then propagated to the magnitude errors. Additional systematic errors due to the magnitude system conversion are also taken into account and can affect our measured magnitude up to 0.1 mag at maximum depending on the source brightness. Our KNC photometric results are shown in Table 5 and 6. As an illustration we show in Figure 3 one of the analysed KNC images according to the method described above.

⁷ <https://github.com/astropy/photutils>

⁸ <https://github.com/karpov-sv/stdpipe>

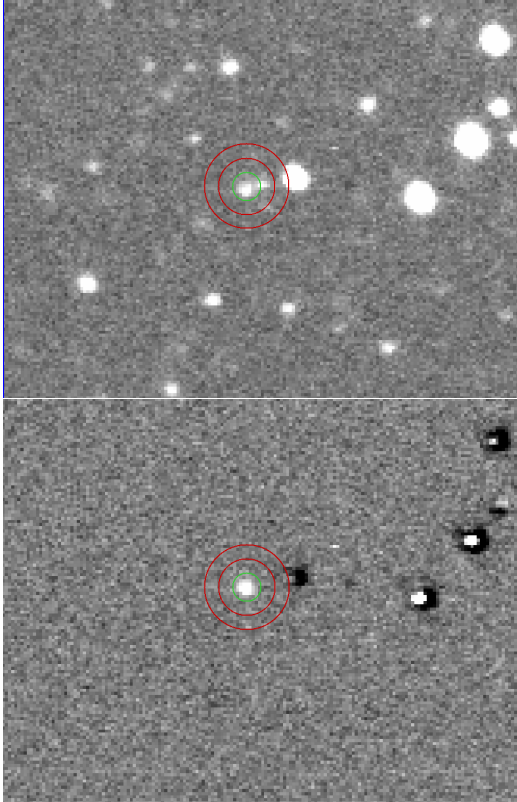


Figure 3. **Top panel:** A 60 s exposure I_c of GRB 221009A taken on the 0.61-m Dall-Kirkham458 telescope of the Burke-Gaffney Observatory ~ 0.5 days after the Fermi GBM trigger time. **Bottom panel:** The corresponding difference image using a PS1 template image downloaded from the CDS HiPS2FITS service. The optical afterglow is well-detected in the residual image and cleaned of any nearby star contribution. The aperture radii (the flux aperture in green and the background flux annulus in red) used to compute the photometric measurement are also shown in green in both images.

MUPHOTEN – MUPHOTEN⁹ is a Python-based software dedicated to photometry of transients observed by heterogeneous instruments, developed for the analysis of GRANDMA images (Duverne et al. 2022). Similarly to STDPipe, it uses Python libraries like PHOTUTILS (Bradley et al. 2021) and external algorithms like SEXTRACTOR (Bertin & Arnouts 1996) and HOTPANTS (Becker 2015). The MUPHOTEN software was utilized for the analysis of all GRANDMA images and a portion of KNC images. We first construct a template image by mosaicking Pan-STARRS DR1 (PS1) archive images, matching the image FoV, and we use HOTPANTS to subtract the template from the image. We do this to limit the contamination from nearby objects, in a

field-of-view crowded due to its proximity to the Galactic plane. However, for a limited number of images, the template subtraction was unsuccessful due to non-convergence with HOTPANTS. Nevertheless, these images had adequate resolution to clearly distinguish the transient from neighboring sources, so they were retained for further analysis. The background is estimated using the method of SEXTRACTOR, in a mesh of 150×150 pixels by default (smaller grids were applied for images with rapidly varying backgrounds). The background and its standard deviation are interpolated to each pixel of the image and subtracted to obtain the final result. Sources are detected by identifying clusters of at least five neighboring pixels that exceed a threshold of 2σ above the background.

Next, we conducted isophotal photometry on all detected sources, measuring the flux and its corresponding error (obtained by integrating the squared flux error, computed by PHOTUTILS as background variation plus gain-adjusted Poisson noise, over the same elliptical aperture). The sources were cross-matched with the PS1 catalog, yielding the PS1 magnitudes of the matched sources in the corresponding filter. For images taken with Johnson-Cousins filters, we transformed the PS1 magnitudes to the observed filters using the conversion equations from Kostov & Bonev (2018). Unfiltered images were treated as if they were taken with the Cousins R_C filter and were processed using the same conversion equations. We construct a calibration scale by fitting the instrumental magnitude and PS1 magnitude using a first-order polynomial fit with iterative clipping of outliers (3σ away from the fit). We then compute calibrated magnitudes for all detected sources, sort them by distance to expected transient coordinates, and consider a source a detection if its coordinates match within five pixels. We also compute, for each source, the photometric error, adding contributions from the flux error measured above and from the calibration uncertainties. Due to crowding in the Galactic plane, we checked for neighboring objects affecting the automatically computed apertures, reducing them if necessary. Forced photometry using circular apertures of default radius 1.5 times the average FWHM of stars in the image was performed at the GRB coordinates in the absence of direct detection. This was calculated using the PSFEX software (Bertin 2011). Plotting circular apertures of increasing radius (1 to 10 pixels) and their corresponding measured fluxes, we could check whether the default aperture collected all the transient flux and not neighbouring sources, and manually correct its coordinates and radius when needed.

⁹ <https://gitlab.in2p3.fr/icare/MUPHOTEN>

Finally, MUPHOTEN assesses the sensitivity of the image with upper-limit estimations. In MUPHOTEN, upper limits are computed as global properties of the whole studied image. The default method outlined in Duverne et al. (2022) calculates the success rate of recovering PS1 objects based on 0.2 magnitude intervals and selects the faintest interval where more than 10% of PS1 objects in the field-of-view are detected in the image. In the case of images where there is a high detection rate up until the limit of the Pan-STARRS catalog, an alternative method defines the upper limit as the magnitude of the faintest source detected with a $\text{SNR} > 5$.

2.5. Extinction selection

Unfortunately for optical studies, the brightest GRB ever detected lies behind significant extinction near the Galactic plane ($b = 4.32^\circ$). Following the maps of SF11, the line-of-sight at the “reference pixel” lies behind $E_{(B-V)} = 1.32 \text{ mag}/A_V = 4.1 \text{ mag}$. However, at Galactic latitudes $|b| < 5^\circ$, the maps of Schlegel et al. (1998, which those of SF11 are based on) are known to be unreliable and may overestimate the extinction (Popowski et al. 2003, and references therein).

Rowles & Froebrich (2009, henceforth RF09) presented a method of determining extinction towards the Galactic plane using near-infrared color excess determinations based on 2MASS observations, following earlier work from Froebrich et al. (2005) based on stellar counts. Using their extinction calculator¹⁰ and the position of the GRB, we find a significantly lower extinction, using the 100NN (Nearest Neighbour, see RF09 for details) result (which has the highest S/N), of $A_V = 2.195 \text{ mag}$. Using the classical Milky Way extinction curve of Cardelli et al. (1989, henceforth CCM89), this translates into $E_{(B-V)} = 0.709 \text{ mag}$. The extinction maps of RF09 show that extinction toward this region of the Milky Way is smooth and quite homogeneous for several degrees around (and not high in the context of the potential extinction toward the Milky Way), the nearest pronounced molecular clouds with significantly higher extinction lie closer to the plane in the neighboring constellation Vulpecula, about 5° away. Therefore, we deem the use of the extinction curve of CCM89 to be valid.

The method of RF09 extends only¹¹ to 2 – 3 kpc. There is evidence for additional dust screens at larger distances, however. *Swift* XRT observations reveal expanding rings in the X-rays (Tiengo et al. 2022) arising from scattering on distant dust curtains. These authors

report the discovery of nine dust rings and derive the distances, with the most distant one lying at $3635 \pm 36 \text{ pc}$, potentially already beyond the detection range of the RF09 method. Observations with IXPE (Negro et al. 2023) confirm the most distant dust ring found by *Swift* at $3.75 \pm 0.0375 \text{ kpc}$, and report an even more distant dust curtain at $14.41 \pm 0.865 \text{ kpc}$. Recently, Vasilopoulos et al. (2023) reported a detailed analysis of *Swift* XRT data and also find evidence for dust out to 15 kpc (see Williams et al. 2023 for further analysis), and *XMM-Newton* analysis of a total of 20 dust rings presented by Tiengo et al. (2023) detects an even further dust curtain at $\approx 18.6 \text{ kpc}$.

The Galactic disc exhibits a warp (e.g., Hou & Han 2014, and references therein). The map derived by Hou & Han (2014, their Fig. 16) shows that at the Galactic longitude of GRB 221009A ($l = 52.96^\circ$), HII regions indeed extend up to several hundred pc “above” the Galactic plane. For the Galactic latitude of GRB 221009A ($b = 4.32^\circ$), the sightline lies $\approx 1100 \text{ pc}$ above the plane at a distance of 14.4 kpc, beyond the HII regions mapped by Hou & Han (2014). However, this does not rule out the existence of cold dust curtains even that high above the Galactic disc which would contribute extra extinction beyond the RF09 measurement. We therefore conclude the true extinction value along the line of sight to GRB 221009A lies in the interval of $A_V = 2.2 - 4.1 \text{ mag}$, and will discuss both extreme values.

3. MULTI-WAVELENGTH ANALYSIS OF THE AFTERGLOW

To analyze the afterglow light curve, we use data from multiple sources: Our own GRANDMA and KNC data (see Table 5), selected GCN data (see Table 6), as well as data published in Williams et al. (2023); Shrestha et al. (2023); Laskar et al. (2023); Levan et al. (2023); O’Connor et al. (2023). We especially note we use the *Hubble Space Telescope* (*HST*) data from Levan et al. (2023) where the host-galaxy contribution has been subtracted using *galfit*. Near-infrared observations are taken from Durbak et al. (2022); D’Avanzo et al. (2022); Huber et al. (2022); Ferro et al. (2022); O’Connor et al. (2023), as well as the *James Webb Space Telescope* (*JWST*) MIR F560W data point (Levan et al. 2023).

3.1. Empirical Light-Curve Analysis

With the exception of our shallow upper limits from Mundrabilla and Raw War Road, no optical observations have been reported before the *Swift* trigger.

The first observations, consisting of *Swift* UVOT data from Williams et al. (2023); Laskar et al. (2023) and ob-

¹⁰ https://astro.kent.ac.uk/~df/query_input.html

¹¹ Neckel & Klare (1980) give a value of $A_V = 3.3 \text{ mag}$ along this sightline out to 3 kpc.

tained via automatic analysis¹² as well as some ground-based observations (Belkin et al. 2022c; Xu et al. 2022), are found to decay more steeply than following observations (see Figure 11 in the Appendix), and also lie above the back-extrapolation of that data. This indicates an extra component in the light curve, potentially the tail end of a reverse-shock flash. The extreme intensity of the GRB makes it potentially possible that the early transient was extremely bright.

Fitting a joint multiband fit to the data, which assumes achromatic evolution and leaves only the normalization of each band an independent parameter, we derive a first decay slope of $\alpha_{steep} = 1.32 \pm 0.34$ (we define $F_\nu \propto t^{-\alpha} \nu^{-\beta}$), significantly steeper than the later decay observed from $\sim 0.09 < t < 0.59$ d, but quite shallow for a reverse-shock flash (Sari & Piran 1999; Kobayashi 2000). As the baseline is short, it is possible we are seeing the transition from the early, steeply decaying component to the later shallower light-curve decay, and the decay at even earlier times might have been steeper and more in accordance with a reverse-shock flash. Extrapolating this slope backward to the peak of the brightest gamma-ray flare of the prompt emission, at ≈ 220 s post-trigger, we find $R_{AB} \approx 11$ mag ($R_{AB} \approx 7.6$ mag when corrected for SF11 extinction). This value is far fainter than our Mundrabilla/Raw War Road exposures probe. A steeper decay (see as mentioned early in the paragraph) or an additional component directly associated with the prompt emission cannot be ruled out but would still be unlikely to be bright enough to be detected by our shallow all-sky observations.

Data at > 0.09 d can be fit with a smoothly broken power-law, with parameters pre-break slope α_1 , post-break slope α_2 , break time t_b in days, and break smoothness n . The very last data points at $\gtrsim 30$ d show a flattening that may result from the host galaxy becoming dominant, we exclude these data points from the analysis. We see no direct evidence of a SN component in the late light curve¹³, in agreement with Shrestha et al. (2023), similar to the case of GRB 030329 (e.g., Kann et al. 2006), and therefore also do not include such a component in the fit. A dedicated search will need well-calibrated late-time data. In general, the data shows dispersion, leading to a large χ^2 .

¹² https://swift.gsfc.nasa.gov/uvot_tdrss/1126853/index.html

¹³ Note that data presenting evidence of a photometric SN rise (Belkin et al. 2022a,b) were taken under inclement conditions and are likely the result of blending with nearby sources and are therefore too bright (A. Pozanenko, priv. comm.). However, Fulton et al. (2023) assume an intrinsic optical decay slope identical to the X-ray slope and interpret the more shallow decay as a rising, luminous SN component.

This fit results in $\alpha_1 = 0.722 \pm 0.012$, $\alpha_2 = 1.437 \pm 0.003$, with $\sim t_b = 0.6$, and a sharp break $n = 100$ fixed. Note that the errors of the fitted parameters are statistical only and do not include the systematic uncertainties ($\sim 10\%$) due to the inter-calibration of the different photometric bands. Therefore, they are simply presented for diagnostic purposes. This steepening had also been reported by D’Avanzo et al. (2022), who found $\alpha_1 \approx 0.8$, $\alpha_2 \approx 1.6$, and $t_b \approx 0.98$ d based on a significantly smaller data set. Shrestha et al. (2023) find $\alpha_1 = 0.64$, $\alpha_2 = 1.44$ in r' and $\alpha_1 = 0.81$, $\alpha_2 = 1.46$ in i' , similar to our result. Williams et al. (2023), using only *Swift* UVOT data, find $\alpha_{1,O} = 0.98^{+0.05}_{-0.11}$, $\alpha_{2,O} = 1.31^{+0.07}_{-0.05}$, and $t_{break,O} = 0.255^{+0.197}_{-0.127}$ d, in agreement with our results within 2σ . They point out this decay is clearly slower than that of the X-rays (see below), but is very unlikely to be influenced by a host or SN component.

Swift XRT observations (initially reported in Kennea et al. 2022b; Tohuvavohu et al. 2022, but these reports are based on the *Swift* trigger time) as given in the XRT repository (Evans et al. 2007, 2009) show the light curve¹⁴ to have multiple shallow breaks (see also Williams et al. 2023, who caution that especially during the WT mode observation, the dust-scattering rings can influence the light curve stemming from the atypical background around the afterglow PSF), but within the first ≈ 10 d, the decay slope is $\alpha_X \approx 1.5-1.6$, similar but steeper than our optical result. In their detailed analysis, Williams et al. (2023) find $\alpha_{1,X} = 1.498 \pm 0.004$, $\alpha_{2,X} = 1.672 \pm 0.008$, and $t_{break,X} = 0.914^{+0.127}_{-0.116}$ d. *Insight*-HXMT observations (Ge et al. 2022, see also An et al. 2023) also yielded a somewhat steeper slope $\alpha_X \approx 1.66$. NICER observations also find $\alpha_X \approx 1.6$ (Iwakiri et al. 2022). The significantly more shallow decay phase in the optical ($\alpha_O \approx 0.83$) as well as the earlier break at $t_b \approx 0.6$ d are not seen in X-rays at all. The optical light curve also shows a much stronger break with $\Delta\alpha_O = 0.617 \pm 0.013$ vs. $\Delta\alpha_X = 0.174 \pm 0.009$.

3.2. Analysis of the Spectral Energy Distribution

The normalizations derived from the joint multiband fit described in §3.1 yield a Spectral Energy Distribution, a very low-resolution “spectrum” of the afterglow that is nonetheless valuable to study the dust properties along the line-of-sight. The fit assumes achromaticity, i.e., no spectral evolution, and is therefore based on all data involved in the fit. Except for scaling, the SED is identical at any time point covered by the fit, the specific

¹⁴ https://www.swift.ac.uk/xrt_live_cat/01126853/

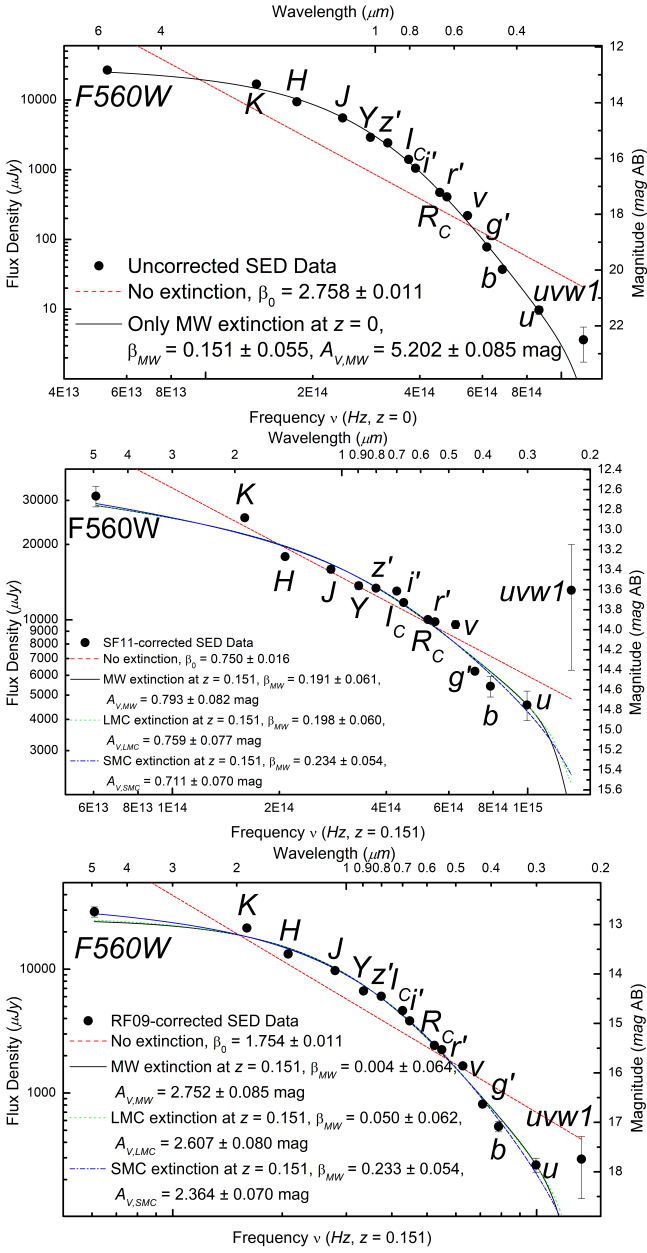


Figure 4. Analysis of the SED. **Top panel:** Fit to the uncorrected SED with a MW extinction model at $z = 0$, i.e., assuming no additional host-galaxy extinction. The fit is generally in agreement with the data, with the *uvw1* data point being brighter than the model. **Middle panel:** Fit to the SED after correcting it for SF11 foreground extinction and shifting it to $z = 0.151$. The correction leads to significant scatter, with the *uvw1* now being clearly brighter than any fit, even one without additional host-galaxy extinction. The three extinction laws can not be discerned from each other, but the potential bright *uvw1* emission makes the SMC law the preferred one. There is still significant curvature which implies additional significant host-galaxy extinction. **Bottom panel:** As the middle panel, with RF09 foreground extinction. The SED remains very red, and very high host extinction is implied. SMC extinction again leads to the most physical solution, but all dust laws are in conflict with the bluest *Swift* UVOT detection.

values are measured at break time. While our data does not indicate an obvious spectral evolution, such a break is hard to constrain due to the challenge of building an empirical model that describes the data well.

We fit the SED both without extinction (a simple power-law) as well as with Milky Way (MW), Large (LMC) and Small Magellanic Cloud (SMC) dust following the parametrization by Pei (1992). These fits are performed after correction for Galactic extinction, and we study both the RF09 and SF11 models. The derived SED shows scatter, with especially the z' band deviating and being too faint. The field is not covered by the Sloan Digital Sky Survey (e.g., Almeida et al. 2023, and references therein); however, many telescopes use filters which are close to the SDSS system. There are offsets to the Pan-STARRS system which was used for calibration in most cases. Following the Pan-STARRS to SDSS conversion of Tonry et al. (2012), we find $g'_{PS1} - g'_{SDSS} = -0.26$ mag, $r'_{PS1} - r'_{SDSS} = 0.02$ mag, $i'_{PS1} - i'_{SDSS} = 0.03$ mag, and $z'_{PS1} - z'_{SDSS} = 0.13$ mag, i.e., small changes for $r'i'$ but more significant changes to g' and z' . As we are unable to examine each measurement individually for more precise color terms, we just apply these offsets to the four data points in the SED, which leads to a marked reduction in scatter and χ^2 . However, scatter still remains, with especially the *H* band being fainter than the models and *K* band being brighter. The precise light-curve fit leads to these normalizations to have small errors, causing large χ^2 values that are not formally acceptable even for fits that generally model the SEDs well. The source of this scatter is less easy to understand than for the light-curve data points themselves, e.g., in the case of the *H* and *K* bands, most data points are from the final analyses presented in refereed papers (e.g., O'Connor et al. 2023), and the few GCN points have larger errors and do not disagree with the fit curves. Furthermore, these data span a long time period, e.g., from 0.23 d to 25.4 d for *H* and from 4.4 d to 25.4 d for *K*. This would imply all data from multiple sources are systematically offset in the same manner. As we have no immediate solution to this issue, we will continue to work with these results despite the fits being formally rejected, noting the scatter is approximately symmetric around the SED fit curves and not due to a clear discrepancy between model fit and data (as is the case for the fits without extinction which disregard the curvature of the SEDs).

3.2.1. Pure MW extinction

We first study the SED without applying any MW foreground correction, and taking the data at $z = 0$. The SED is very steep and shows evidence for curvature

(see Fig. 4, top panel). A simple power-law fit yields a spectral slope $\beta_0 = 2.758 \pm 0.011$. This is clearly not a good model, we find $\chi^2 = 8102$ for 13 degrees of freedom.

Applying MW dust to the SED yields a highly significant improvement ($\chi^2 = 142.8$ for twelve degrees of freedom, this number of degrees of freedom is identical for all extinction fits), and we derive $\beta = 0.323 \pm 0.086$, $A_{V,Gal} = 5.202 \pm 0.085$ mag ($E_{(B-V)} = 1.69 \pm 0.03$ mag). This value exceeds the SF11 correction by over a magnitude and can indicate two things: Either even the SF11 result does not encompass the entirety of the MW foreground extinction, or there is additional, significant host-galaxy extinction along the line-of-sight, or it is a combination of both at once. The detection of the Na I doublet at the redshift of the host galaxy (de Ugarte Postigo et al. 2022; Malesani et al. 2023) indicates there must be some amount of host-galaxy extinction. However, we note that the free fit already yields an intrinsic spectral slope lying in the typical range found for GRB afterglows, $\beta \sim 0.2 - 1.2$ (Kann et al. 2010).

3.2.2. SF11 extinction

We next correct the SED for SF11 MW extinction and now study the pure host extinction at $z = 0.151$. After this correction, the spectral slope is obviously much flatter than before ($\beta_{0,SF11} = 0.750 \pm 0.016$, $\chi^2 = 207$ for 13 degrees of freedom), however, the SED shows remaining significant curvature as well as scatter (see Fig. 4, middle panel), with especially the *uvw1* band deviating. We caution this color is derived using only two r'/R_C -band GCN points, which yields additional uncertainty, beyond the fact that it is only a 2σ excess above the background, and thus barely a confident detection. If real, the *uvw1* band detection (Williams et al. 2023) coincides with the 2175 Å bump feature for LMC and MW dust in the host-galaxy rest frame, indicating the host-galaxy extinction law is most likely similar to SMC dust which lacks this feature almost completely. Mathematically, the different results can not be distinguished ($\chi^2 = 128, 125, 116$ for MW, LMC, and SMC dust, respectively; see also Williams et al. 2023), but SMC dust yields the overall most logical result, with an intrinsic spectral slope very close to the MW-only fit ($\beta_{SF11,SMC} = 0.234 \pm 0.054$) and moderately high additional host-frame extinction ($A_{V,SF11,SMC} = 0.711 \pm 0.070$ mag, $E_{(B-V)} = 0.243 \pm 0.024$ mag). In terms of the intrinsic spectral slope, our results are in good agreement with those of Levan et al. (2023), who give several results in the slope range of $\beta = 0.3 - 0.4$, but especially a broadband fit using *JWST* and Gran Telescopio Canarias spectra as well as NOEMA sub-mm data which yields $\beta = 0.362$. They attribute most

extinction to the Milky Way and find only very small host-galaxy extinction. Modeling these data together with XRT, they find evidence for a spectral break between the optical and X-ray bands, but not for a spectral break within the optical/NIR regime itself. Using only *Swift* UVOT data, Williams et al. (2023) derive higher values: Correcting for the higher foreground extinction given by Schlegel et al. (1998) and using an intrinsic slope of $\beta = 0.7$, they find $E_{(B-V)} = 0.51 \pm 0.03$ mag for SMC dust.

3.2.3. RF09 extinction

Finally, for the lowest assumed MW extinction, that of RF09, we find a combination of “moderately high” MW extinction and “moderately high” host-galaxy extinction. The SED after RF09 correction is still very steep (see Fig. 4, bottom panel, we find $\beta_{0,SF11} = 1.754 \pm 0.011$, $\chi^2 = 2300$). Again the three dust models yield similar goodness-of-fit values ($\chi^2 = 161, 152, 123$ for MW, LMC, and SMC dust, respectively, but in this case, the very flat intrinsic spectral slopes $\beta \approx 0.0 - 0.1$ additionally speak against MW and LMC dust being the correct solution. SMC dust results in $\beta_{RF09,SMC} = 0.233 \pm 0.054$, $A_{V,RF09,SMC} = 2.364 \pm 0.070$ mag. Even this result is not in agreement with the *uvw1* detection, however.

Overall, while there is no strong evidence for one or another foreground extinction, the most logical solution is SF11 foreground extinction with additional moderately high SMC extinction in the host galaxy. High host-galaxy extinction such as in the RF09 case is also not supported by the relatively small equivalent width of the Na doublet at the host redshift (Malesani et al. 2023). In general, given the poor performance of the fits, it seems like that the extinction law is different from the three canonical functions used above, or the spectrum cannot be approximated as a power-law; however, for the sake of the analysis, for both foreground extinction scenarios, we corrected our data for Galactic extinction and host-galaxy extinction. During this step, we accounted for the systematic uncertainties of our extinction estimate in each band, adding them to the photometric errors of Table 6. These fully-corrected data sets are shown in Table 5.

3.3. The afterglow of GRB 221009A in a global context - luminous but not intrinsically extraordinary

With knowledge of the intrinsic extinction and the redshift, and using the method first presented in Kann et al. (2006), we are able to place the optical/NIR afterglow of GRB 221009A in the context of a large sample of GRB afterglows. The sample is compiled from Kann et al. (2006, 2010, 2011, Kann et al. 2023a,b in prep.). These

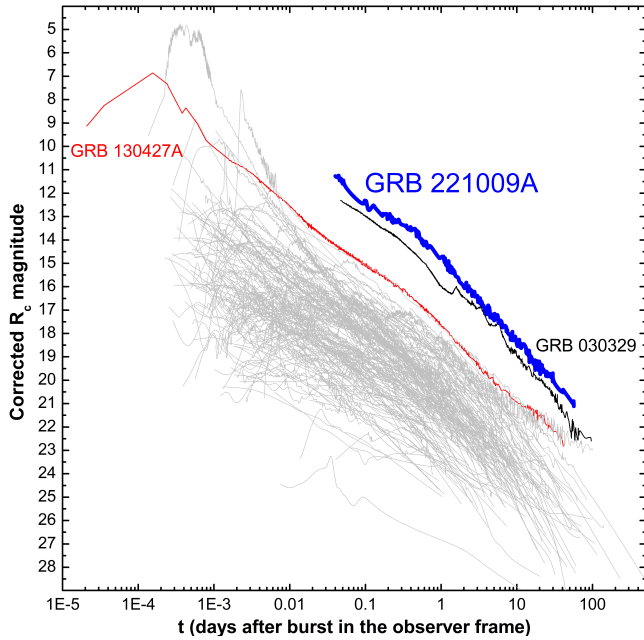


Figure 5. The afterglow light curve of GRB 221009A in context of a large sample of GRB afterglows (Kann et al. 2006, 2010, 2011, 2023a,b in prep.). These data have been corrected for Galactic extinction along each individual line-of-sight, and if possible for the host-galaxy and SN contribution. For the GRB 221009A afterglow, we show the result for SF11 Galactic extinction. We highlight the afterglows of two other GRBs, namely that of the much less energetic but similarly distant GRB 030329, and that of the well-studied, ultra-bright GRB 130427A, which had been the closest highly energetic (“cosmological”) GRB so far. Assuming the higher extinction correction, the afterglow of GRB 221009A is seen to be the brightest that has ever been detected, even brighter than the afterglow of GRB 030329, however, by only a small margin.

afterglows have been corrected for individual Galactic foreground extinction, host-galaxy contribution (where known) and SN contribution at late times (where applicable).

The otherwise as-observed light curves are shown in Fig. 5. We highlight the afterglows of the two exceptional GRBs mentioned in the introduction. For one, the nearby but only moderately energetic GRB 030329, whose afterglow (e.g., Lipkin et al. 2004; Kann et al. 2006) remains the most well-observed until this day, and is seen to be brighter than all other afterglows in the sample at any given time. And secondly the afterglow of the extremely bright GRB 130427A (e.g., Vestrand et al. 2014; Perley et al. 2014, Kann et al. 2023b, in prep.), also among the brightest observed GRB afterglows and energetically more similar to GRB 221009A.

The placement of the afterglow of GRB 221009A depends on the MW foreground extinction correction.

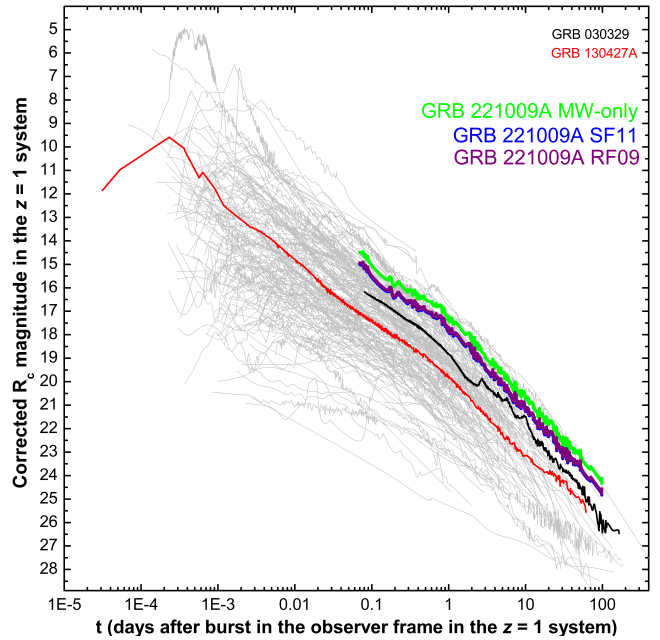


Figure 6. The same as Fig. 5, but now all afterglows are in the $z = 1$ system. This means that the afterglow magnitudes have been additionally corrected for host-galaxy extinction, and all of them have been shifted to $z = 1$ taking the individual spectral slopes β and cosmological k -correction into account. We again highlight the afterglows of the bright nearby GRBs 030329 and 130427A, and three solutions for GRB 221009A: The pure MW solution, SF11 MW extinction, and RF09 MW extinction along with the respective host-galaxy solutions. All yield similar brightness, with the SF11 and RF09 results essentially overlapping (offset by only 0.05 mag), and the afterglow is seen to be among the more luminous ones detected so far. We note that the late afterglow of GRB 221009A is *not* corrected for a potential SN contribution and therefore the luminosity may be overestimated.

From our three models, we display the SF11 solution here, which is usually the standard correction for extinction in other cases. If we use the MW-only solution, the resultant afterglow would be even brighter, whereas it would be magnitudes fainter with the RF09 solution, but as pointed out, this solution is unlikely. For SF11, we see the observed afterglow is even brighter than that of GRB 030329 at all times (albeit usually by not more than one magnitude) - potentially, yet another record that GRB 221009A holds. Williams et al. (2023) report the observed afterglow of GRB 221009A is by far the brightest X-ray afterglow, and also the brightest UVOT afterglow (after extinction correction) ever detected.

A better afterglow comparison can be achieved if we correct both for the distance (temporally and in terms of luminosity, we choose to place all afterglows at $z = 1$ and present them in the observer frame) as well as for any intrinsic (host-galaxy) extinction. If the latter

value is high, it can hide extremely luminous GRB afterglows from initially looking extraordinary (e.g., GRB 080607, Perley et al. 2011). The results are shown in Fig. 6. It can now be seen that the afterglow of GRB 130427A is only of medium brightness, and that of GRB 030329, while brighter, is also well within the sample of known afterglows. The same is true for the afterglow of GRB 221009A. The three foreground-extinction solutions yield similar results now, as high foreground extinction implies low additional host-galaxy extinction (MW-only, SF11), while the lower RF09 foreground extinction is mostly compensated by necessary high intrinsic extinction. Indeed, the degeneracy between the foreground and host-galaxy extinction, which stems from the very low redshift of the event, leads to the completely corrected light curves for the SF11 and RF09 extinction to almost overlap, the offset is only 0.05 mag. This motivates us to only use the SF11 solution for numerical modelling (see §§3.4.1, 3.4.2.) The afterglow of GRB 221009A is clearly among the more luminous detected so far, but it is not egregious. Only at late times does the unbroken decay lead it to become exceptional, but we caution these observations are not corrected for host-galaxy and SN contribution and are therefore to be taken with caution (see Fulton et al. 2023 for the potential SN contribution, but see also Shrestha et al. 2023).

Quantitatively, we determine the $z = 1$ magnitudes of a sample of 170 GRB afterglow light curves including that of GRB 221009A, where not every afterglow has measurements at the chosen time (however, the GRB 221009A afterglow does). As times, we chose 0.07 d, 0.5 d, 1 d, 5 d, 10 d, and 20 d. For these times, the comparison sample encompasses 140, 144, 130, 78, 52, and 34 other afterglows, respectively. We find the afterglow of GRB 221009A is brighter than 83.6%, 86.1%, 83.8%, 87.2%, 88.5%, and 85.3% of all other afterglows, respectively. More generally, it is brighter than 80% – 90%, which supports our claim that it is not exceptional in the way the prompt emission energetics are. However, it is extraordinary indeed in one aspect. As an example, at one day after trigger (12 hr in the rest-frame), there are 20 afterglows found to be brighter than that of GRB 221009A, but none of these lie at $z < 1.4$, and 15 lie at $z > 2$. In all time slices, the single afterglow at $z < 1$ found to be brighter (at 0.5 d and 2 d, but not 1 d) is that of GRB 110715A at $z = 0.8225$ (Sánchez-Ramírez et al. 2017, , Kann et al. 2023a, in prep.).

Overall, despite its extreme energetics, the optical/NIR afterglow of GRB 221009A is not intrinsically extraordinary compared to the global sample of known afterglows, a phenomenon also seen for other highly

energetic GRBs like GRB 990123 (Kann et al. 2010). Williams et al. (2023) reach similar conclusions, for both the UVOT and the X-ray afterglow, and Laskar et al. (2023) show this is true as well for the radio afterglow.

3.4. Properties of the GRB afterglow from Bayesian Inference

We analysed our data in the framework of the standard afterglow model where the observed emission is dominated by the synchrotron radiation from shock-accelerated electrons at the forward external shock due to the deceleration of a relativistic jet by the ambient medium (assumed here to be uniform). We explored the allowed parameter space of this model with a Bayesian approach using the constraints provided by two distinct data sets. Both data sets include X-ray data from the *Swift*/XRT instrument (at 1 keV and 10 keV), following the procedure outlined in §2.1 and downsampling the data to avoid our Bayesian inference runs being entirely dominated by X-ray observations. These data were combined with *HXMT*-LE data at 5 keV. We then combine the *Swift*-XRT and *HXMT* X-ray data with two different optical data sets: (i) GRANDMA data points in the optical and near-infrared (presented in §2.2 and §2.3), simply completed in u-band by early *Swift*-UVOT points. We denote this set as “GRANDMA”. (ii) We enrich the “GRANDMA” data with the same observations collected in the literature as already used in the introduction of §3. This full data set has the advantage of including J , H , K , and $F560W$ in our analysis, increase the existing optical data, and extend the observations up to nearly 60 days. We denote this set as “Extended”. Both sets are corrected for extinction using the SF11 assumption for the foreground extinction, see §3.2. We made the choice not to take into account any radio data, as only a subset was publicly available at the time of the publication of the article (e.g. data from Laskar et al. 2023 was not yet available). For these two multi-wavelength data sets and for both Bayesian Inference presented below, we use the same parameter space and priors, presented in table 1, except for the initial Lorentz factor Γ_0 , which is needed only in the second model including the coasting phase. The luminosity distance to the source is fixed to $D_L = 742$ Mpc, corresponding to a redshift $z = 0.151$ for a flat cosmology with $H_0 = 67.7 \text{ km} \cdot \text{s}^{-1} \cdot \text{Mpc}^{-1}$ and $\Omega_m = 0.307$ (Planck Collaboration et al. 2016).

3.4.1. Bayesian Inference using NMMA, investigation of the jet structure and SN contribution

As a further framework to interpret GRB 221009A, we use the Nuclear physics and Multi-Messenger Astronomy framework NMMA (Dietrich et al. 2020; Pang et al.

2022)¹⁵ that allows us to perform joint Bayesian inference of multi-messenger events containing gravitational waves, kilonovae, SNe, and GRB afterglows. We have analyzed both the *GRANDMA* and *Extended* data sets with NMMA.

For this work, we follow Kunert et al. (2023) and employ first the top-hat jet structure (with on axis-assumption and with a free case) with the semi-analytic code *afterglowpy* (van Eerten et al. 2010; Ryan et al. 2020).¹⁶ In this model, the dynamics of the relativistic ejecta propagating through the interstellar medium are treated under the thin-shell approximation, and the angular structure is introduced by dissecting the blast wave into angular elements, each of which is evolved independently, including lateral expansion. Magnetic-field amplification, electron acceleration, and the synchrotron emission from the forward shock are treated according to the analytical prescriptions of Sari et al. (1998). The observed radiation is computed by performing equal-time arrival surface integration. It is important to note that the model does not account for the presence of the reverse shock or the early coasting phase and does not include inverse Compton radiation. This limits its applicability to the early afterglow of very bright GRBs.

While we find a more steeply decaying emission component at early times, it is unclear whether it can be attributed to the reverse shock emission Laskar et al. 2023.

The advantage of the NMMA framework is the possibility of comparing different astrophysical scenarios and models in a straightforward way. As a starting point, we compare different jet structures. In addition to the top-hat jet, we also employed a Gaussian and Power-law jet. Gaussian jet features an angular dependence $E(\theta_{\text{obs}}) \propto \exp(-\theta_{\text{obs}}^2/(2\theta_w^2))$ for $\theta_{\text{obs}} \leq \theta_w$, with θ_w being an additional free parameter. The power-law jet features an angular dependence $E(\theta_{\text{obs}}) \propto (1 + (\theta_{\text{obs}}/\theta_c)^2/b)^{-b/2}$ for $\theta_{\text{obs}} \leq \theta_w$, with θ_w and b being an additional parameter.

We present our best-fit light curves for the SF11 extinction, with different jet structures assumed in Fig. 7, which shows the *GRANDMA* data (see Fig. 12 in the Appendix for the *Extended* data).

We find that the observational data are only moderately well-fit by the model. While the *r*-band lightcurve is reasonably well-recovered, the predicted lightcurves

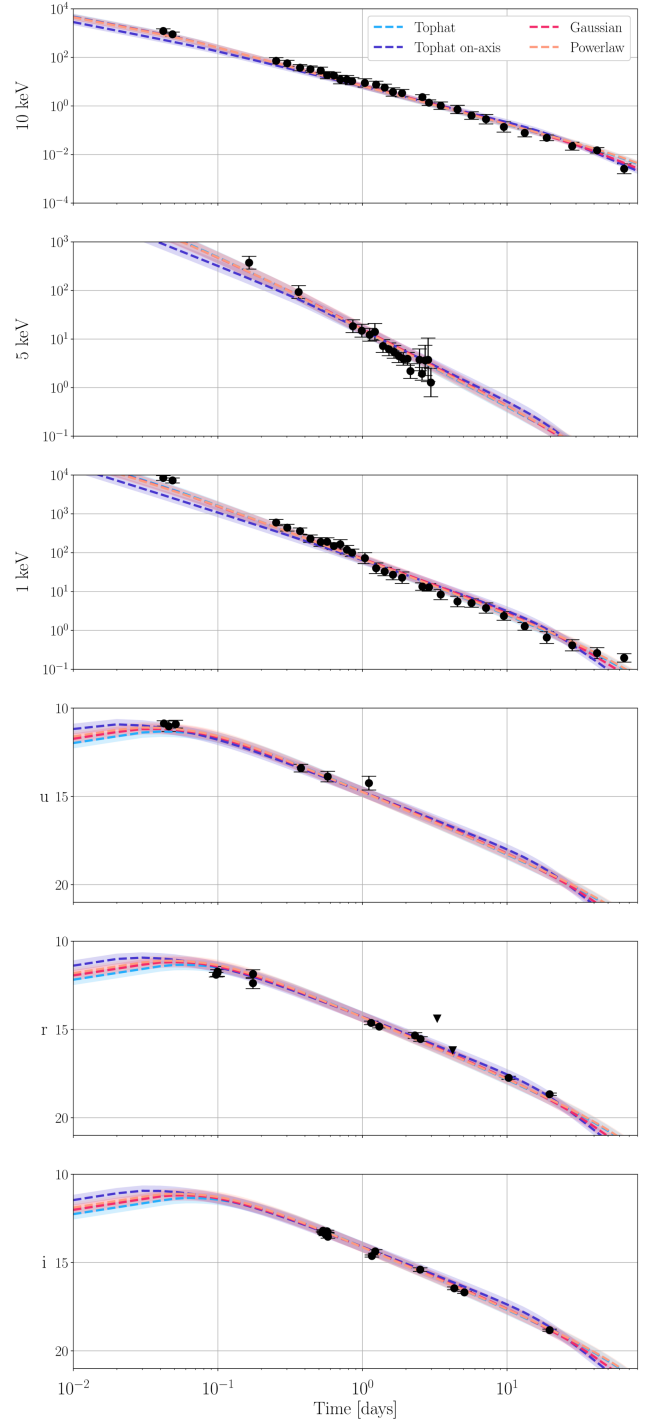


Figure 7. NMMA - Observational data (*GRANDMA* data) and best-fit light curves of selected filters for the NMMA analysis using the SF11 extinction and the four employed jet structures. The X-ray bands are shown in μJy and the rest of the bands are shown in AB magnitude.

at higher frequencies, especially in X-rays, cannot reproduce the observed evolution.

¹⁵ <https://github.com/nuclear-multimessenger-astronomy/nmma>

¹⁶ The nested sampling algorithm implemented in PYMULTINEST (Buchner 2016) is used.

We present the corresponding source parameters, namely, the inclination angle θ_{obs} , isotropic energy E_0 , the interstellar medium density n_{ism} , half-opening angle of the jet core θ_{core} , and microphysical parameters $\{p, \epsilon_e, \epsilon_B, \zeta\}$ (the power-law index of the electron energy distribution, the fraction of energy in electrons, the fraction of energy in the magnetic field and the fraction of electron accelerated, respectively) using the four different jet structure models in Fig. 8, which uses the *GRANDMA* data (see Fig. 13 in the Appendix for the *Extended* data); each simulation uses 2048 live points for the nested sampling. The full posteriors can be found in Tab. 1.

Most surprising in our analysis might be the relatively large jet-opening angle (the viewing angle being near the edge but still within the jet), which might be hard to explain given the high isotropic energy release of the GRB. For the tophat on-axis (i.e. $\theta_{\text{obs}} = 0$), the light curve seems dimmer than expected for the X-ray data, which drives the analysis to prefer larger viewing angles. Although a larger viewing is preferred, the relation of $\theta_{\text{obs}} < \theta_{\text{core}}$ is clearly observed in the posterior of the angle ratio $\theta_{\text{obs}}/\theta_{\text{core}}$ (in Tab. 1), which is attributed to the absence of the jet break in the present data. We also provide the $\chi^2/\text{d.o.f.}$ for these fits in Tab. 3

Finally, following the study of [Fulton et al. \(2023\)](#), we investigate the possibility of an SN connected to GRB 221009A. For modeling the SN, we use the **nugent-hyper** model from **sncosmo** ([Levan et al. 2005](#)) with a shift in the absolute magnitude, S_{max} , as the main free parameter. We vary this free parameter within $S_{\text{max}} \in [-30 \text{ mag}, 30 \text{ mag}]$. The nugent-hyper model is a template constructed from observations of SN 1998bw ([Galama et al. 1998](#)). Within our analysis, we find that in our runs combining the GRB top-hat jet afterglow with a SN component, the $\chi^2/\text{d.o.f.}$ are very similar to the pure top-hat jet model (0.551 to 0.548 for *Extended* data and 0.496 to 0.503 for *GRANDMA* data). Due to the size of the parameter space, the log Bayes Factor prefers the simpler top-hat jet model, 0.542 ± 0.140 for the *Extended* data and 0.540 ± 0.136 for the *GRANDMA* data). Hence, there is no strong evidence for or against the presence of a SN contribution consistent with the nugent-hyper model combined with models used in our analysis (see, for instance, [Fulton et al. \(2023\)](#) for another interpretation.

3.4.2. Refining the physics in the top-hat jet model

The poor quality of the fits obtained in §3.4.1 is a clear indication of tension between the observed temporal and spectral slopes, as suggested by other authors, e.g. [Laskar et al. \(2023\)](#); [Sato et al. \(2023\)](#); [O’Connor](#)

[et al. \(2023\)](#). We also note that some of the parameters obtained and presented in Figs. 13 and 8 are at odds with typical GRB afterglow parameters. Perhaps the most striking is the very large jet opening angle. It is constrained to $\theta_{\text{core}} \gtrsim 15$ degrees, while typical jets have opening angles $\theta_{\text{core}} \simeq (2.5 \pm 1.0)$ degree ([Wang et al. 2018](#)).

The **afterglowpy** model, which is used by **NMMA**, despite being already a refined implementation of the external shock afterglow model ([Ryan et al. 2020](#)), suffers from some limitations. The dynamics of the jet deceleration is assumed to be in the self-similar regime at all times, which can lead to flux over-estimates at very early times when the jet still is in the coasting phase. We also note that Synchrotron Self-Compton (SSC) scattering is not accounted for; this could be important in the case of GRB 221009A, where some very high energy photons observed may hint towards strong SSC emission.

To further validate the previous analysis, we therefore also model the afterglow data of GRB 221009A using the afterglow model from [Pellouin & Daigne \(2023\)](#) which not only includes synchrotron radiation but also computes the Synchrotron Self-Compton (SSC) radiation, taking into account both the Thomson and Klein-Nishina regime with a treatment following [Nakar et al. \(2009\)](#). This model also accounts for the jet lateral structure, any viewing angle, and also includes the treatment of the coasting phase of the jet propagation, which can induce differences at early times. A detailed description of this afterglow model will be provided in [Pellouin & Daigne \(2023\)](#). However, an analysis with the best-fit parameters shows it does not impact the light curves post the first observed time at 3618s by *Swift*-XRT in this case.

We used a Markov Chain Monte Carlo (MCMC) routine to infer the physical parameters for the afterglow, using the data set presented at the beginning of §3.4. When performing the χ^2 computation, we inflate the errors to avoid any over-fitting of points with artificially small errors, using $\max\{\text{flux error}; 0.3 \times \text{flux}\}$. We initialize 100 independent chains, and run them over 20000 iterations; we remove chains that get stuck in a high χ^2 region of the parameter space, as they are not true solutions.

Our first analysis uses a simplified model where only synchrotron radiation powers the afterglow emission, for comparison with the analysis presented in §3.4.1. For the top-hat jet with a fixed viewing angle $\theta_{\text{obs}} = 0$ degree, the posterior samples converge towards parameter values that are very similar to those presented in §3.4.1, both when fitting the *GRANDMA* data and the extended data. Those values are listed in Table 4, and the

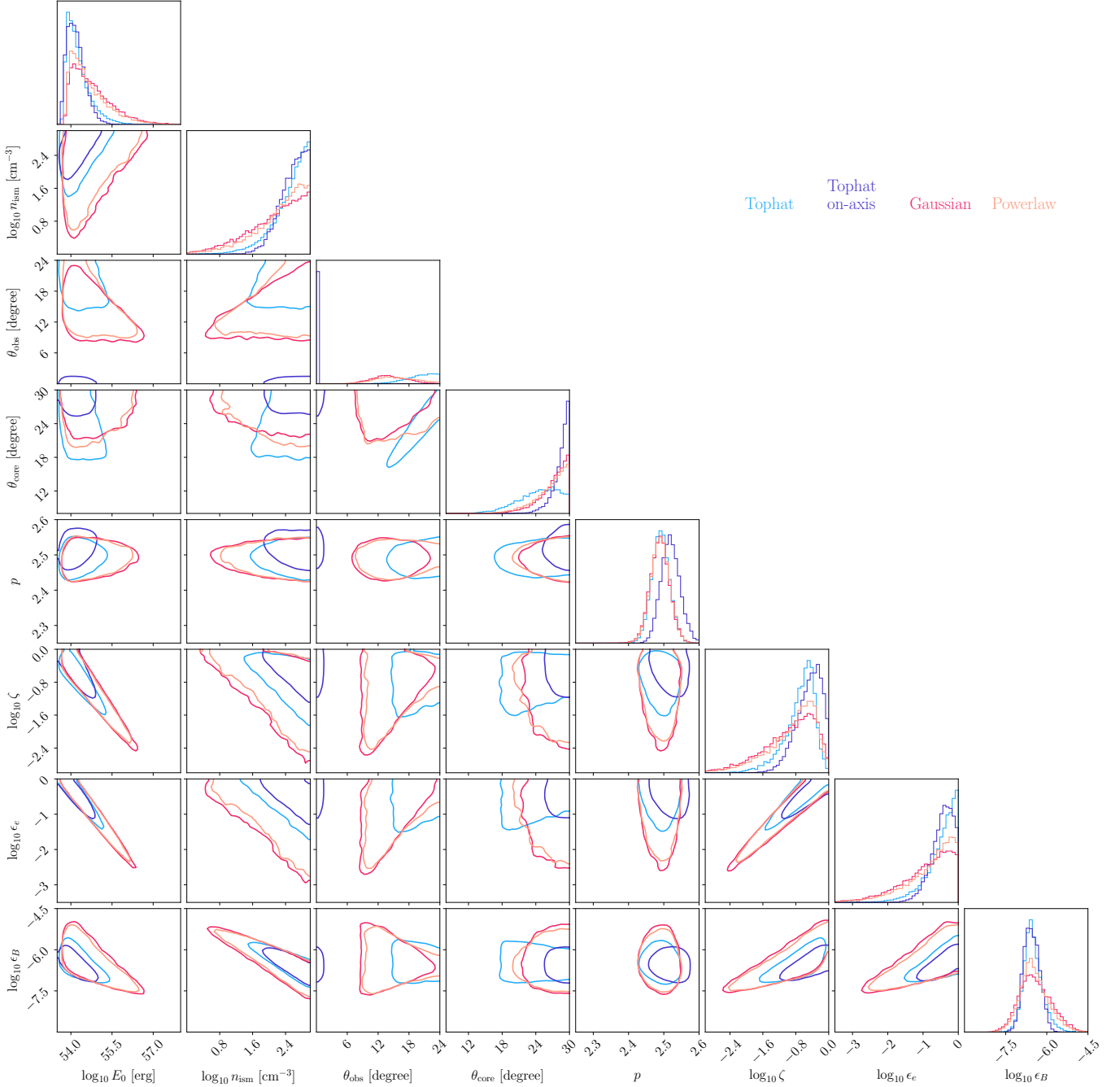


Figure 8. NMMA - Posterior distribution (shown are 90% confidence intervals) for our selected data sets when using different jet models of `afterglowpy` analyzing the *GRANDMA* data.

results are presented in Fig. 10. Our analysis with this independent model confirms the relatively poor quality of the best fit. However, when fitting the extended data set, another solution emerges in the MCMC posteriors with this model; this fit has a lower χ^2 , but still leads to a best fit of poor quality. Contrary to NMMA using `afterglowpy`, the model does not include the lateral expansion of the jet at late times, which leads to an alternative scenario with an early jet break with a shallow

post-jet break decay slope. This solution implies a small core jet opening angle $\theta_{\text{core}} \lesssim 0.7$ degree and an electron slope very close to 2. Both solutions to the model appear on an equal number of MCMC chains (44 each) and therefore correspond to 2 local minima for the χ^2 distribution, with similar weight. When isolating both solutions, we observe the usual parameter correlations (e.g. $E_{0,\text{iso}}$ and n_{ism} or between ϵ_B , ϵ_e and ζ). For better readability, we show in Fig. 9 only the marginalized

Table 1. NMMA - Parameters and prior bounds employed in our Bayesian inferences. We report median posterior values at 90 % credibility from simulations that were run with different jet structures using SF11 extinction data for analysis (*GRANDMA* and *Extended*), see §3.4.1 and Figs. 12,13.

Parameter	Bounds	Prior	Tophat		Tophat on-axis		Gaussian		Power-law	
			<i>GRANDMA</i>	<i>Extended</i>	<i>GRANDMA</i>	<i>Extended</i>	<i>GRANDMA</i>	<i>Extended</i>	<i>GRANDMA</i>	<i>Extended</i>
Isotropic afterglow energy E_0 [erg]	$[10^{50}, 10^{58}]$	log-uniform	$10^{54.16^{+0.71}_{-0.45}}$	$10^{54.71^{+0.91}_{-0.80}}$	$10^{54.15^{+0.52}_{-0.45}}$	$10^{54.51^{+0.52}_{-0.57}}$	$10^{54.62^{+1.18}_{-0.81}}$	$10^{55.27^{+1.20}_{-1.10}}$	$10^{54.17^{+1.15}_{-0.68}}$	$10^{55.13^{+1.22}_{-1.05}}$
Ambient medium's density $n_{\text{ism}}[\text{cm}^{-3}]$	$[10^{-6}, 10^3]$	log-uniform	$10^{2.61^{+0.39}_{-0.70}}$	$10^{2.60^{+0.40}_{-0.63}}$	$10^{2.61^{+0.39}_{-0.49}}$	$10^{2.51^{+0.49}_{-0.51}}$	$10^{2.27^{+0.73}_{-1.14}}$	$10^{2.48^{+0.52}_{-0.82}}$	$10^{2.39^{+0.61}_{-1.04}}$	$10^{2.51^{+0.49}_{-0.76}}$
Energy fraction in electrons ϵ_e	$[10^{-4}, 1]$	log-uniform	$10^{-0.38^{+0.38}_{-0.70}}$	$10^{-0.96^{+0.66}_{-0.81}}$	$10^{-0.41^{+0.41}_{-0.47}}$	$10^{-0.68^{+0.49}_{-0.51}}$	$10^{-0.85^{+0.78}_{-1.09}}$	$10^{-1.39^{+0.98}_{-1.08}}$	$10^{-0.75^{+0.67}_{-1.07}}$	$10^{-1.27^{+0.93}_{-1.09}}$
Energy fraction in magnetic field ϵ_B	$[10^{-9}, 1]$	log-uniform	$10^{-6.54^{+0.62}_{-0.49}}$	$10^{-6.59^{+0.64}_{-0.56}}$	$10^{-6.56^{+0.49}_{-0.42}}$	$10^{-6.83^{+0.55}_{-0.49}}$	$10^{-6.46^{+1.02}_{-0.86}}$	$10^{-6.71^{+0.84}_{-0.71}}$	$10^{-6.50^{+0.90}_{-0.80}}$	$10^{-6.69^{+0.79}_{-0.70}}$
Electron distribution power-law index p	[2,3]	uniform	$2.49^{+0.04}_{-0.04}$	$2.39^{+0.03}_{-0.03}$	$2.52^{+0.04}_{-0.04}$	$2.53^{+0.03}_{-0.03}$	$2.49^{+0.04}_{-0.05}$	$2.40^{+0.03}_{-0.04}$	$2.49^{+0.04}_{-0.04}$	$2.40^{+0.03}_{-0.03}$
Fraction of accelerated electrons ζ	$[10^{-4}, 1]$	log-uniform	$10^{-0.63^{+0.45}_{-0.67}}$	$10^{-0.39^{+0.39}_{-0.62}}$	$10^{-0.44^{+0.44}_{-0.47}}$	$10^{-0.47^{+0.47}_{-0.52}}$	$10^{-0.85^{+0.78}_{-1.09}}$	$10^{-0.52^{+0.52}_{-0.83}}$	$10^{-0.75^{+0.67}_{-1.07}}$	$10^{-0.47^{+0.67}_{-0.80}}$
Viewing angle θ_{obs} [degrees]	[0,30]	uniform	$21.45^{+4.79}_{-5.56}$	$17.14^{+4.82}_{-4.50}$	0	0	$13.98^{+5.75}_{-5.54}$	$12.32^{+4.87}_{-5.04}$	$15.36^{+7.33}_{-6.31}$	$13.19^{+5.34}_{-5.45}$
Jet core's opening angle θ_{core} [degrees]	[0.1,30]	uniform	$24.91^{+5.09}_{-5.50}$	$23.68^{+6.31}_{-5.42}$	$28.85^{+1.15}_{-2.37}$	$29.58^{+0.42}_{-0.98}$	$27.65^{+2.35}_{-4.17}$	$27.85^{+2.15}_{-4.02}$	$27.29^{+2.71}_{-4.80}$	$27.56^{+2.44}_{-4.00}$
“Wing” truncation angle θ_{wing} [degrees]	[0.1,30]	uniform	–	–	–	–	$16.65^{+6.81}_{-6.83}$	$17.51^{+7.01}_{-7.19}$	$18.33^{+8.99}_{-7.17}$	$18.70^{+7.49}_{-7.54}$
Power-law structure index b	[0.1, 7]	uniform	–	–	–	–	–	$2.42^{+3.62}_{-2.52}$	–	$2.64^{+3.41}_{-2.54}$
Angle ratio $\theta_{\text{obs}}/\theta_{\text{core}}$	[1/300,300]	-	$0.866^{+0.05}_{-0.06}$	$0.725^{+0.04}_{-0.04}$	0	0	$0.515^{+0.212}_{-0.189}$	$0.454^{+0.165}_{-0.192}$	$0.573^{+0.304}_{-0.232}$	$0.491^{+0.180}_{-0.218}$

	<i>Extended</i> data	<i>GRANDMA</i> data
Tophat $\theta_{\text{obs}} \leq 0$ vs $\theta_{\text{obs}} = 0$	71.26 ± 0.14	30.66 ± 0.13
Tophat vs Gaussian	4.29 ± 0.14	3.86 ± 0.14
Tophat vs Power-law	3.53 ± 0.14	3.19 ± 0.14

Table 2. The log Bayes factor between different models. For both the *Extended* data and *GRANDMA* data, the tophat model without on-axis assumption is preferred.

	<i>Extended</i> data	<i>GRANDMA</i> data
Tophat $\theta_{\text{obs}} \leq 0$	0.551	0.496
Tophat $\theta_{\text{obs}} = 0$	0.882	0.972
Gaussian	0.561	0.542
Power-law	0.555	0.520

Table 3. The $\chi^2/\text{d.o.f.}$ of different models for NMMA.

posterior distribution for the 8 free parameters of the model, and split the two classes of models in two colors. In blue, we show marginalized posterior distributions for this new model (with a low θ_{core} and $p \lesssim 2.02$) and in orange, marginalized posterior distributions for the model with a large θ_{core} , similar to what is found in §3.4.1. The median values and the 90 % confidence intervals are reported in Table 4 for the two models.

We investigate these two types of models and show in Fig. 10 light curves obtained with the two posterior samples of parameters. The light curves are computed in 3 optical/UV bands (*i*-band, 755 nm, *r*-band, 622 nm, *u*-band, 389.8 nm) and in the 3 X-ray bands (1 keV and 10 keV, with XRT observations; 5 keV with *HXMT* observations). All the fitted observations are shown in grey.

Using Fig. 10, we see that though both classes of models are able to broadly reproduce the multi-wavelength observations, they both fail to reproduce the observed features accurately. The models with high θ_{core} , also found with NMMA and shown in orange, accurately fit the optical but fail to reproduce the observed X-ray tempo-

ral slope. They also feature a jet break at $t \sim 8$ days, which is not observed in the data. Conversely, the models with low θ_{core} , though slightly favored statistically ($\chi^2 = 600$ for the latter model, $\chi^2 = 950$ for the former with the same d.o.f.), also pose major interpretation challenges. The temporal decay in X-rays is also not in line with X-ray observations, and the very high E_0 values that are found (between 10^{55} and 10^{58} ergs) imply a very low prompt efficiency, given a prompt energy $E_{\gamma, \text{iso}} \sim 10^{55}$ erg (An et al. 2023).

While the true energy in the jet ranges between 10^{51} and 5×10^{53} erg due to the very narrow jet opening angles $\theta_{\text{core}} \lesssim 0.7$ degree, the posterior distribution of the prompt efficiency peaks at 10^{-4} , which seems very low for most prompt emission models, especially considering the bright luminosity of the prompt emission of GRB 221009A. This posterior distribution shows, however, a tail towards larger values, reaching 10^{-1} , which are more physically plausible. the physical relevance of this scenario is also questionable regarding the jet dynamics, as at least a moderate lateral expansion should be expected.

As a final verification, we also computed the predicted light curves at radio frequencies and compared them with observations reported in Laskar et al. (2023) and O’Connor et al. (2023). With both classes of models, our predictions over-estimate the flux compared to the observations. We therefore, conclude that while these parameters do correspond to the best fits of the extended data set using a top-hat jet model with a fixed observing angle $\theta_{\text{obs}} = 0$ degree and assuming only synchrotron radiation, they do not provide satisfactory predictions given other constraints found in the literature, motivating a deeper analysis. When accounting for SSC scattering in the model, we ran the models with narrow θ_{core} . We also tested models with a free observing angle and find similar results to those presented in §3.4.1: this model is preferred, but the typical values found for the

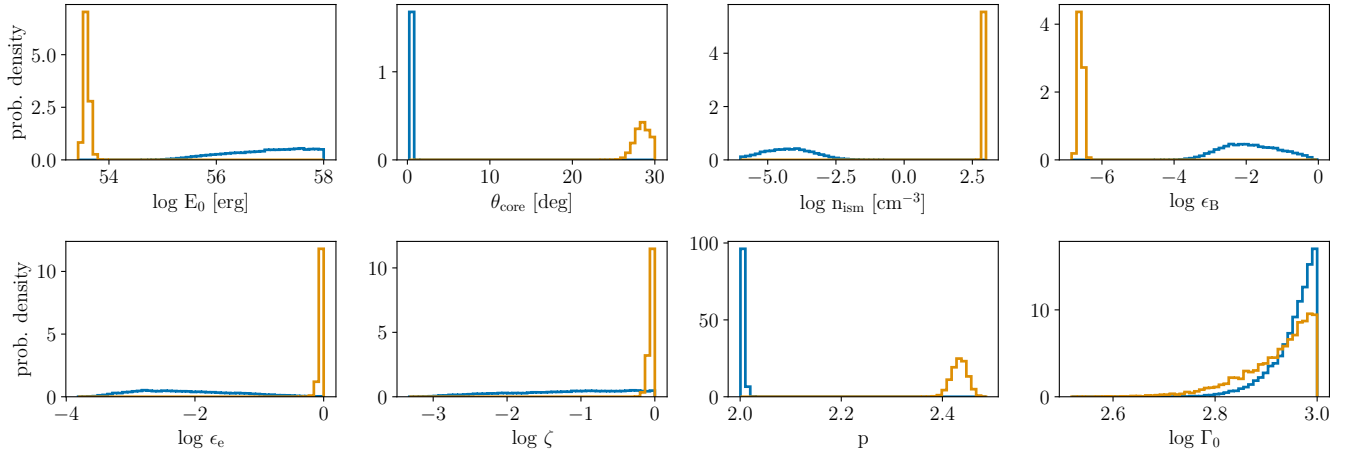


Figure 9. Bayesian inference presented in §3.4.2: Marginalized posterior distribution of the free parameters best fitting the extended data with an on-axis observation of a top-hat jet radiating via synchrotron only, as presented in §3.4.2. In blue, marginalized distributions for the model which features a low θ_{core} and $p \sim 2$, not found with NMMA. In orange, marginalized distributions for the model with a high θ_{core} , similar to what is found with NMMA. The median values and 90 % confidence intervals can be found in Table 4.

Table 4. Bayesian inference presented in §3.4.2: Parameters and prior bounds employed in our Bayesian inferences. We report median posterior values at 90 % credibility from simulations that were run with a top-hat jet structure with a fixed observing angle $\theta_{\text{obs}} = 0$ degrees assuming synchrotron radiation. We fit the extended data set presented in §3.4. These results are discussed in §3.4.2, and in Figs. 9, 10.

Parameter	Symbol	Bounds	Prior	Posterior	
				low θ_{core}	high θ_{core}
Isotropic afterglow energy [erg]	E_0	$[10^{50}, 10^{58}]$	log-uniform	$10^{57.01^{+0.99}_{-1.16}}$	$10^{53.58^{+0.09}_{-0.08}}$
Opening angle of the core of the jet [deg]	θ_{core}	$[0.1, 30]$	uniform	$0.39^{+0.13}_{-0.11}$	$28.47^{+1.52}_{-1.18}$
Density of the ambient medium [cm^{-3}]	n_{ism}	$[10^{-6}, 10^3]$	log-uniform	$10^{-4.23^{+1.36}_{-1.51}}$	$10^{2.98^{+0.02}_{-0.04}}$
Fraction of the energy which generates the magnetic field	ϵ_B	$[10^{-9}, 1]$	log-uniform	$10^{-1.93^{+1.39}_{-1.17}}$	$10^{-6.59^{+0.11}_{-0.10}}$
Fraction of the energy which accelerates the electrons	ϵ_e	$[10^{-4}, 1]$	log-uniform	$10^{-2.22^{+1.33}_{-1.16}}$	$10^{-0.02^{+0.02}_{-0.05}}$
Fraction of electrons accelerated at the shock	ζ	$[10^{-4}, 1]$	log-uniform	$10^{-1.10^{+1.10}_{-1.25}}$	$10^{-0.04^{+0.04}_{-0.06}}$
Electron population Lorentz factor injection index	p	$[2, 3]$	uniform	$2.003^{+0.005}_{-0.003}$	$2.43^{+0.03}_{-0.02}$
Initial Lorentz factor	Γ_0	$[10^1, 10^3]$	log-uniform	$10^{2.96^{+0.04}_{-0.07}}$	$10^{2.94^{+0.06}_{-0.11}}$

parameters are close to those found with the fixed observation angle. Therefore our analysis shows that even in a more realistic description including the coasting phase and the SSC radiation, the standard top-hat jet afterglow model is in tension with the observed data. We note that for free observing angles, the MCMC chains do not favor narrow θ_{core} anymore. Finally, we also study the impact of the jet structure: our findings are similar to those presented in §3.4.1. We also performed our analysis with only the GRANDMA data set and find similar values as those found with NMMA, but in this case the MCMC chains also do not find the very narrow θ_{core} models. We leave to a future study the investigation of

more advanced models regarding, for instance, the jet structure of the external medium density.

4. DISCUSSION AND CONCLUSION

In this work, the properties of the GRB 221009A afterglow are studied using a multi-wavelength data set, presenting data from optical observations from ground-based telescopes or the GRANDMA/KNC network and the Low Energy X-ray telescope (LE) onboard the *Insight-HXMT* satellite. The X-ray observations were made 9.8 hours to 3 days after the trigger time, while the ultraviolet, optical, and near-infrared sky was covered from the prompt emission (shallow limits from all-sky cameras) and then (with narrow-field instruments) from

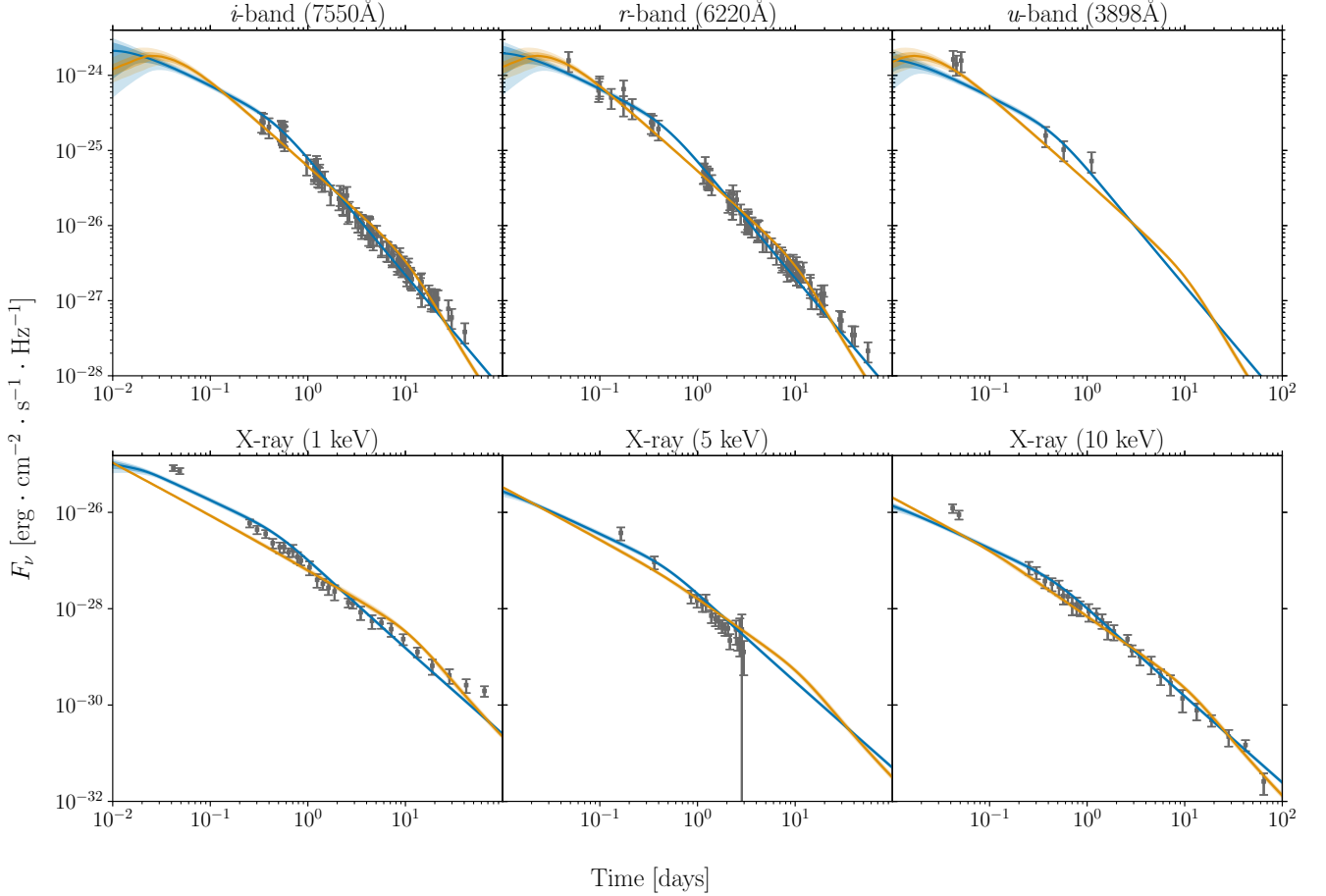


Figure 10. Bayesian inference presented in § 3.4.2

- Predicted light curves for the two classes of parameters reported in Fig. 9 and found using a top-hat model with a fixed observing angle $\theta_{\text{obs}} = 0$ degree, and assuming only synchrotron radiation. Observing frequencies or energies are shown on top of each panel, and the fitted observational data is displayed in grey. Blue curves show the model with a low θ_{core} and $p \sim 2$. Orange curves show the model with a high θ_{core} .

2.2 hours after the trigger time to about 20 days. The GRANDMA network involved more than 30 telescopes, including both professional and amateur telescopes, and collected more than 200 images for this GRB. This is one of the few GRB afterglows that has been observed extensively by amateur astronomers. The measurements with the deepest limiting magnitudes reach $m_{\text{lim}} = 24.6$ mag in g' band by a professional telescope (CFHT) and $m_{\text{lim}} = 21.5$ mag in the V band by an amateur telescope, demonstrating the potential for citizen contributions to time-domain astrophysical science. We also collected prompt observations of the GRB in the optical (between T_0 and to $T_0 + 500$ seconds) by cameras managed by the Desert Fireball Network, but no optical flash was detected in the V band (down to a limiting magnitude of 3.8 mag). We furthermore collect public data from the XRT telescope onboard the *Swift* satellite, with the first observation having been taken about one hour

after the GRB trigger time. Two specially-tuned photometric pipelines, STDPIPE and MUPHOTEN, are used to analyze the GRB afterglow data. The observations are calibrated using stars from the PS1 catalog; slightly different results being obtained for Johnson-Cousins filters between the two pipelines. For this reason, only a subset of data with good quality and consistent results have been selected for analysis.

In this paper, we tackle the challenge of determining the significant extinction correction, as the GRB lies behind the Galactic plane. To correct for this, we employ two different techniques: firstly, we use the SF11 maps (Schlafly & Finkbeiner 2011), which may overestimate the extinction. Secondly, we use the RF09 maps by Rowles & Froebrich (2009), which utilize near-infrared color excess determinations based on 2MASS observations. This method results in a significantly lower extinction value (but is only valid out to 2 – 3

kpc), compared to the SF11 value. Taking into account the existence of dust at larger distances determined by X-ray measurements of dust rings (Negro et al. 2023; Vasilopoulos et al. 2023; Williams et al. 2023), we proceed to discuss the reliability of these measurements and conduct our follow-up analysis using both correction methods for comparison.

Empirical analysis of the light curve shows it to be composed of three power-law sections (steep, shallow, steep), with the first section only covered by a short data baseline. The data after ~ 0.1 d show a clear break and a relatively shallow post-break slope with no further indication of a jet break, which would usually lead to a decay slope $\alpha \gtrsim 2$. The light curve analysis yields a SED which we fit with three solutions for the foreground/host-galaxy extinction including one under the assumption that the entire extinction is foreground. All extinction models yield viable solutions; in combination with spectroscopic evidence for small-to-moderate host-galaxy extinction, we prefer the combination of SF11 foreground correction and about half a magnitude of SMC-type host-galaxy extinction. Using these values, we are able to compare the optical afterglow to a global sample and find it to be luminous but not excessively so, in contrast to the extreme isotropic energy release of the prompt emission, a result also found for the X-ray afterglow (Williams et al. 2023).

We analysed our observations in the framework of the standard GRB afterglow model; in this model, the observed flux is dominated by synchrotron radiation from shock-accelerated electrons at the forward external shock due to the deceleration of the GRB relativistic jet by the ambient medium (Sari et al. 1998). We limited our study to the case of a uniform medium. We performed Bayesian Inference using two multi-wavelength datasets, the first composed of our own GRANDMA data, complemented by X-ray data (*Swift*-XRT and *HXMT*-LE), and the second one extended with additional optical and near-infrared measurements collected from the literature: see §3.4. This Bayesian Inference was done using the Nuclear physics and Multi-Messenger Astronomy framework, *NMMA* (Dietrich et al. 2020; Pang et al. 2022), employing the semi-analytic code *afterglowpy* for afterglow lightcurve modelling (Ryan et al. 2020) and was complemented with an independent Bayesian inference based on the model by Pellouin & Daigne (2023) to test the impact of more realistic physics for the jet dynamics; this model accounts for both the early coasting phase and for the emission, by including the synchrotron self-Compton emission with a full treatment in Thomson and Klein-Nishina regimes. We started with the simplest version

of the standard GRB afterglow model, i.e. a top-hat jet seen exactly on-axis. Both independent pipelines converged to similar solutions, with a best fit that yields poor fits to some of the observations. This analysis confirms a tension between the standard afterglow model and the observed spectral and temporal evolution, as suggested by Laskar et al. (2023), based on the closure relations. The smoother transitions, rather than sharp breaks, observed in such a detailed model only moderately improve the predicted lightcurves. In particular, the high frequency lightcurves, especially in X-rays, are not well reproduced, and the late-time radio flux is overpredicted. In addition, we note that this best-fit yields an unexpectedly large opening angle for such a bright GRB, and a very dense external medium. We explored several additional effects: free viewing angle, lateral structure of the jet (power-law or Gaussian), early coasting phase, SSC radiation, or an underlying supernova component. None of these models which include more realistic physics leads to better fits. We, therefore, conclude that the modelling of the GRB 221009A afterglow will require going beyond the most standard afterglow model by, for instance, considering more complex jet structure, or external density, or the contribution of the reverse shock, as also suggested by Laskar et al. (2023); O’Connor et al. (2023).

GRB 221009A is an absolutely unique event, representing not just the nearest extremely energetic GRB, but potentially also the most energetic GRB ever detected. These two factors combined make it by far the brightest GRB ever seen, at the very least a once-in-a-lifetime event, more probably even a millennial one. To have such an event occur when we have a fleet of satellites in space able to detect gamma-rays, and the ground- and space-based capabilities to determine the distance and follow up the afterglow evolution in detail, even by amateur astronomers, is fortuitous indeed. It is unlikely that a chance like this will come again in the coming decades or even centuries, making this an event to be remembered through the ages.

The GRANDMA consortium thanks the amateur participants of the Kilonova-Catcher program and observers from GRANDMA. GRANDMA thanks the paper writing team managed by D. A. Kann. The Kilonova-Catcher program is supported by the IdEx Université de Paris Cité, ANR-18-IDEX-0001. The GRANDMA collaboration thanks G. Parent, E. Maris, F. Bayard, O. Aguerre and M. Richmond for their observations. This project has received financial support from the CNRS through the MITI interdisciplinary programs. We thank Mathias Schultheis for fruitful discussions regarding extinction selection. D. A. Kann acknowledges the support by the State of Hessen within the Research Cluster ELEMENTS (Project ID 500/10.006). S. Antier acknowledges the financial support of the Programme National Hautes Energies (PNHE) and of Crédits Scientifiques Incitatifs d’UCA 2023. M. W. Coughlin acknowledges support from the National Science Foundation with grant numbers PHY-2010970 and OAC-2117997. C. Andrade and M. W. Coughlin were supported by the Preparing for Astrophysics with LSST Program, funded by the Heising Simons Foundation through grant 2021-2975, and administered by Las Cumbres Observatory. J.-G. Ducoin is supported by a research grant from the Ile-de-France Region within the framework of the Domaine d’Intérêt Majeur-Astrophysique et Conditions d’Apparition de la Vie (DIM-ACAV). This work has made use of the Infinity Cluster hosted by Institut d’Astrophysique de Paris. C. Pellouin acknowledges funding support from the Initiative Physique des Infinis (IPI), a research training program of the IdEX SUPER at Sorbonne Université. The Egyptian team acknowledges support from the Science, Technology & Innovation Funding Authority (STDF) under grant number 45779. S. Karpov is supported by European Structural and Investment Fund and the Czech Ministry of Education, Youth and Sports (Project CoGraDS – CZ.02.1.01/0.0/0.0/15_003/0000437). J. Mao is supported by the NSFC 11673062 and Oversea Talent Program of Yunnan Province. The *Insight-HXMT* team acknowledges support from the National Key R&D Program of China (2021YFA0718500) and the National Natural Science Foundation of China under Grants Nos. U1838201, U1838202.

REFERENCES

- Abbott, B. P., Abbott, R., Abbott, T. D., et al. 2017a, *PhRvL*, 119, 161101, doi: [10.1103/PhysRevLett.119.161101](https://doi.org/10.1103/PhysRevLett.119.161101)
- . 2017b, *ApJL*, 848, L12, doi: [10.3847/2041-8213/aa91c9](https://doi.org/10.3847/2041-8213/aa91c9)
- . 2017c, *ApJL*, 848, L13, doi: [10.3847/2041-8213/aa920c](https://doi.org/10.3847/2041-8213/aa920c)

- Ackermann, M., Ajello, M., Asano, K., et al. 2014, *Science*, 343, 42, doi: [10.1126/science.1242353](https://doi.org/10.1126/science.1242353)
- Aguerre, O., Bayard, F., Broens, E., et al. 2022, GRB Coordinates Network, 32934
- Agüí Fernández, J. F., Thöne, C. C., Kann, D. A., et al. 2023, *MNRAS*, 520, 613, doi: [10.1093/mnras/stad099](https://doi.org/10.1093/mnras/stad099)
- Ahumada, T., Singer, L. P., Anand, S., et al. 2021, *Nature Astronomy*, 5, 917, doi: [10.1038/s41550-021-01428-7](https://doi.org/10.1038/s41550-021-01428-7)
- Ai, S., & Gao, H. 2022, arXiv e-prints, arXiv:2210.14116, doi: [10.48550/arXiv.2210.14116](https://doi.org/10.48550/arXiv.2210.14116)
- Aivazyan, V., Almualla, M., Antier, S., et al. 2022, *MNRAS*, 515, 6007, doi: [10.1093/mnras/stac2054](https://doi.org/10.1093/mnras/stac2054)
- Akerlof, C., Balsano, R., Barthelmy, S., et al. 1999, *Nature*, 398, 400, doi: [10.1038/18837](https://doi.org/10.1038/18837)
- Almeida, A., Anderson, S. F., Argudo-Fernández, M., et al. 2023, arXiv e-prints, arXiv:2301.07688, doi: [10.48550/arXiv.2301.07688](https://doi.org/10.48550/arXiv.2301.07688)
- An, Z.-H., Antier, S., Bi, X.-Z., et al. 2023, arXiv e-prints, arXiv:2303.01203, doi: [10.48550/arXiv.2303.01203](https://doi.org/10.48550/arXiv.2303.01203)
- Antier, S., Agayeva, S., Aivazyan, V., et al. 2020a, *MNRAS*, 492, 3904, doi: [10.1093/mnras/stz3142](https://doi.org/10.1093/mnras/stz3142)
- Antier, S., Agayeva, S., Almualla, M., et al. 2020b, *MNRAS*, 497, 5518, doi: [10.1093/mnras/staa1846](https://doi.org/10.1093/mnras/staa1846)
- Atri, P., An, T., Giroletti, M., et al. 2022, GRB Coordinates Network, 32907
- Atteia, J. L. 2022, GRB Coordinates Network, 32793
- Atteia, J. L., Heussaff, V., Dezalay, J. P., et al. 2017, *ApJ*, 837, 119, doi: [10.3847/1538-4357/aa5ffa](https://doi.org/10.3847/1538-4357/aa5ffa)
- Atwood, W. B., Abdo, A. A., Ackermann, M., et al. 2009, *ApJ*, 697, 1071, doi: [10.1088/0004-637X/697/2/1071](https://doi.org/10.1088/0004-637X/697/2/1071)
- Barthelmy, S. D., Barbier, L. M., Cummings, J. R., et al. 2005, *SSRv*, 120, 143, doi: [10.1007/s11214-005-5096-3](https://doi.org/10.1007/s11214-005-5096-3)
- Becker, A. 2015, HOTPANTS: High Order Transform of PSF ANd Template Subtraction. <http://ascl.net/1504.004>
- Belkin, S., Kim, V., Pozanenko, A., et al. 2022a, GRB Coordinates Network, 32769
- Belkin, S., Moskvitin, A., Kim, V., et al. 2022b, GRB Coordinates Network, 32818
- Belkin, S., Pozanenko, A., Klunko, E., Pankov, N., & GRB IKI FuN. 2022c, GRB Coordinates Network, 32645
- Berger, E. 2014, *ARA&A*, 52, 43, doi: [10.1146/annurev-astro-081913-035926](https://doi.org/10.1146/annurev-astro-081913-035926)
- Bertin, E. 2010, SWarp: Resampling and Co-adding FITS Images Together, Astrophysics Source Code Library, record ascl:1010.068. <http://ascl.net/1010.068>
- Bertin, E. 2011, in *Astronomical Society of the Pacific Conference Series*, Vol. 442, *Astronomical Data Analysis Software and Systems XX*, ed. I. N. Evans, A. Accomazzi, D. J. Mink, & A. H. Rots, 435
- Bertin, E., & Arnouts, S. 1996, *A&AS*, 117, 393, doi: [10.1051/aas:1996164](https://doi.org/10.1051/aas:1996164)
- Bikmaev, I., Khamitov, I., Irtuganov, E., et al. 2022a, GRB Coordinates Network, 32743
- . 2022b, GRB Coordinates Network, 32752
- Bissaldi, E., Omodei, N., Kerr, M., & Fermi-LAT Team. 2022, GRB Coordinates Network, 32637
- Bloom, J. S., Perley, D. A., Li, W., et al. 2009, *ApJ*, 691, 723, doi: [10.1088/0004-637X/691/1/723](https://doi.org/10.1088/0004-637X/691/1/723)
- Boch, T., Fernique, P., Bonnarel, F., et al. 2020, in *Astronomical Society of the Pacific Conference Series*, Vol. 527, *Astronomical Society of the Pacific Conference Series*, ed. R. Pizzo, E. R. Deul, J. D. Mol, J. de Plaa, & H. Verkouter, 121
- Boch, T., Pineau, F., & Derriere, S. 2012, in *Astronomical Society of the Pacific Conference Series*, Vol. 461, *Astronomical Data Analysis Software and Systems XXI*, ed. P. Ballester, D. Egret, & N. P. F. Lorente, 291
- Boër, M., Atteia, J. L., Damerdji, Y., et al. 2006, *ApJL*, 638, L71, doi: [10.1086/501048](https://doi.org/10.1086/501048)
- Bradley, L., Sipőcz, B., Robitaille, T., et al. 2021, *astropy/photutils: 1.1.0*, 1.1.0, Zenodo, doi: [10.5281/zenodo.4624996](https://doi.org/10.5281/zenodo.4624996)
- Brivio, R., Ferro, M., D’Avanzo, P., et al. 2022, GRB Coordinates Network, 32652
- Broens, E. 2022, GRB Coordinates Network, 32640
- Buchner, J. 2016, PyMultiNest: Python interface for MultiNest, Astrophysics Source Code Library, record ascl:1606.005. <http://ascl.net/1606.005>
- Burns, E., Svinkin, D., Femimore, E., et al. 2023, arXiv e-prints, arXiv:2302.14037, doi: [10.48550/arXiv.2302.14037](https://doi.org/10.48550/arXiv.2302.14037)
- Burrows, D. N., Hill, J. E., Nousek, J. A., et al. 2005, *SSRv*, 120, 165, doi: [10.1007/s11214-005-5097-2](https://doi.org/10.1007/s11214-005-5097-2)
- Cano, Z., Wang, S.-Q., Dai, Z.-G., & Wu, X.-F. 2017, *Advances in Astronomy*, 2017, 8929054, doi: [10.1155/2017/8929054](https://doi.org/10.1155/2017/8929054)
- Cardelli, J. A., Clayton, G. C., & Mathis, J. S. 1989, *ApJ*, 345, 245, doi: [10.1086/167900](https://doi.org/10.1086/167900)
- Castro-Tirado, A. J., Sanchez-Ramirez, R., Hu, Y. D., et al. 2022, GRB Coordinates Network, 32686
- Chambers, K. C., Magnier, E. A., Metcalfe, N., et al. 2016, arXiv e-prints, arXiv:1612.05560. <https://arxiv.org/abs/1612.05560>
- Chen, T. W., Malesani, D. B., Yang, S., et al. 2022, GRB Coordinates Network, 32667
- D’Avanzo, P., Ferro, M., Brivio, R., et al. 2022, GRB Coordinates Network, 32755
- De Pasquale, M., Page, M. J., Kann, D. A., et al. 2016, *MNRAS*, 462, 1111, doi: [10.1093/mnras/stw1704](https://doi.org/10.1093/mnras/stw1704)

- de Ugarte Postigo, A., Izzo, L., Pugliese, G., et al. 2022, GRB Coordinates Network, 32648
- de Wet. 2022, GRB Coordinates Network, 32944
- de Wet, S., Groot, P. J., & Meerlicht Consortium. 2022, GRB Coordinates Network, 32646
- Dichiara, S., Gropp, J. D., Kennea, J. A., et al. 2022a, The Astronomer’s Telegram, 15650
- . 2022b, GRB Coordinates Network, 32632
- Dietrich, T., Coughlin, M. W., Pang, P. T. H., et al. 2020, *Science*, 370, 1450, doi: [10.1126/science.abb4317](https://doi.org/10.1126/science.abb4317)
- Duan, K.-K., Xu, Z.-L., Shen, Z.-Q., et al. 2022, GRB Coordinates Network, 32973
- Durbak, J. M., Kutuyev, A. S., Andreoni, I., et al. 2022, GRB Coordinates Network, 32654
- Duverne, P. A., Antier, S., Basa, S., et al. 2022, *PASP*, 134, 114504, doi: [10.1088/1538-3873/ac9c31](https://doi.org/10.1088/1538-3873/ac9c31)
- Dzhappuev, D. D., Afshokov, Y. Z., Dzaparova, I. M., et al. 2022, The Astronomer’s Telegram, 15669
- Evans, P. A., Beardmore, A. P., Page, K. L., et al. 2007, *A&A*, 469, 379, doi: [10.1051/0004-6361:20077530](https://doi.org/10.1051/0004-6361:20077530)
- . 2009, *MNRAS*, 397, 1177, doi: [10.1111/j.1365-2966.2009.14913.x](https://doi.org/10.1111/j.1365-2966.2009.14913.x)
- Evans, P. A., Willingale, R., Osborne, J. P., et al. 2010, *A&A*, 519, A102, doi: [10.1051/0004-6361/201014819](https://doi.org/10.1051/0004-6361/201014819)
- Ferro, M., Brivio, R., D’Avanzo, P., et al. 2022, GRB Coordinates Network, 32804
- Frederiks, D., Lysenko, A., Ridnaia, A., et al. 2022, GRB Coordinates Network, 32668
- Frederiks, D., Svinkin, D., Lysenko, A. L., et al. 2023, arXiv e-prints, arXiv:2302.13383, doi: [10.48550/arXiv.2302.13383](https://doi.org/10.48550/arXiv.2302.13383)
- Froebrich, D., Ray, T. P., Murphy, G. C., & Scholz, A. 2005, *A&A*, 432, L67, doi: [10.1051/0004-6361:200500016](https://doi.org/10.1051/0004-6361:200500016)
- Fulton, M. D., Smartt, S. J., Rhodes, L., et al. 2023, arXiv e-prints, arXiv:2301.11170, doi: [10.48550/arXiv.2301.11170](https://doi.org/10.48550/arXiv.2301.11170)
- Galama, T. J., Vreeswijk, P. M., van Paradijs, J., et al. 1998, *Nature*, 395, 670, doi: [10.1038/27150](https://doi.org/10.1038/27150)
- Ge, M. Y., Chen, Y. P., Liao, J. Y., et al. 2022, The Astronomer’s Telegram, 15703
- Gehrels, N., Ramirez-Ruiz, E., & Fox, D. B. 2009, *ARA&A*, 47, 567, doi: [10.1146/annurev.astro.46.060407.145147](https://doi.org/10.1146/annurev.astro.46.060407.145147)
- Gehrels, N., Chincarini, G., Giommi, P., et al. 2004, *ApJ*, 611, 1005, doi: [10.1086/422091](https://doi.org/10.1086/422091)
- Gehrels, N., Barthelmy, S. D., Burrows, D. N., et al. 2008, *ApJ*, 689, 1161, doi: [10.1086/592766](https://doi.org/10.1086/592766)
- Gendre, B., Stratta, G., Atteia, J. L., et al. 2013, *ApJ*, 766, 30, doi: [10.1088/0004-637X/766/1/30](https://doi.org/10.1088/0004-637X/766/1/30)
- GLAST Facility Science Team, Gehrels, N., & Michelson, P. 1999, *Astroparticle Physics*, 11, 277, doi: [10.1016/S0927-6505\(99\)00066-3](https://doi.org/10.1016/S0927-6505(99)00066-3)
- Goldstein, A., Veres, P., Burns, E., et al. 2017, *ApJL*, 848, L14, doi: [10.3847/2041-8213/aa8f41](https://doi.org/10.3847/2041-8213/aa8f41)
- Gotz, D., Mereghetti, S., Savchenko, V., et al. 2022, GRB Coordinates Network, 32660
- Greiner, J., Kloise, S., Reinsch, K., et al. 2003, *Nature*, 426, 157, doi: [10.1038/nature02077](https://doi.org/10.1038/nature02077)
- Groot, P. J., Vreeswijk, P. M., Ter Horst, R., et al. 2022, GRB Coordinates Network, 32678
- Guha, A., & Nicholson, P. 2022, GRB Coordinates Network, 32745
- Gupta, R., Ror, A. K., Pandey, S. B., et al. 2022, GRB Coordinates Network, 32811
- Hayes, L. A., & Gallagher, P. T. 2022, *Research Notes of the American Astronomical Society*, 6, 222, doi: [10.3847/2515-5172/ac9d2f10.48550/arXiv.2210.15284](https://doi.org/10.3847/2515-5172/ac9d2f10.48550/arXiv.2210.15284)
- Hjorth, J., & Bloom, J. S. 2012, in Chapter 9 in “Gamma-Ray Bursts” (Cambridge University Press), 169–190
- Hjorth, J., Sollerman, J., Møller, P., et al. 2003, *Nature*, 423, 847, doi: [10.1038/nature01750](https://doi.org/10.1038/nature01750)
- Hou, L. G., & Han, J. L. 2014, *A&A*, 569, A125, doi: [10.1051/0004-6361/20142403910.48550/arXiv.1407.7331](https://doi.org/10.1051/0004-6361/20142403910.48550/arXiv.1407.7331)
- Hu, Y. D., Casanova, V., Fernandez-Garcia, E., et al. 2022, GRB Coordinates Network, 32644
- Huang, Y., Hu, S., Chen, S., et al. 2022, GRB Coordinates Network, 32677
- Huber, M., Schultz, A., Chambers, K. C., et al. 2022, GRB Coordinates Network, 32758
- IceCube Collaboration. 2022, GRB Coordinates Network, 32665
- Iwakiri, W., Jaisawal, G. K., Younes, G., et al. 2022, GRB Coordinates Network, 32694
- Izzo, L., Saccardi, A., Fynbo, J. P. U., et al. 2022, GRB Coordinates Network, 32765
- Jin, Z.-P., Zhou, H., Wang, Y., et al. 2023, arXiv e-prints, arXiv:2301.02407. <https://arxiv.org/abs/2301.02407>
- Kann, D. A., & Agui Fernandez, J. F. 2022, GRB Coordinates Network, 32762
- Kann, D. A., Kloise, S., & Zeh, A. 2006, *ApJ*, 641, 993, doi: [10.1086/500652](https://doi.org/10.1086/500652)
- Kann, D. A., Masetti, N., & Kloise, S. 2007, *AJ*, 133, 1187, doi: [10.1086/511066](https://doi.org/10.1086/511066)
- Kann, D. A., Kloise, S., Zhang, B., et al. 2010, *ApJ*, 720, 1513, doi: [10.1088/0004-637X/720/2/1513](https://doi.org/10.1088/0004-637X/720/2/1513)
- . 2011, *ApJ*, 734, 96, doi: [10.1088/0004-637X/734/2/96](https://doi.org/10.1088/0004-637X/734/2/96)
- Karpov, S. 2021, STDPipe: Simple Transient Detection Pipeline. <http://ascl.net/2112.006>

- Kennea, J. A., Williams, M., & Swift Team. 2022a, GRB Coordinates Network, 32635
- Kennea, J. A., Tohuvavohu, A., Osborne, J. P., et al. 2022b, GRB Coordinates Network, 32651
- Kim, V., Krugov, M., Pozanenko, A., et al. 2022, GRB Coordinates Network, 32670
- KM3NeT Collaboration. 2022, GRB Coordinates Network, 32741
- Kobayashi, K., Negoro, H., Nakajima, M., et al. 2022, GRB Coordinates Network, 32756
- Kobayashi, S. 2000, ApJ, 545, 807, doi: [10.1086/317869](https://doi.org/10.1086/317869)
- Kostov, A., & Bonev, T. 2018, Bulgarian Astronomical Journal, 28, 3, doi: [10.48550/arXiv.1706.06147](https://doi.org/10.48550/arXiv.1706.06147)
- Kouveliotou, C., Meegan, C. A., Fishman, G. J., et al. 1993, ApJL, 413, L101, doi: [10.1086/186969](https://doi.org/10.1086/186969)
- Kulkarni, S. R., Djorgovski, S. G., Odewahn, S. C., et al. 1999, Nature, 398, 389, doi: [10.1038/18821](https://doi.org/10.1038/18821)
- Kumar, H., Swain, V., Waratkar, G., et al. 2022, GRB Coordinates Network, 32662
- Kunert, N., Antier, S., Nedora, V., et al. 2023, arXiv e-prints, arXiv:2301.02049, doi: [10.48550/arXiv.2301.02049](https://doi.org/10.48550/arXiv.2301.02049)
- Lapshov, I., Molkov, S., Mereminsky, I., et al. 2022, GRB Coordinates Network, 32663
- Laskar, T., Alexander, K. D., Margutti, R., et al. 2023, arXiv e-prints, arXiv:2302.04388, <https://arxiv.org/abs/2302.04388>
- Lesage, S., Veres, P., Roberts, O. J., et al. 2022, GRB Coordinates Network, 32642
- Levan, A., Nugent, P., Fruchter, A., et al. 2005, ApJ, 624, 880, doi: [10.1086/428657](https://doi.org/10.1086/428657)
- Levan, A. J., Tanvir, N. R., Starling, R. L. C., et al. 2014a, ApJ, 781, 13, doi: [10.1088/0004-637X/781/1/13](https://doi.org/10.1088/0004-637X/781/1/13)
- Levan, A. J., Tanvir, N. R., Fruchter, A. S., et al. 2014b, ApJ, 792, 115, doi: [10.1088/0004-637X/792/2/115](https://doi.org/10.1088/0004-637X/792/2/115)
- Levan, A. J., Lamb, G. P., Schneider, B., et al. 2023, arXiv e-prints, arXiv:2302.07761, doi: [10.48550/arXiv.2302.07761](https://doi.org/10.48550/arXiv.2302.07761)
- Lipkin, Y. M., Ofek, E. O., Gal-Yam, A., et al. 2004, ApJ, 606, 381, doi: [10.1086/383000](https://doi.org/10.1086/383000)
- Liu, J. C., Zhang, Y. Q., Xiong, S. L., et al. 2022, GRB Coordinates Network, 32751
- Malesani, D. B., Levan, A. J., Izzo, L., et al. 2023, arXiv e-prints, arXiv:2302.07891, doi: [10.48550/arXiv.2302.07891](https://doi.org/10.48550/arXiv.2302.07891)
- Mao, J., Lu, K. X., Zhao, X. H., & Bai, J. M. 2022, GRB Coordinates Network, 32727
- Maselli, A., Melandri, A., Nava, L., et al. 2014, Science, 343, 48, doi: [10.1126/science.1242279](https://doi.org/10.1126/science.1242279)
- Matheson, T., Garnavich, P. M., Stanek, K. Z., et al. 2003, ApJ, 599, 394, doi: [10.1086/379228](https://doi.org/10.1086/379228)
- Mazets, E. P., Golenetskii, S. V., Ilinskii, V. N., et al. 1981, Ap&SS, 80, 3, doi: [10.1007/BF00649140](https://doi.org/10.1007/BF00649140)
- Meegan, C., Lichti, G., Bhat, P. N., et al. 2009, ApJ, 702, 791, doi: [10.1088/0004-637X/702/1/791](https://doi.org/10.1088/0004-637X/702/1/791)
- Melandri, A., Pian, E., D’Elia, V., et al. 2014, A&A, 567, A29, doi: [10.1051/0004-6361/201423572](https://doi.org/10.1051/0004-6361/201423572)
- Minaev, P. Y., & Pozanenko, A. S. 2020, MNRAS, 492, 1919, doi: [10.1093/mnras/stz3611](https://doi.org/10.1093/mnras/stz3611)
- Mitchell, L. J., Philips, B. F., & Johnson, W. N. 2022, GRB Coordinates Network, 32746
- Mösta, P., Ott, C. D., Radice, D., et al. 2015, Nature, 528, 376, doi: [10.1038/nature15755](https://doi.org/10.1038/nature15755)
- Nakar, E. 2007, PhR, 442, 166, doi: [10.1016/j.physrep.2007.02.005](https://doi.org/10.1016/j.physrep.2007.02.005)
- Nakar, E., Ando, S., & Sari, R. 2009, ApJ, 703, 675, doi: [10.1088/0004-637X/703/1/675](https://doi.org/10.1088/0004-637X/703/1/675)
- Neckel, T., & Klare, G. 1980, A&AS, 42, 251
- Negoro, H., Nakajima, M., Kobayashi, K., et al. 2022, The Astronomer’s Telegram, 15651
- Negro, M., Di Lalla, N., Omodei, N., et al. 2023, arXiv e-prints, arXiv:2301.01798, <https://arxiv.org/abs/2301.01798>
- Nysewander, M., Fruchter, A. S., & Pe’er, A. 2009, ApJ, 701, 824, doi: [10.1088/0004-637X/701/1/824](https://doi.org/10.1088/0004-637X/701/1/824)
- O’Connor, B., Cenko, S. B., Troja, E., et al. 2022a, GRB Coordinates Network, 32739
- . 2022b, GRB Coordinates Network, 32799
- O’Connor, B., Troja, E., Ryan, G., et al. 2023, arXiv e-prints, arXiv:2302.07906, doi: [10.48550/arXiv.2302.07906](https://doi.org/10.48550/arXiv.2302.07906)
- Odeh, M. 2022, GRB Coordinates Network, 32649
- Omodei, N., Bruel, P., Bregeon, J., et al. 2022a, GRB Coordinates Network, 32760
- . 2022b, GRB Coordinates Network, 32916
- Paek, G. S. H., Im, M., Urata, Y., & Sung, H.-I. 2022, GRB Coordinates Network, 32659
- Pal, S., Hobara, Y., Shvets, A., et al. 2023, Atmosphere, 14, 217, doi: [10.3390/atmos14020217](https://doi.org/10.3390/atmos14020217)
- Pancino, E., Marrese, P. M., Marinoni, S., et al. 2022, A&A, 664, A109, doi: [10.1051/0004-6361/202243939](https://doi.org/10.1051/0004-6361/202243939)
- Pang, P. T. H., Dietrich, T., Coughlin, M. W., et al. 2022, arXiv e-prints, arXiv:2205.08513, doi: [10.48550/arXiv.2205.08513](https://doi.org/10.48550/arXiv.2205.08513)
- Pannarale, F. 2022, GRB Coordinates Network, 32877
- Pei, Y. C. 1992, ApJ, 395, 130, doi: [10.1086/171637](https://doi.org/10.1086/171637)
- Pellouin, C., & Daigne, F. 2023, *in prep.*
- Perley, D. A., Morgan, A. N., Updike, A., et al. 2011, AJ, 141, 36, doi: [10.1088/0004-6256/141/2/36](https://doi.org/10.1088/0004-6256/141/2/36)

- Perley, D. A., Cenko, S. B., Corsi, A., et al. 2014, *ApJ*, 781, 37, doi: [10.1088/0004-637X/781/1/37](https://doi.org/10.1088/0004-637X/781/1/37)
- Piano, G., Verrecchia, F., Bulgarelli, A., et al. 2022, GRB Coordinates Network, 32657
- Pillera, R., Bissaldi, E., Omodei, N., et al. 2022, GRB Coordinates Network, 32658
- Pineau, F.-X., Boch, T., Derrière, S., & Schaaff, A. 2020, in *Astronomical Society of the Pacific Conference Series*, Vol. 522, *Astronomical Data Analysis Software and Systems XXVII*, ed. P. Ballester, J. Ibsen, M. Solar, & K. Shortridge, 125
- Planck Collaboration, Ade, P. A. R., Aghanim, N., et al. 2016, *A&A*, 594, A13, doi: [10.1051/0004-6361/201525830](https://doi.org/10.1051/0004-6361/201525830)
- Popowski, P., Cook, K. H., & Becker, A. C. 2003, *AJ*, 126, 2910, doi: [10.1086/37929110.48550/arXiv.astro-ph/0303075](https://doi.org/10.1086/37929110.48550/arXiv.astro-ph/0303075)
- Racusin, J. L., Karpov, S. V., Sokolowski, M., et al. 2008, *Nature*, 455, 183, doi: [10.1038/nature07270](https://doi.org/10.1038/nature07270)
- Rajabov, Y., Sadibekova, T., Tillayev, Y., et al. 2022, GRB Coordinates Network, 32795
- Rastinejad, J., & Fong, W. 2022, GRB Coordinates Network, 32749
- Rastinejad, J. C., Gompertz, B. P., Levan, A. J., et al. 2022, *Nature*, 612, 223, doi: [10.1038/s41586-022-05390-w](https://doi.org/10.1038/s41586-022-05390-w)
- Ripa, J., Pal, A., Werner, N., et al. 2022, GRB Coordinates Network, 32685
- Ripa, J., Takahashi, H., Fukazawa, Y., et al. 2023, arXiv e-prints, arXiv:2302.10047, <https://arxiv.org/abs/2302.10047>
- Romanov, F. 2022a, arXiv e-prints, arXiv:2212.12543, doi: [10.48550/arXiv.2212.12543](https://doi.org/10.48550/arXiv.2212.12543)
- Romanov, F. D. 2022b, GRB Coordinates Network, 32664
- . 2022c, GRB Coordinates Network, 32679
- Roming, P. W. A., Kennedy, T. E., Mason, K. O., et al. 2005, *SSRv*, 120, 95, doi: [10.1007/s11214-005-5095-4](https://doi.org/10.1007/s11214-005-5095-4)
- Rossi, A., Rothberg, B., Palazzi, E., et al. 2022, *ApJ*, 932, doi: [10.3847/1538-4357/ac60a2](https://doi.org/10.3847/1538-4357/ac60a2)
- Rowles, J., & Froebrich, D. 2009, *MNRAS*, 395, 1640, doi: [10.1111/j.1365-2966.2009.14655.x](https://doi.org/10.1111/j.1365-2966.2009.14655.x)
- Ryan, G., van Eerten, H., Piro, L., & Troja, E. 2020, *Astrophys. J.*, 896, 166, doi: [10.3847/1538-4357/ab93cf](https://doi.org/10.3847/1538-4357/ab93cf)
- Sánchez-Ramírez, R., Hancock, P. J., Jóhannesson, G., et al. 2017, *MNRAS*, 464, 4624, doi: [10.1093/mnras/stw2608](https://doi.org/10.1093/mnras/stw2608)
- Sari, R., & Piran, T. 1999, *ApJ*, 520, 641, doi: [10.1086/307508](https://doi.org/10.1086/307508)
- Sari, R., Piran, T., & Narayan, R. 1998, *Astrophys. J. Lett.*, 497, L17, doi: [10.1086/311269](https://doi.org/10.1086/311269)
- Sasada, M., Imai, Y., Murata, K. L., et al. 2022, GRB Coordinates Network, 32730
- Sato, Y., Obayashi, K., Theodre Zhang, B., et al. 2023, *Journal of High Energy Astrophysics*, 37, 51, doi: [10.1016/j.jheap.2022.12.004](https://doi.org/10.1016/j.jheap.2022.12.004)
- Schlaflly, E. F., & Finkbeiner, D. P. 2011, *ApJ*, 737, 103, doi: [10.1088/0004-637X/737/2/103](https://doi.org/10.1088/0004-637X/737/2/103)
- Schlegel, D. J., Finkbeiner, D. P., & Davis, M. 1998, *ApJ*, 500, 525, doi: [10.1086/305772](https://doi.org/10.1086/305772)
- Schneider, B., Adami, C., Le Floc'h, E., et al. 2022, GRB Coordinates Network, 32753
- Schnoor, P. W., Nicholson, P., & Welch, D. L. 2022, GRB Coordinates Network, 32744
- Selsing, J., Malesani, D., Goldoni, P., et al. 2019, *A&A*, 623, A92, doi: [10.1051/0004-6361/201832835](https://doi.org/10.1051/0004-6361/201832835)
- Shrestha, M., Sand, D., Alexander, K. D., et al. 2022, GRB Coordinates Network, 32759
- Shrestha, M., Bostroem, K., Sand, D., et al. 2022, GRB Coordinates Network, 32771
- Shrestha, M., Sand, D. J., Alexander, K. D., et al. 2023, arXiv e-prints, arXiv:2302.03829, <https://arxiv.org/abs/2302.03829>
- Stanek, K. Z., Matheson, T., Garnavich, P. M., et al. 2003, *ApJL*, 591, L17, doi: [10.1086/376976](https://doi.org/10.1086/376976)
- Strausbaugh, R. 2022a, GRB Coordinates Network, 32693
- . 2022b, GRB Coordinates Network, 32738
- Tan, W. J., Li, C. K., Ge, M. Y., et al. 2022, *The Astronomer's Telegram*, 15660
- Thöne, C. C., Greiner, J., Savaglio, S., & Jehin, E. 2007, *ApJ*, 671, 628, doi: [10.1086/522558](https://doi.org/10.1086/522558)
- Thöne, C. C., de Ugarte Postigo, A., Fryer, C. L., et al. 2011, *Nature*, 480, 72, doi: [10.1038/nature10611](https://doi.org/10.1038/nature10611)
- Tiengo, A., Pintore, F., Mereghetti, S., Salvaterra, R., & a larger Collaboration. 2022, GRB Coordinates Network, 32680
- Tiengo, A., Pintore, F., Vaia, B., et al. 2023, arXiv e-prints, arXiv:2302.11518, doi: [10.48550/arXiv.2302.11518](https://doi.org/10.48550/arXiv.2302.11518)
- Tohuvavohu, A., Beardmore, A. P., Osborne, J. P., et al. 2022, GRB Coordinates Network, 32671
- Tonry, J. L., Stubbs, C. W., Lykke, K. R., et al. 2012, *ApJ*, 750, 99, doi: [10.1088/0004-637X/750/2/99](https://doi.org/10.1088/0004-637X/750/2/99)
- Towner, M. C., Cupak, M., Deshayes, J., et al. 2020, *PASA*, 37, e008, doi: [10.1017/pasa.2019.48](https://doi.org/10.1017/pasa.2019.48)
- Troja, E., Fryer, C. L., O'Connor, B., et al. 2022, *Nature*, 612, 228, doi: [10.1038/s41586-022-05327-3](https://doi.org/10.1038/s41586-022-05327-3)
- Ursi, A., Panebianco, G., Pittori, C., et al. 2022, GRB Coordinates Network, 32650
- van der Horst, A. J., Paragi, Z., de Bruyn, A. G., et al. 2014, *MNRAS*, 444, 3151, doi: [10.1093/mnras/stu1664](https://doi.org/10.1093/mnras/stu1664)
- van Eerten, H., Leventis, K., Meliani, Z., Wijers, R., & Keppens, R. 2010, *Mon. Not. Roy. Astron. Soc.*, 403, 300, doi: [10.1111/j.1365-2966.2009.16109.x](https://doi.org/10.1111/j.1365-2966.2009.16109.x)

- Vanderspek, R., Sakamoto, T., Barraud, C., et al. 2004, *ApJ*, 617, 1251, doi: [10.1086/423923](https://doi.org/10.1086/423923)
- Vasilopoulos, G., Karavola, D., Stathopoulos, S. I., & Petropoulou, M. 2023, *MNRAS*, doi: [10.1093/mnras/stad375](https://doi.org/10.1093/mnras/stad375)
- Veres, P., Burns, E., Bissaldi, E., et al. 2022, GRB Coordinates Network, 32636
- Vestrand, W. T., Wren, J. A., Panaitescu, A., et al. 2014, *Science*, 343, 38, doi: [10.1126/science.1242316](https://doi.org/10.1126/science.1242316)
- Vidal, E., Zheng, W., Filippenko, A. V., & KAIT GRB team. 2022, GRB Coordinates Network, 32669
- Vinko, J., Bodi, A., Pal, A., et al. 2022, GRB Coordinates Network, 32709
- Wang, X.-G., Zhang, B., Liang, E.-W., et al. 2018, *ApJ*, 859, 160, doi: [10.3847/1538-4357/aabc13](https://doi.org/10.3847/1538-4357/aabc13)
- Williams, M. A., Kennea, J. A., Dichiara, S., et al. 2023, arXiv e-prints, arXiv:2302.03642, <https://arxiv.org/abs/2302.03642>
- Woosley, S. E. 1993, *ApJ*, 405, 273, doi: [10.1086/172359](https://doi.org/10.1086/172359)
- Xia, Z.-Q., Wang, Y., Yuan, Q., & Fan, Y.-Z. 2022a, GRB Coordinates Network, 32748
- . 2022b, arXiv e-prints, arXiv:2210.13052, doi: [10.48550/arXiv.2210.13052](https://doi.org/10.48550/arXiv.2210.13052)
- Xu, D., Jiang, S. Q., Fu, S. Y., et al. 2022, GRB Coordinates Network, 32647
- Yang, J., Ai, S., Zhang, B.-B., et al. 2022, *Nature*, 612, 232, doi: [10.1038/s41586-022-05403-8](https://doi.org/10.1038/s41586-022-05403-8)
- Zhang, B. B., Liu, Z. K., Peng, Z. K., et al. 2021, *Nature Astronomy*, 5, 911, doi: [10.1038/s41550-021-01395-z](https://doi.org/10.1038/s41550-021-01395-z)
- Zhang, S.-N., Li, T., Lu, F., et al. 2020, *Science China Physics, Mechanics, and Astronomy*, 63, 249502, doi: [10.1007/s11433-019-1432-6](https://doi.org/10.1007/s11433-019-1432-6)

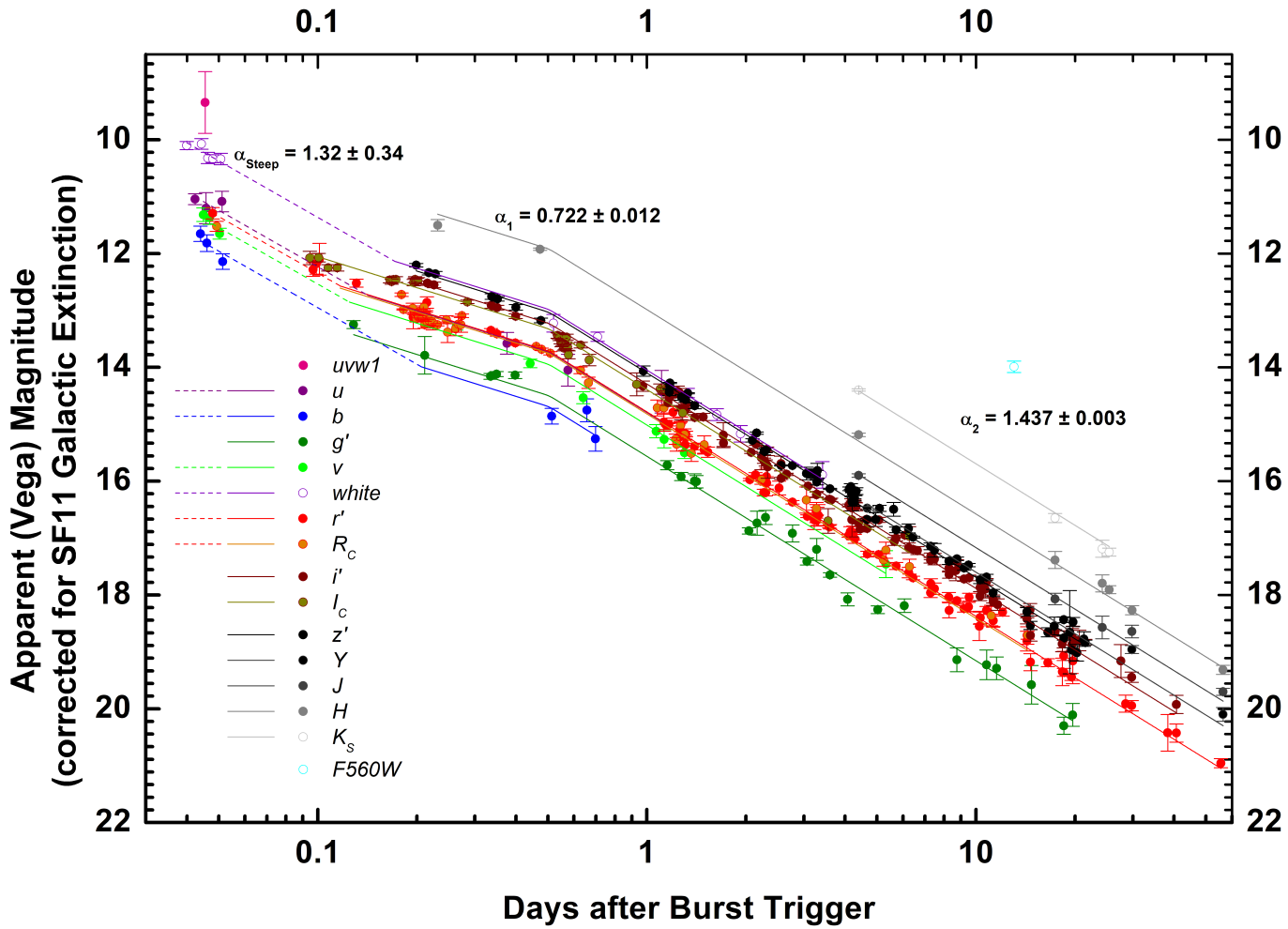


Figure 11. UVOIR light curve of GRB 221009A (see section "Empirical light curve analysis"). The magnitudes, expressed in the Vega system, are corrected for the SF11 galactic extinction. The break slope is at ~ 0.6 d post GRB trigger time between α_1 and α_2 .

APPENDIX

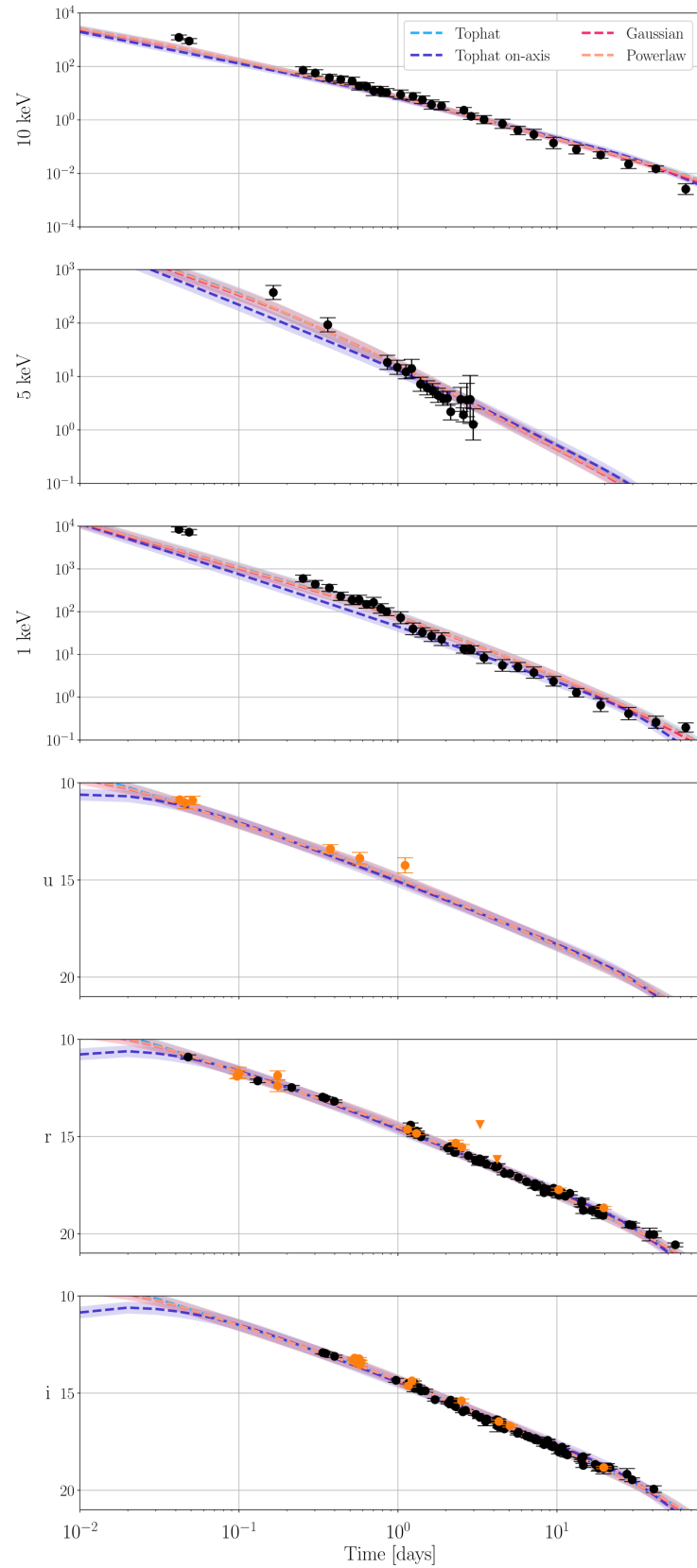


Figure 12. NMMA - Observational data (*Extended* data) and best-fit light curves of selected filters for the NMMA analysis using the SF11 extinction and the four employed jet structures. The X-ray bands are shown in μJy and the rest of the bands are shown in AB magnitude. In the optical band, the *GRANDMA* data points are shown in orange.

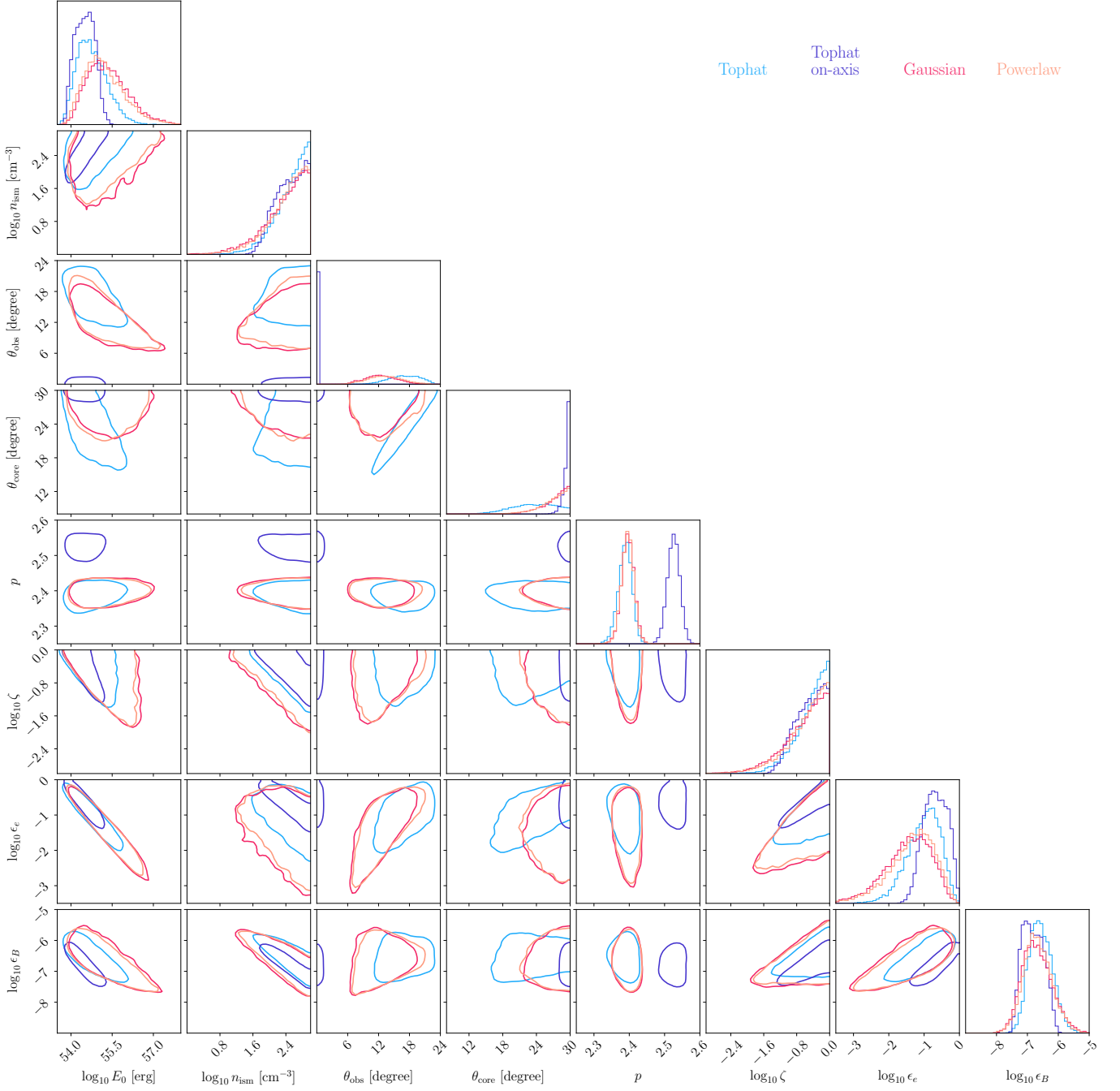


Figure 13. NMMA - Posterior distribution (shown are 90% confidence intervals) for our selected data sets when using different jet models of `afterglowpy` analyzing the *Extended* data.

Table 5. Data used for the numerical data analysis sections (§3.4.1, §3.4.2). *Swift* data have been converted from the Vega system to the AB system. Data are given fully extinction-corrected, for either SF11 MW foreground extinction (described in section 3.2, or RF09^b, and the corresponding SMC extinction in the host galaxy (§3.2).

Delay		Filter	SF11		RF09		Observatory
(day)	(sec)		Magnitude	Upper-limit	Magnitude	Upper-limit	
0.0423	3.657×10^3	<i>u</i>	10.87 ± 0.15	-	10.65 ± 0.35	-	<i>Swift</i> UVOT
0.0457	3.949×10^3	<i>u</i>	11.03 ± 0.30^a	-	10.77 ± 0.44	-	<i>Swift</i> UVOT
0.0511	4.416×10^3	<i>u</i>	10.91 ± 0.22	-	10.75 ± 0.39	-	<i>Swift</i> UVOT
0.3755	3.244×10^4	<i>u</i>	13.40 ± 0.22	-	-	-	<i>Swift</i> UVOT
0.5751	4.969×10^4	<i>u</i>	13.88 ± 0.30	-	-	-	<i>Swift</i> UVOT
1.1084	9.576×10^4	<i>u</i>	14.25 ± 0.39	-	-	-	<i>Swift</i> UVOT
0.2572	2.222×10^4	<i>B</i>	-	11.76	-	11.69	KNC-SCT-0.28
1.1368	9.822×10^4	<i>g'</i>	14.81 ± 0.21	-	14.70 ± 0.31	-	KAO
19.6945	1.702×10^6	<i>g'</i>	18.95 ± 0.22	-	18.84 ± 0.31	-	CFHT-Megacam
-0.0010	-90	<i>V</i>	-	-2.79	-	-2.9	Mundrabilla
-0.0007	-60	<i>V</i>	-	-2.79	-	-2.9	Mundrabilla
-0.0003	-30	<i>V</i>	-	-0.99	-	-1.1	Raw War Road
0.0000	0	<i>V</i>	-	-0.99	-	-1.1	Raw War Road
0.0004	30	<i>V</i>	-	-0.99	-	-1.1	Raw War Road
0.0007	60	<i>V</i>	-	-0.99	-	-1.1	Raw War Road
0.0011	90	<i>V</i>	-	-0.99	-	-1.1	Raw War Road
0.0014	120	<i>V</i>	-	-0.99	-	-1.1	Raw War Road
0.0017	150	<i>V</i>	-	-0.99	-	-1.1	Raw War Road
0.0021	180	<i>V</i>	-	-0.99	-	-1.1	Raw War Road
0.0024	210	<i>V</i>	-	-0.99	-	-1.1	Raw War Road
0.0031	270	<i>V</i>	-	-0.99	-	-1.1	Raw War Road
0.0035	300	<i>V</i>	-	-0.99	-	-1.1	Raw War Road
0.0042	360	<i>V</i>	-	-0.99	-	-1.1	Raw War Road
0.0045	390	<i>V</i>	-	-0.99	-	-1.1	Raw War Road
0.2677	2.313×10^4	<i>V</i>	12.60 ± 0.10	-	12.50 ± 0.22	-	KNC-SCT-0.28
1.1465	9.906×10^4	<i>V</i>	14.57 ± 0.16	-	14.47 ± 0.26	-	ShAO
1.2606	1.089×10^5	<i>V</i>	-	13.90	-	13.80	KNC-SCT-0.28
0.0972	8.40×10^3	<i>r'</i>	11.90 ± 0.13	-	11.79 ± 0.21	-	TRE
0.0993	8.58×10^3	<i>r'</i>	11.80 ± 0.19	-	11.69 ± 0.25	-	TRE
0.0995	8.60×10^3	<i>r'</i>	11.72 ± 0.29	-	11.61 ± 0.33	-	TRE
0.1748	1.510×10^4	<i>r'</i>	12.38 ± 0.31	-	12.27 ± 0.35	-	TRE
0.1750	1.512×10^4	<i>r'</i>	11.86 ± 0.24	-	11.75 ± 0.29	-	TRE
1.1489	9.926×10^4	<i>r'</i>	14.63 ± 0.10	-	14.52 ± 0.19	-	KAO
1.3077	1.130×10^5	<i>r'</i>	14.84 ± 0.07	-	14.73 ± 0.18	-	C2PU/Omicron
2.3083	1.994×10^5	<i>r'</i>	15.34 ± 0.16	-	15.23 ± 0.23	-	KNC-Parent
2.5206	2.178×10^5	<i>r'</i>	15.54 ± 0.13	-	15.43 ± 0.21	-	KNC-LCO/McDO-0.4m
3.2874	2.840×10^5	<i>r'</i>	-	14.38	-	14.27	KNC-C11-ATLAS
4.2097	3.637×10^5	<i>r'</i>	-	16.18	-	16.07	KAO
10.2667	8.870×10^5	<i>r'</i>	17.74 ± 0.09	-	17.63 ± 0.19	-	C2PU/Omicron
19.6965	1.702×10^6	<i>r'</i>	18.67 ± 0.07	-	18.56 ± 0.18	-	CFHT/MegaCam
0.2736	2.364×10^4	<i>R_C</i>	12.41 ± 0.07	-	12.34 ± 0.18	-	KNC-SCT-0.28
1.0813	9.342×10^4	<i>R_C</i>	14.36 ± 0.15	-	14.29 ± 0.22	-	UBAI-ST60
1.2274	1.060×10^5	<i>R_C</i>	14.25 ± 0.10	-	14.18 ± 0.19	-	Lisnyky AZT-8
1.2365	1.068×10^5	<i>R_C</i>	14.39 ± 0.10	-	14.32 ± 0.19	-	Lisnyky AZT-8
1.2755	1.102×10^5	<i>R_C</i>	-	14.30	-	14.23	KNC-SCT-0.28
2.2956	1.983×10^5	<i>R_C</i>	-	14.91	-	14.84	KNC-SCT-0.28

^a This does not include updated measurements provided after Feb. 05. 2022

^b This does not include updated measurements provided after Feb. 05. 2022

Table 5. Continued.

Delay		Filter	SF11		RF09		Observatory
(day)	(sec)		Magnitude	Upper-limit	Magnitude	Upper-limit	
2.3042	1.991×10^5	R_C	15.37 ± 0.10	-	15.30 ± 0.19	-	Lisnyky AZT-8
3.2868	2.840×10^5	R_C	16.13 ± 0.12	-	16.06 ± 0.20	-	Lisnyky AZT-8
5.0674	4.378×10^5	R_C	-	14.61	-	14.54	UBAI-ST60
11.1313	9.617×10^5	R_C	18.01 ± 0.19	-	17.94 ± 0.25	-	UBAI-AZT22
12.4567	1.076×10^6	R_C	-	16.02	-	15.95	VIRT
0.5333	4.608×10^4	i'	13.20 ± 0.06	-	13.13 ± 0.14	-	KNC-BGO
0.5372	4.641×10^4	i'	13.21 ± 0.06	-	13.14 ± 0.14	-	KNC-BGO
0.5411	4.675×10^4	i'	13.24 ± 0.06	-	13.17 ± 0.14	-	KNC-BGO
0.5450	4.709×10^4	i'	13.30 ± 0.06	-	13.23 ± 0.14	-	KNC-BGO
0.5489	4.742×10^4	i'	13.34 ± 0.07	-	13.27 ± 0.15	-	KNC-BGO
0.5527	4.775×10^4	i'	13.33 ± 0.06	-	13.26 ± 0.14	-	KNC-BGO
0.5572	4.814×10^4	i'	13.42 ± 0.06	-	13.35 ± 0.14	-	KNC-BGO
0.5611	4.848×10^4	i'	13.40 ± 0.06	-	13.33 ± 0.14	-	KNC-BGO
0.5650	4.882×10^4	i'	13.37 ± 0.07	-	13.30 ± 0.15	-	KNC-BGO
0.5689	4.915×10^4	i'	13.23 ± 0.06	-	13.16 ± 0.14	-	KNC-BGO
0.5727	4.948×10^4	i'	13.40 ± 0.07	-	13.33 ± 0.15	-	KNC-BGO
0.5766	4.982×10^4	i'	13.54 ± 0.08	-	13.47 ± 0.15	-	KNC-BGO
1.1625	1.004×10^5	i'	14.63 ± 0.06	-	14.56 ± 0.14	-	KAO
1.2255	1.059×10^5	i'	14.37 ± 0.10	-	14.30 ± 0.16	-	KNC-IRIS
2.5092	2.168×10^5	i'	15.40 ± 0.10	-	15.33 ± 0.16	-	KNC-BGO
3.5534	3.070×10^5	i'	16.46 ± 0.22	-	16.39 ± 0.26	-	KNC-BGO
4.2108	3.638×10^5	i'	16.69 ± 0.30	-	16.62 ± 0.33	-	KAO
19.7097	1.703×10^6	i'	18.83 ± 0.06	-	18.76 ± 0.14	-	CFHT/MegaCam
0.2887	2.494×10^4	I_C	12.40 ± 0.06	-	12.21 ± 0.13	-	KNC-SCT-0.28
1.2902	1.115×10^5	I_C	14.31 ± 0.14	-	14.12 ± 0.18	-	KNC-SCT-0.28
2.3509	2.031×10^5	I_C	-	14.79	-	14.60	KNC-SCT-0.28
6.3104	5.452×10^5	I_C	16.96 ± 0.17	-	16.77 ± 0.21	-	Lisnyky AZT-8
15.4848	1.338×10^6	I_C	-	16.98	-	16.79	VIRT
1.1745	1.015×10^5	z'	14.80 ± 0.07	-	14.70 ± 0.11	-	KAO
4.217	3.643×10^5	z'	16.73 ± 0.16	-	16.63 ± 0.19	-	KAO
13.184	1.139×10^6	z'	-	18.23	-	18.13	KAO
19.7308	1.705×10^6	z'	18.84 ± 0.09	-	18.74 ± 0.12	-	CFHT/MegaCam
Delay		X-ray Filter	Flux		Flux error		Observatory
(day)	(sec)	Central frequency	(Jansky)		(Jansky)		
0.1644	1.420×10^4	5 keV	3.74×10^{-4}		7.49×10^{-5}		HXMT/LE
0.3617	3.125×10^4	5 keV	9.32×10^{-5}		2.06×10^{-5}		HXMT/LE
0.8580	7.413×10^4	5 keV	1.83×10^{-5}		3.66×10^{-6}		HXMT/LE
0.9896	8.550×10^4	5 keV	1.49×10^{-5}		2.99×10^{-6}		HXMT/LE
1.1223	9.697×10^4	5 keV	1.23×10^{-5}		2.45×10^{-6}		HXMT/LE
1.2192	1.053×10^5	5 keV	1.41×10^{-5}		5.53×10^{-6}		HXMT/LE
1.3864	1.198×10^5	5 keV	7.18×10^{-6}		1.44×10^{-6}		HXMT/LE
1.5256	1.318×10^5	5 keV	6.17×10^{-6}		1.23×10^{-6}		HXMT/LE
1.6526	1.428×10^5	5 keV	5.45×10^{-6}		1.09×10^{-6}		HXMT/LE
1.7844	1.542×10^5	5 keV	4.44×10^{-6}		8.87×10^{-7}		HXMT/LE
1.9157	1.655×10^5	5 keV	3.91×10^{-6}		7.82×10^{-7}		HXMT/LE
2.0485	1.770×10^5	5 keV	3.91×10^{-6}		8.87×10^{-7}		HXMT/LE
2.1473	1.855×10^5	5 keV	2.19×10^{-6}		7.59×10^{-7}		HXMT/LE
2.4809	2.143×10^5	5 keV	3.73×10^{-6}		1.93×10^{-6}		HXMT/LE
2.5822	2.231×10^5	5 keV	1.92×10^{-6}		3.84×10^{-7}		HXMT/LE
2.7138	2.345×10^5	5 keV	3.64×10^{-6}		2.62×10^{-6}		HXMT/LE
2.8464	2.459×10^5	5 keV	3.73×10^{-6}		3.83×10^{-6}		HXMT/LE
2.9744	2.570×10^5	5 keV	1.27×10^{-6}		8.57×10^{-7}		HXMT/LE

Table 5. Continued.

Delay		X-ray Filter	Flux	Flux error	Observatory
(day)	(sec)	Central frequency	(Jansky)	(Jansky)	
0.0419	0.362×10^4	10 keV	1.23×10^{-3}	2.51×10^{-4}	<i>Swift</i> XRT
0.0486	0.420×10^4	10 keV	8.95×10^{-4}	1.88×10^{-4}	<i>Swift</i> XRT
0.2529	2.185×10^4	10 keV	7.23×10^{-5}	2.14×10^{-5}	<i>Swift</i> XRT
0.3018	2.608×10^4	10 keV	5.71×10^{-5}	1.64×10^{-5}	<i>Swift</i> XRT
0.3701	3.197×10^4	10 keV	3.76×10^{-5}	1.10×10^{-5}	<i>Swift</i> XRT
0.4365	3.771×10^4	10 keV	3.29×10^{-5}	9.87×10^{-6}	<i>Swift</i> XRT
0.5145	4.445×10^4	10 keV	2.87×10^{-5}	9.62×10^{-6}	<i>Swift</i> XRT
0.5698	4.923×10^4	10 keV	1.85×10^{-5}	6.31×10^{-6}	<i>Swift</i> XRT
0.6348	5.484×10^4	10 keV	1.80×10^{-5}	5.48×10^{-6}	<i>Swift</i> XRT
0.7026	6.070×10^4	10 keV	1.22×10^{-5}	4.97×10^{-6}	<i>Swift</i> XRT
0.7808	6.746×10^4	10 keV	1.22×10^{-5}	4.72×10^{-6}	<i>Swift</i> XRT
0.8481	7.327×10^4	10 keV	1.06×10^{-5}	3.63×10^{-6}	<i>Swift</i> XRT
1.0395	8.982×10^4	10 keV	8.91×10^{-6}	3.54×10^{-6}	<i>Swift</i> XRT
1.2431	1.074×10^5	10 keV	7.61×10^{-6}	2.45×10^{-6}	<i>Swift</i> XRT
1.4247	1.231×10^5	10 keV	5.73×10^{-6}	1.91×10^{-6}	<i>Swift</i> XRT
1.6254	1.404×10^5	10 keV	3.77×10^{-6}	1.48×10^{-6}	<i>Swift</i> XRT
1.8796	1.624×10^5	10 keV	3.36×10^{-6}	1.17×10^{-6}	<i>Swift</i> XRT
2.5980	2.245×10^5	10 keV	2.32×10^{-6}	5.38×10^{-7}	<i>Swift</i> XRT
2.8842	2.492×10^5	10 keV	1.37×10^{-6}	3.63×10^{-7}	<i>Swift</i> XRT
3.4783	3.005×10^5	10 keV	1.02×10^{-6}	3.60×10^{-7}	<i>Swift</i> XRT
4.5403	3.923×10^5	10 keV	7.20×10^{-7}	2.87×10^{-7}	<i>Swift</i> XRT
5.6807	4.908×10^5	10 keV	4.04×10^{-7}	1.46×10^{-7}	<i>Swift</i> XRT
7.1565	6.183×10^5	10 keV	2.85×10^{-7}	1.28×10^{-7}	<i>Swift</i> XRT
9.5104	8.217×10^5	10 keV	1.37×10^{-7}	6.70×10^{-8}	<i>Swift</i> XRT
13.260	1.146×10^6	10 keV	7.76×10^{-8}	2.97×10^{-8}	<i>Swift</i> XRT
18.832	1.627×10^6	10 keV	4.86×10^{-8}	1.31×10^{-8}	<i>Swift</i> XRT
28.236	2.440×10^6	10 keV	2.21×10^{-8}	8.34×10^{-9}	<i>Swift</i> XRT
41.971	3.626×10^6	10 keV	1.48×10^{-8}	3.81×10^{-9}	<i>Swift</i> XRT
64.598	5.581×10^6	10 keV	2.59×10^{-9}	1.23×10^{-9}	<i>Swift</i> XRT
0.0419	0.362×10^4	1 keV	8.36×10^{-3}	1.16×10^{-3}	<i>Swift</i> XRT
0.0486	0.420×10^4	1 keV	7.25×10^{-3}	1.04×10^{-3}	<i>Swift</i> XRT
0.2529	2.185×10^4	1 keV	5.98×10^{-4}	1.12×10^{-4}	<i>Swift</i> XRT
0.3018	2.608×10^4	1 keV	4.39×10^{-4}	8.75×10^{-5}	<i>Swift</i> XRT
0.3701	3.197×10^4	1 keV	3.59×10^{-4}	6.76×10^{-5}	<i>Swift</i> XRT
0.4365	3.771×10^4	1 keV	2.30×10^{-4}	5.15×10^{-5}	<i>Swift</i> XRT
0.5145	4.445×10^4	1 keV	1.89×10^{-4}	4.82×10^{-5}	<i>Swift</i> XRT
0.5698	4.923×10^4	1 keV	1.91×10^{-4}	4.60×10^{-5}	<i>Swift</i> XRT
0.6348	5.484×10^4	1 keV	1.49×10^{-4}	3.07×10^{-5}	<i>Swift</i> XRT
0.7026	6.070×10^4	1 keV	1.65×10^{-4}	4.62×10^{-5}	<i>Swift</i> XRT
0.7808	6.746×10^4	1 keV	1.19×10^{-4}	3.07×10^{-5}	<i>Swift</i> XRT
0.8481	7.327×10^4	1 keV	9.98×10^{-5}	2.10×10^{-5}	<i>Swift</i> XRT
1.0395	8.982×10^4	1 keV	7.24×10^{-5}	2.33×10^{-5}	<i>Swift</i> XRT
1.2431	1.074×10^5	1 keV	3.96×10^{-5}	1.23×10^{-5}	<i>Swift</i> XRT
1.4247	1.231×10^5	1 keV	3.28×10^{-5}	8.30×10^{-6}	<i>Swift</i> XRT
1.6254	1.404×10^5	1 keV	2.71×10^{-5}	7.93×10^{-6}	<i>Swift</i> XRT
1.8796	1.624×10^5	1 keV	2.28×10^{-5}	7.84×10^{-6}	<i>Swift</i> XRT
2.5980	2.245×10^5	1 keV	1.35×10^{-5}	2.94×10^{-6}	<i>Swift</i> XRT
2.8842	2.492×10^5	1 keV	1.28×10^{-5}	2.86×10^{-6}	<i>Swift</i> XRT
3.4783	3.005×10^5	1 keV	8.41×10^{-6}	2.59×10^{-6}	<i>Swift</i> XRT
4.5403	3.923×10^5	1 keV	5.56×10^{-6}	1.75×10^{-6}	<i>Swift</i> XRT
5.6807	4.908×10^5	1 keV	5.08×10^{-6}	1.24×10^{-6}	<i>Swift</i> XRT
7.1565	6.183×10^5	1 keV	3.77×10^{-6}	1.16×10^{-6}	<i>Swift</i> XRT
9.5104	8.217×10^5	1 keV	2.34×10^{-6}	5.99×10^{-7}	<i>Swift</i> XRT
13.260	1.146×10^6	1 keV	1.27×10^{-6}	2.92×10^{-7}	<i>Swift</i> XRT
18.832	1.627×10^6	1 keV	6.52×10^{-7}	2.28×10^{-7}	<i>Swift</i> XRT
28.236	2.440×10^6	1 keV	4.15×10^{-7}	1.38×10^{-7}	<i>Swift</i> XRT
41.971	3.626×10^6	1 keV	2.59×10^{-7}	8.25×10^{-8}	<i>Swift</i> XRT
64.598	5.581×10^6	1 keV	1.96×10^{-7}	4.82×10^{-8}	<i>Swift</i> XRT

Table 6. The GRANDMA and GCN optical observations of GRB 221009A. In column (2), the T_{mid} time is the delay between the beginning of the observation and the *Fermi* GBM GRB trigger time (2022-10-09T13:16:59.99) in days. In column (5), magnitudes are given in the AB system and not corrected for Galactic and host-galaxy dust extinction. In column (9), the VETO tag refers to GRANDMA data that were not analyzed due to the bad quality of the images.

T_{start} UT (1)	T_{mid} (days) MJD $T-T_{\text{GRB}}$ (2)	Filter (3)	Exposure (4)	Magnitude (5)	U.L. (6)	Telescope (7)	Reference (8)	Analysis method (9)
2022-10-09T18:06:27	59861.7545 0.2010	u'	6×60s	-	17.9 (3 σ)	MeerLICHT	de Wet et al. (2022)	-
2022-10-10T05:00	59862.2083 0.6549	u'	6×60s	-	-	Nickel-1m	Vidal et al. (2022)	-
2022-10-09T19:19:51	59861.8107 0.2572	B	5×180s	-	18.1 (5 σ)	KNC-SCT-0.28	Broens (2022) & this work	STDPIPE
2022-10-10T04:21	59862.1812 0.6278	B	5×60s	-	19.7	LOAO-1m	Paek et al. (2022)	-
2022-10-09T16:21	59861.6812 0.1278	g'	200s	17.66 ± 0.07	-	GIT	Kumar et al. (2022)	-
2022-10-09T18:21	59861.7646 0.2111	g'	6×60s	18.22 ± 0.33	-	MeerLICHT	de Wet et al. (2022)	-
2022-10-10T05:00	59862.2083 0.6549	g'	300s	18.96 ± 0.1	-	Nickel-1m	Vidal et al. (2022)	-
2022-10-10T11:39	59862.4854 0.932	g'	8340s	-	18.3	MITSuME	Sasada et al. (2022)	-
2022-10-10T12:25	59862.5174 0.9639	g'	2×150s	-	18.3 (3 σ)	SLT-40	Chen et al. (2022)	-
2022-10-10T16:34	59862.6903 1.1368	g'	2×120s	20.38 ± 0.19	19.9 (3 σ)	KAO	this work	MUPHOTEN
2022-10-10T16:56	59862.7056 1.1521	g'	600s	20.13 ± 0.08	-	RTT-150	Bikmaev et al. (2022a)	-
2022-10-10T17:16	59862.7194 1.166	g'	15×30s	20.53 ± 0.1	21.0 (3 σ)	AZT-20	Belkin et al. (2022a)	-
2022-10-10T19:40	59862.8194 1.266	g'	3×100s	20.87 ± 0.36	-	LCOGT	Strausbaugh (2022a)	-
2022-10-10T20:17	59862.8451 1.2917	g'	600s	20.44 ± 0.25	-	RTT-150	Bikmaev et al. (2022a)	-
2022-10-11T17:10	59863.7153 2.1618	g'	600s	21.15 ± 0.21	-	RTT-150	Bikmaev et al. (2022a)	-
2022-10-12T02:40	59864.1111 2.5577	g'	-	-	23.0	LBTO	Shrestha et al. (2022)	-
2022-10-12T03:34	59864.1486 2.5952	g'	3×300s	-	22.3	LCOGT	Strausbaugh (2022b)	-
2022-10-15T15:44	59867.6556 6.1021	g'	30×60s	22.6 ± 0.12	23.4(3 σ)	AZT-20	Belkin et al. (2022a)	-
2022-10-29T05:57	59881.2479 19.6945	g'	3×300s	24.52 ± 0.2	26.1	CFHT-Megacam	this work	MUPHOTEN
2022-10-09T13:15:29	59861.5524 -0.0010	V	27s	-	2.0	Mundrabilla	this work	section 2.2
2022-10-09T13:15:59	59861.5528 -0.0007	V	27s	-	2.0	Mundrabilla	this work	section 2.2
2022-10-09T13:16:30	59861.5531 -0.0003	V	27s	-	3.8	RawWarRoad	this work	section 2.2
2022-10-09T13:17:00	59861.5535 0.0000	V	27s	-	3.8	RawWarRoad	this work	section 2.2
2022-10-09T13:17:30	59861.5538 0.0004	V	27s	-	3.8	RawWarRoad	this work	section 2.2
2022-10-09T13:18:00	59861.5542 0.0007	V	27s	-	3.8	RawWarRoad	this work	section 2.2
2022-10-09T13:18:30	59861.5545 0.0011	V	27s	-	3.8	RawWarRoad	this work	section 2.2
2022-10-09T13:19:00	59861.5549 0.0014	V	27s	-	3.8	RawWarRoad	this work	section 2.2
2022-10-09T13:19:30	59861.5552 0.0017	V	27s	-	3.8	RawWarRoad	this work	section 2.2
2022-10-09T13:20:00	59861.5556 0.0021	V	27s	-	3.8	RawWarRoad	this work	section 2.2
2022-10-09T13:20:30	59861.5559 0.0024	V	27s	-	3.8	RawWarRoad	this work	section 2.2
2022-10-09T13:21:30	59861.5566 0.0031	V	27s	-	3.8	RawWarRoad	this work	section 2.2
2022-10-09T13:22:00	59861.5569 0.0035	V	27s	-	3.8	RawWarRoad	this work	section 2.2
2022-10-09T13:23:00	59861.5576 0.0042	V	27s	-	3.8	RawWarRoad	this work	section 2.2
2022-10-09T13:23:30	59861.5580 0.0045	V	27s	-	3.8	RawWarRoad	this work	section 2.2
2022-10-09T19:35:00	59861.82118 0.2677	V	5×180s	17.39 ± 0.08	18.3 (5 σ)	KNC-SCT-0.28	Broens (2022) & this work	MUPHOTEN
2022-10-10T04:23	59862.1826 0.6292	V	5×60s	18.74 ± 0.13	19.5	LOAO-1m	Paek et al. (2022)	-
2022-10-10T16:48	59862.7 1.1465	V	25×120s	19.36 ± 0.15	19.5	ShAOT60	this work	STDPIPE
2022-10-10T19:16	59862.8141 1.2606	V	11×180s	-	18.7 (5 σ)	KNC-SCT-0.28	this work	MUPHOTEN
2022-10-14T20:13	59866.8768 5.3233	V	180×32s	21.55 ± 0.24	21.2 (5 σ)	KNC-T-CAT	this work	STDPIPE
2022-10-09T19:51	59861.8271 0.2736	R_c	5×180s	16.26 ± 0.05	17.9 (5 σ)	KNC-SCT-0.28	Broens (2022) & this work	MUPHOTEN
2022-10-10T11:39	59862.4854 0.932	R_c	60s	-	17.0	MITSuME	Sasada et al. (2022)	-
2022-10-10T14:56	59862.6347 1.0813	R_c	6×180s	18.21 ± 0.14	18.5	UBAI-ST60	this work	MUPHOTEN
2022-10-10T15:53	59862.6774 1.124	R_c	15×90s	-	-	ShAOT60	this work	VETO
2022-10-10T18:32	59862.7809 1.2274	R_c	25×30s	18.1 ± 0.08	19.3	Lisnyky-AZT-8	this work	MUPHOTEN
2022-10-10T18:45	59862.7899 1.2365	R_c	25×30s	18.24 ± 0.08	19.1	Lisnyky-AZT-8	this work	MUPHOTEN
2022-10-10T19:43:14	59862.8290 1.2755	R_c	7×180s	-	18.2 (5 σ)	KNC-SCT-0.28	this work	MUPHOTEN
2022-10-11T19:52:44	59863.8292 2.2956	R_c	20×180s	-	18.8 (5 σ)	KNC-SCT-0.28	Broens (2022) & this work	MUPHOTEN
2022-10-11T18:44	59863.8576 2.3042	R_c	111×60s	19.22 ± 0.08	20.5	Lisnyky-AZT-8	this work	MUPHOTEN
2022-10-12T14:24	59864.6139 3.0604	R_c	5×240s	-	-	UBAI-ST60	this work	VETO
2022-10-12T19:40	59864.8403 3.2868	R_c	30×60s	19.98 ± 0.11	20.1	Lisnyky-AZT-8	this work	MUPHOTEN
2022-10-14T14:10	59866.6208 5.0674	R_c	11×240s	-	18.5	UBAI-ST60	this work	MUPHOTEN
2022-10-21T22:58	59874.0102 12.4567	R_c	460×10s	-	19.9	VIRT	this work	MUPHOTEN
2022-10-22T03:34:20	59874.1697 12.6162	R_c	6×600 s	-	19.4 (5 σ)	KNC-IT11	this work	STDPIPE
2022-10-09T14:25	59861.6007 0.0472	r'	-	14.93 ± 0.1	-	NEXT	Xu et al. (2022)	-
2022-10-09T14:27	59861.6021 0.0486	r'	120s	14.84 ± 0.09	20.8	Mondy	Belkin et al. (2022c)	-
2022-10-09T15:36	59861.6507 0.0972	r'	180s	15.92 ± 0.12	16.5	TRE	this work	STDPIPE & MUPHOTEN
2022-10-09T15:39	59861.6528 0.0993	r'	180s	15.82 ± 0.18	16.7	TRE	this work	STDPIPE & MUPHOTEN
2022-10-09T15:40	59861.6530 0.0995	r'	180s	15.74 ± 0.28	16.1	TRE	this work	STDPIPE & MUPHOTEN
2022-10-09T16:25	59861.684 0.1306	r'	200s	16.16 ± 0.07	-	GIT	Kumar et al. (2022)	-
2022-10-09T17:28	59861.7283 0.1748	r'	180s	16.4 ± 0.3	16.3	TRE	this work	STDPIPE & MUPHOTEN
2022-10-09T17:29	59861.7285 0.1750	r'	180s	15.88 ± 0.23	16.3	TRE	this work	STDPIPE & MUPHOTEN
2022-10-09T18:25	59861.7674 0.2139	r'	-	16.5 ± 0.1	-	NEXT	Xu et al. (2022)	-
2022-10-09T18:23	59861.766 0.2125	r'	6×60s	16.76 ± 0.08	-	MeerLICHT	de Wet (2022)	-
2022-10-09T18:49	59861.784 0.2306	r'	90s	16.57 ± 0.02	-	OSN-0.9	Hu et al. (2022)	-
2022-10-09T23:58	59861.9986 0.4452	r'	-	17.36 ± 0.12	-	REM	Brivio et al. (2022)	-
2022-10-10T04:25	59862.184 0.6306	r'	60×5s	17.55 ± 0.06	19.8	LOAO-1m	Paek et al. (2022)	-
2022-10-10T05:00	59862.2083 0.6549	r'	300s	17.8 ± 0.1	-	Nickel-1m	Vidal et al. (2022)	-

Table 6. Continued.

2022-10-10T12:25	59862.5174	0.9639	r'	2×150s	18.67 ± 0.16	-	SLT-40	Chen et al. (2022)	-
2022-10-10T16:33	59862.7023	1.1489	r'	11×100s	18.65 ± 0.08	20.9	KAO	this work	MUPHOTEN
2022-10-10T17:06	59862.7125	1.159	r'	600s	18.65 ± 0.02	-	RIT-150	Bikmaev et al. (2022a)	-
2022-10-10T17:14	59862.7181	1.1646	r'	18×30s	18.64 ± 0.03	20.8 (3 σ)	AZT-20	Kim et al. (2022)	-
2022-10-10T19:26	59862.8097	1.2563	r'	2×300s	18.74 ± 0.12	-	RC-80	Vinko et al. (2022)	-
2022-10-10T19:40	59862.8194	1.266	r'	3×100s	18.8 ± 0.21	-	LCOGT	Strausbaugh (2022a)	-
2022-10-10T20:30	59862.8611	1.3077	r'	2×300s	18.86 ± 0.04	20.5	C2PU/Omicron	this work	STDPIPE & MUPHOTEN
2022-10-10T20:50	59862.8681	1.3146	r'	600s	18.81 ± 0.05	-	RIT-150	Bikmaev et al. (2022a)	-
2022-10-11T00:15	59863.0444	1.4909	r'	16×360s	18.89 ± 0.06	20.4 (5 σ)	KNC-C14/Ste-Sophie	this work	STDPIPE
2022-10-11T00:58	59863.0846	1.5312	r'	59×120s	18.93 ± 0.09	19.8 (5 σ)	KNC-C11-FREE	this work	STDPIPE
2022-10-11T16:37	59863.6924	2.1389	r'	600s	19.53 ± 0.04	-	RIT-150	Bikmaev et al. (2022a)	-
2022-10-11T20:41	59863.8617	2.3083	r'	-	19.36 ± 0.15	19.8 (5 σ)	KNC-Parent	this work	STDPIPE
2022-10-11T20:44	59863.8639	2.3104	r'	600s	19.67 ± 0.11	-	RIT-150	Bikmaev et al. (2022a)	-
2022-10-12T01:36	59864.1041	2.5506	r'	31×180s	19.56 ± 0.12	20.2 (5 σ)	KNC-LCO/McDO-0.4m	this work	STDPIPE
2022-10-12T03:34	59864.1486	2.5952	r'	3×300s	-	21.4	LCOGT	Strausbaugh (2022b)	-
2022-10-12T17:05	59864.7118	3.1583	r'	600s	20.03 ± 0.06	-	RIT-150	Bikmaev et al. (2022a)	-
2022-10-12T17:38	59864.7347	3.1813	r'	600s	19.97 ± 0.08	-	RIT-150	Bikmaev et al. (2022a)	-
2022-10-12T18:10	59864.7569	3.2035	r'	600s	20.07 ± 0.19	-	RIT-150	Bikmaev et al. (2022a)	-
2022-10-12T18:42	59864.7792	3.2257	r'	600s	20.32 ± 0.17	-	RIT-150	Bikmaev et al. (2022a)	-
2022-10-12T19:15	59864.8409	3.2874	r'	30×120s	-	18.4	KNC-C11-ATLAS	this work	STDPIPE
2022-10-12T19:46	59864.8236	3.2702	r'	600s	20.17 ± 0.12	-	RIT-150	Bikmaev et al. (2022a)	-
2022-10-12T19:40	59864.8194	3.266	r'	1800s	20.23 ± 0.09	-	OHP	Schneider et al. (2022)	-
2022-10-12T20:18	59864.8458	3.2924	r'	300s	20.58 ± 0.7	-	RC-80	Vinko et al. (2022)	-
2022-10-12T20:25	59864.8507	3.2972	r'	600s	20.26 ± 0.16	-	RIT-150	Bikmaev et al. (2022a)	-
2022-10-12T20:57	59864.8729	3.3195	r'	600s	20.24 ± 0.19	-	RIT-150	Bikmaev et al. (2022a)	-
2022-10-13T03:09	59865.1312	3.5778	r'	-	20.44 ± 0.05	-	LDT	O'Connor et al. (2022a)	-
2022-10-13T17:37	59865.7632	4.2097	r'	21×120s	-	20.2	KAO	this work	MUPHOTEN
2022-10-13T16:53	59865.7035	4.15	r'	600s	20.53 ± 0.09	-	RIT-150	Bikmaev et al. (2022b)	-
2022-10-13T17:25	59865.7257	4.1722	r'	600s	20.63 ± 0.09	-	RIT-150	Bikmaev et al. (2022b)	-
2022-10-13T17:58	59865.7486	4.1952	r'	600s	20.71 ± 0.15	-	RIT-150	Bikmaev et al. (2022b)	-
2022-10-13T18:30	59865.7708	4.2174	r'	600s	20.54 ± 0.1	-	RIT-150	Bikmaev et al. (2022b)	-
2022-10-13T19:02	59865.7931	4.2396	r'	600s	20.55 ± 0.12	-	RIT-150	Bikmaev et al. (2022b)	-
2022-10-13T19:35	59865.816	4.2625	r'	600s	20.74 ± 0.16	-	RIT-150	Bikmaev et al. (2022b)	-
2022-10-13T20:08	59865.8389	4.2854	r'	600s	20.9 ± 0.23	-	RIT-150	Bikmaev et al. (2022b)	-
2022-10-13T20:43	59865.8632	4.3097	r'	600s	20.86 ± 0.27	-	RIT-150	Bikmaev et al. (2022b)	-
2022-10-14T05:27	59866.2271	4.6736	r'	-	20.92 ± 0.05	-	Pan-STARRS	Huber et al. (2022)	-
2022-10-15T14:40	59867.6111	6.0577	r'	30×60s	20.96 ± 0.05	22.9 (3 σ)	AZT-20	Belkin et al. (2022a)	-
2022-10-15T06:34	59867.2736	5.7202	r'	-	21.13 ± 0.06	-	Faulkes	Shrestha et al. (2022)	-
2022-10-16T14:41	59868.6118	7.0583	r'	200×25s	21.3 ± 0.04	-	DFOT	Gupta et al. (2022)	-
2022-10-19T02:05	59871.0868	9.5333	r'	-	21.68 ± 0.07	-	LDT	O'Connor et al. (2022b)	-
2022-10-19T18:26	59871.8201	10.2667	r'	4×300s	21.8 ± 0.07	21.9	C2PU/Omicron	this work	STDPIPE & MUPHOTEN
2022-10-20T16:11	59872.6847	11.1313	r'	3×300s	21.86 ± 0.18	21.8	UBAI-AZT22	this work	MUPHOTEN
2022-10-21T14:33	59873.6062	12.0528	r'	30×60s	21.94 ± 0.07	23.9(3 σ)	AZT-20	Belkin et al. (2022b)	-
2022-10-23T00:59:10	59875.0757	13.5222	r'	31×180s	19.4 ± 0.05	19.4 (5 σ)	KNC-C11-FREE	this work	STDPIPE
2022-10-25T01:59:52	59877.1045	15.5510	r'	6×600s	-	20.5 (5 σ)	KNC-iT11	this work	STDPIPE
2022-10-27T00:45:41	59879.0501	17.4967	r'	26×120s	-	20.0 (5 σ)	KNC-C11-FREE	this work	STDPIPE
2022-10-29T05:50	59881.25	19.6965	r'	2×300s	22.69 ± 0.05	25.5	CFHT-Megacam	this work	STDPIPE & MUPHOTEN
2022-10-09T18:26:56	59861.7687	0.2152	i'	6×60s	15.58 ± 0.03	-	MeerLICHT	de Wet et al. (2022)	-
2022-10-10T02:04:32	59862.0868	0.5333	i'	300s	16.24 ± 0.05	17.9 (5 σ)	KNC-BGO	this work	STDPIPE
2022-10-10T02:10:06	59862.0907	0.5372	i'	300s	16.25 ± 0.05	17.9 (5 σ)	KNC-BGO	this work	STDPIPE
2022-10-10T02:15:41	59862.0945	0.5411	i'	300s	16.28 ± 0.05	17.9 (5 σ)	KNC-BGO	this work	STDPIPE
2022-10-10T02:21:15	59862.0984	0.5450	i'	300s	16.34 ± 0.05	17.9 (5 σ)	KNC-BGO	this work	STDPIPE
2022-10-10T02:26:50	59862.1023	0.5489	i'	300s	16.38 ± 0.06	17.8 (5 σ)	KNC-BGO	this work	STDPIPE
2022-10-10T02:32:25	59862.1062	0.5527	i'	300s	16.37 ± 0.05	17.9 (5 σ)	KNC-BGO	this work	STDPIPE
2022-10-10T02:38:55	59862.1107	0.5572	i'	300s	16.46 ± 0.05	18.0 (5 σ)	KNC-BGO	this work	STDPIPE
2022-10-10T02:44:29	59862.1107	0.5611	i'	300s	16.44 ± 0.05	17.9 (5 σ)	KNC-BGO	this work	STDPIPE
2022-10-10T02:50:04	59862.1184	0.5650	i'	300s	16.41 ± 0.06	17.9 (5 σ)	KNC-BGO	this work	STDPIPE
2022-10-10T02:55:39	59862.1223	0.5689	i'	300s	16.27 ± 0.05	17.8 (5 σ)	KNC-BGO	this work	STDPIPE
2022-10-10T03:01:14	59862.1262	0.5727	i'	300s	16.44 ± 0.06	17.8 (5 σ)	KNC-BGO	this work	STDPIPE
2022-10-10T03:06:48	59862.1301	0.5766	i'	300s	16.58 ± 0.07	17.8 (5 σ)	KNC-BGO	this work	STDPIPE
2022-10-10T04:26	59862.1847	0.6313	i'	60×5s	16.41 ± 0.05	19.56	LOAO-1m	Paek et al. (2022)	-
2022-10-10T12:25	59862.5174	0.9639	i'	2×150s	17.38 ± 0.09	-	SLT-40	Chen et al. (2022)	-
2022-10-10T16:59	59862.716	1.1625	i'	9×80s	17.67 ± 0.05	20.7	KAO	this work	MUPHOTEN
2022-10-10T17:23	59862.7243	1.1708	i'	15×30s	17.58 ± 0.01	20.7 (3 σ)	AZT-20	Belkin et al. (2022a)	-
2022-10-10T17:17	59862.7201	1.1667	i'	600s	17.52 ± 0.01	-	RIT-150	Bikmaev et al. (2022a)	-
2022-10-10T18:20:07	59862.7938	1.2255	i'	14×180s	17.47 ± 0.09	17.6 (5 σ)	KNC-IRIS	this work	STDPIPE
2022-10-10T19:26	59862.8097	1.2563	i'	2×300s	17.5 ± 0.12	-	RC-80	Vinko et al. (2022)	-
2022-10-10T21:01	59862.8757	1.3222	i'	600s	17.69 ± 0.02	-	RIT-150	Bikmaev et al. (2022a)	-
2022-10-11T06:07:28	59863.2569	1.7035	i'	300s	17.85 ± 0.13	18.1 (5 σ)	KNC-iT24	this work	STDPIPE
2022-10-11T06:12:57	59863.2607	1.7072	i'	300s	18.24 ± 0.22	18.2 (5 σ)	KNC-iT24	this work	STDPIPE
2022-10-11T00:54	59863.0375	1.484	i'	-	17.92 ± 0.06	-	BlackGEM	Groot et al. (2022)	-
2022-10-11T16:48	59863.7	2.1465	i'	600s	18.4 ± 0.02	-	RIT-150	Bikmaev et al. (2022a)	-
2022-10-11T18:46:47	59863.8193	2.2659	i'	199×32s	18.64 ± 0.21	18.7 (5 σ)	KNC-EHEA-200F5	this work	STDPIPE
2022-10-11T20:56	59863.8722	2.3188	i'	600s	18.49 ± 0.04	-	RIT-150	Bikmaev et al. (2022a)	-
2022-10-12T00:58:02	59864.0626	2.5092	i'	11 × 300s	18.44 ± 0.09	19.0 (5 σ)	KNC-BGO	this work	STDPIPE
2022-10-12T02:07:18	59864.1083	2.5548	i'	11×300s	18.74 ± 0.13	19.3 (5 σ)	KNC-C11-FREE	this work	STDPIPE
2022-10-12T02:40	59864.1111	2.5577	i'	-	19.0 ± 0.2	-	LBTO	Shrestha et al. (2022)	-
2022-10-12T03:34	59864.1486	2.5952	i'	3×300s	-	20.5	LCOGT	Strausbaugh (2022b)	-
2022-10-12T16:54	59864.7042	3.1507	i'	600s	18.82 ± 0.03	-	RIT-150	Bikmaev et al. (2022a)	-
2022-10-12T17:27	59864.7271	3.1736	i'	600s	19.02 ± 0.07	-	RIT-150	Bikmaev et al. (2022a)	-
2022-10-12T17:59	59864.7493	3.1958	i'	600s	19.09 ± 0.1	-	RIT-150	Bikmaev et al. (2022a)	-
2022-10-12T18:31	59864.7715	3.2181	i'	600s	18.95 ± 0.07	-	RIT-150	Bikmaev et al. (2022a)	-
2022-10-12T19:03	59864.7938	3.2403	i'	600s	18.93 ± 0.04	-	RIT-150	Bikmaev et al. (2022a)	-
2022-10-12T19:36	59864.8167	3.2632	i'	600s	18.93 ± 0.04	-	RIT-150	Bikmaev et al. (2022a)	-
2022-10-12T19:40	59864.8194	3.266	i'	3×600s	18.91 ± 0.11	-	OHP	Schneider et al. (2022)	-
2022-10-12T20:08	59864.8389	3.2854	i'	600s	18.92 ± 0.04	-	RIT-150	Bikmaev et al. (2022a)	-
2022-10-12T20:18	59864.8458	3.2924	i'	300s	18.74 ± 0.18	-	RC-80	Vinko et al. (2022)	-

Table 6. Continued.

2022-10-13T02:36:45	59865.1069	3.5534	i'	12 × 300s	19.50 ± 0.22	19.4 (5 σ)	KNC-BGO	this work	STDPIPE
2022-10-13T02:24:22	59865.1149	3.5614	i'	20 × 120s	-	18.7 (5 σ)	KNC-iT11	this work	STDPIPE
2022-10-13T03:09	59865.1312	3.5778	i'	-	19.37 ± 0.05	-	LDT	O'Connor et al. (2022a)	-
2022-10-13T17:04	59865.7111	4.1577	i'	600s	19.51 ± 0.06	-	RTT-150	Bikmaev et al. (2022b)	-
2022-10-13T17:36	59865.7333	4.1799	i'	600s	19.41 ± 0.05	-	RTT-150	Bikmaev et al. (2022b)	-
2022-10-13T18:09	59865.7562	4.2028	i'	600s	19.52 ± 0.05	-	RTT-150	Bikmaev et al. (2022b)	-
2022-10-13T17:42	59865.7642	4.2108	i'	21 × 110s	19.73 ± 0.3	20.3	KAO	this work	MUPHOTEN
2022-10-13T18:41	59865.7785	4.225	i'	600s	19.44 ± 0.04	-	RTT-150	Bikmaev et al. (2022b)	-
2022-10-13T19:13	59865.8007	4.2472	i'	600s	19.45 ± 0.05	-	RTT-150	Bikmaev et al. (2022b)	-
2022-10-13T19:46	59865.8236	4.2702	i'	600s	19.43 ± 0.05	-	RTT-150	Bikmaev et al. (2022b)	-
2022-10-13T20:18	59865.8458	4.2924	i'	600s	19.48 ± 0.06	-	RTT-150	Bikmaev et al. (2022b)	-
2022-10-13T20:53	59865.8701	4.3167	i'	600s	19.5 ± 0.07	-	RTT-150	Bikmaev et al. (2022b)	-
2022-10-14T00:04	59866.0028	4.4493	i'	-	19.89 ± 0.05	-	VLT	Izzo et al. (2022)	-
2022-10-14T00:40	59866.0278	4.4743	i'	7 × 60s	19.8 ± 0.5	-	GMOS	Rastinejad & Fong (2022)	-
2022-10-15T06:34	59867.2736	5.7202	i'	-	20.01 ± 0.05	-	Faulkes	Shrestha et al. (2022)	-
2022-10-15T14:11	59867.591	6.0375	i'	30 × 60s	20.0 ± 0.04	23.2 (3 σ)	AZT-20	Belkin et al. (2022a)	-
2022-10-19T02:05	59871.0868	9.5333	i'	-	20.72 ± 0.05	-	LDT	O'Connor et al. (2022b)	-
2022-10-21T15:04	59873.6278	12.0743	i'	30 × 60s	20.72 ± 0.11	23.3(3 σ)	AZT-20	Belkin et al. (2022b)	-
2022-10-29T06:09	59881.2632	19.7097	i'	2 × 300s	21.87 ± 0.05	24.5	CFHT-Megacam	this work	STDPIPE & MUPHOTEN
2022-10-09T20:05:19	59861.8422	0.2887	I_c	5 × 180s	15.21 ± 0.04	17.0 (5 σ)	KNC-SCT-0.28	this work	MUPHOTEN
2022-10-10T05:00	59862.2083	0.6549	I_c	300s	16.74 ± 0.1	-	Nickel-1m	Vidal et al. (2022)	-
2022-10-10T11:39	59862.4854	0.932	I_c	8340s	17.1 ± 0.2	-	MITSuME	Sasada et al. (2022)	-
2022-10-10T20:04:25	59862.8436	1.2902	I_c	7 × 180s	17.12 ± 0.13	17.0 (5 σ)	KNC-SCT-0.28	this work	MUPHOTEN
2022-10-11T18:14	59863.7958	2.2424	I_c	52 × 60s	-	-	AbAO-T70	this work	VETO
2022-10-11T21:06:16	59863.9043	2.3509	I_c	24 × 180s	-	17.6 (5 σ)	KNC-SCT-0.28	this work	MUPHOTEN
2022-10-12T18:11	59864.7889	3.2354	I_c	45 × 60s	-	-	Lisnyky-AZT-8	this work	VETO
2022-10-13T01:49:56	59865.1248	3.5713	I_c	23 × 300s	18.95 ± 0.12	19.7 (5 σ)	KNC-C11-FREE	this work	STDPIPE
2022-10-15T18:44	59867.8639	6.3104	I_c	120 × 60s	19.77 ± 0.17	19.0	Lisnyky-AZT-8	this work	MUPHOTEN
2022-10-24T23:01	59877.0383	15.4848	I_c	685 × 10s	-	19.8	VIRT	this work	MUPHOTEN
2022-10-09T18:29	59861.7701	0.2167	z'	6 × 60s	14.89 ± 0.03	-	MeerLICHT	de Wet et al. (2022)	-
2022-10-10T12:25	59862.5174	0.9639	z'	2 × 150s	16.6 ± 0.09	-	SLT-40	Chen et al. (2022)	-
2022-10-10T17:26	59862.7264	1.1729	z'	15 × 30s	16.87 ± 0.05	19.8	AZT-20	Belkin et al. (2022a)	-
2022-10-10T17:28	59862.7278	1.1743	z'	600s	16.81 ± 0.01	-	RTT-150	Bikmaev et al. (2022a)	-
2022-10-10T17:15	59862.728	1.1745	z'	10 × 80s	16.97 ± 0.06	20.3	KAO	this work	MUPHOTEN
2022-10-10T21:13	59862.884	1.3306	z'	600s	16.99 ± 0.01	-	RTT-150	Bikmaev et al. (2022a)	-
2022-10-11T00:50	59863.0347	1.4813	z'	-	16.92 ± 0.05	-	BlackGEM	Groot et al. (2022)	-
2022-10-11T16:59	59863.7076	2.1542	z'	600s	17.69 ± 0.02	-	RTT-150	Bikmaev et al. (2022a)	-
2022-10-11T21:07	59863.8799	2.3264	z'	600s	17.72 ± 0.03	-	RTT-150	Bikmaev et al. (2022a)	-
2022-10-12T02:40	59864.1111	2.5577	z'	-	18.26 ± 0.01	-	LBTO	Shresta et al. (2022)	-
2022-10-12T14:34	59864.6092	3.0557	z'	-	18.40 ± 0.11	-	GMG-Lijiang	(Mao et al. 2022)	-
2022-10-12T17:16	59864.7194	3.166	z'	600s	18.2 ± 0.04	-	RTT-150	Bikmaev et al. (2022a)	-
2022-10-12T17:48	59864.7417	3.1882	z'	600s	18.19 ± 0.05	-	RTT-150	Bikmaev et al. (2022a)	-
2022-10-12T18:21	59864.7646	3.2111	z'	600s	18.4 ± 0.08	-	RTT-150	Bikmaev et al. (2022a)	-
2022-10-12T18:53	59864.7868	3.2333	z'	600s	18.26 ± 0.03	-	RTT-150	Bikmaev et al. (2022a)	-
2022-10-12T19:25	59864.809	3.2556	z'	600s	18.23 ± 0.03	-	RTT-150	Bikmaev et al. (2022a)	-
2022-10-12T19:40	59864.8194	3.266	z'	2100s	18.35 ± 0.13	-	OHP	Schneider et al. (2022)	STDPIPE
2022-10-12T19:57	59864.8312	3.2778	z'	600s	18.23 ± 0.04	-	RTT-150	Bikmaev et al. (2022a)	-
2022-10-12T20:35	59864.8576	3.3042	z'	600s	18.3 ± 0.04	-	RTT-150	Bikmaev et al. (2022b)	-
2022-10-12T21:08	59864.8806	3.3271	z'	600s	18.18 ± 0.04	-	RTT-150	Bikmaev et al. (2022b)	-
2022-10-13T17:15	59865.7188	4.1653	z'	600s	18.63 ± 0.05	-	RTT-150	Bikmaev et al. (2022b)	-
2022-10-13T17:47	59865.741	4.1875	z'	600s	18.76 ± 0.05	-	RTT-150	Bikmaev et al. (2022b)	-
2022-10-13T18:19	59865.7632	4.2097	z'	600s	18.69 ± 0.04	-	RTT-150	Bikmaev et al. (2022b)	-
2022-10-13T17:51	59865.7705	4.217	z'	21 × 110s	18.90 ± 0.16	19.8	KAO	this work	MUPHOTEN
2022-10-13T18:52	59865.7861	4.2327	z'	600s	18.75 ± 0.04	-	RTT-150	Bikmaev et al. (2022b)	-
2022-10-13T19:24	59865.8083	4.2549	z'	600s	18.74 ± 0.05	-	RTT-150	Bikmaev et al. (2022b)	-
2022-10-13T19:57	59865.8312	4.2778	z'	600s	18.83 ± 0.05	-	RTT-150	Bikmaev et al. (2022b)	-
2022-10-13T20:32	59865.8556	4.3021	z'	600s	18.74 ± 0.05	-	RTT-150	Bikmaev et al. (2022b)	-
2022-10-13T21:06	59865.8792	4.3257	z'	600s	18.71 ± 0.06	-	RTT-150	Bikmaev et al. (2022b)	-
2022-10-14T12:12	59866.5106	4.9571	z'	-	19.21 ± 0.12	-	GMG-Lijiang	(Mao et al. 2022)	-
2022-10-15T06:34	59867.2736	5.7202	z'	-	19.39 ± 0.05	-	Faulkes	Shrestha et al. (2022)	-
2022-10-15T16:08	59867.6722	6.1188	z'	15 × 60s	19.31 ± 0.08	21.0 (3 σ)	AZT-20	Belkin et al. (2022a)	-
2022-10-22T16:22	59874.7375	13.184	z'	20 × 240s	-	20.4	KAO	this work	MUPHOTEN
2022-10-29T06:32	59881.2843	19.7308	z'	4 × 260s	21.01 ± 0.08	24.0	CFHT-Megacam	this work	MUPHOTEN
2022-10-09T15:30	59861.6458	0.0924	Clear	180s	15.5 ± 0.1	-	SCT	Odeh (2022)	-
2022-10-09T15:49	59861.659	0.1056	Clear	180s	15.6 ± 0.1	-	SCT	Odeh (2022)	-
2022-10-09T17:14	59861.7181	0.1646	Clear	180s	15.9 ± 0.1	-	SCT	Odeh (2022)	-
2022-10-09T18:44	59861.7806	0.2271	Clear	× 60s	16.21 ± 0.11	-	BOOTES-2	Hu et al. (2022)	-
2022-10-10T19:29	59862.8257	1.2722	Clear	20 × 60s	18.52 ± 0.06	19.5	MOSS	this work	MUPHOTEN
2022-10-10T19:31	59862.8490	1.2955	L	34 × 180s	18.38 ± 0.25	20.2 (3 σ)	KNC-HAO	this work	MUPHOTEN
2022-10-10T21:48:00	59862.9188	1.3652	CR	10 × 180s	18.76 ± 0.14	19.2 (5 σ)	KNC-MSXD	this work	STDPIPE
2022-10-11T16:33	59863.7069	2.1535	Clear	10 × 150s	-	17.5	SNOVA	this work	MUPHOTEN
2022-10-11T18:29:21	59863.7707	2.2172	CR	2 × 30s	-	18.3 (5 σ)	KNC-Montarrenti	this work	STDPIPE
2022-10-11T18:24:14	59863.7825	2.2290	CR	15 × 180s	19.22 ± 0.08	20.3	KNC-MSXD	this work	STDPIPE
2022-10-11T18:27:11	59863.8203	2.2668	L	3 × 2960s	-	19.7 (5 σ)	KNC-COK26	this work	STDPIPE
2022-10-12T13:56	59864.5979	3.0445	Clear	10 × 150s	-	19.1	SNOVA	this work	MUPHOTEN
2022-10-14T18:17:29	59866.7944	5.2409	CR	31 × 180s	20.63 ± 0.11	21.3 (5 σ)	KNC-MSXD	this work	STDPIPE
2022-10-14T20:13:33	59866.8768	5.3233	CR	180 × 32s	20.46 ± 0.14	21.0 (5 σ)	KNC-T-CAT	this work	STDPIPE
2022-10-15T19:17:26	59867.8329	6.2795	CR	28 × 180s	20.75 ± 0.13	21.3 (5 σ)	KNC-MSXD	this work	STDPIPE